STANFORD UNIVERSITY

CENTER FOR SYSTEMS RESEARCH

# FINAL REPORT

## Biocybernetic Factors in Human Perception and Memory

Principal Investigator
David C. Lai

*Information Systems Laboratory*

Reproduced by
NATIONAL TECHNICAL
INFORMATION SERVICE
U.S. Department of Commerce
Springfield, VA. 22151

The views and conclusions contained in this document are those of the authors and should not be interpreted as necessarily representing the official policies, either expressed or implied, of the Advanced Research Projects Agency or the U. S. Government.

SEL 75-021

FINAL REPORT

for the Advanced Research Projects Agency

of the Department of Defense

# BIOCYBERNETIC FACTORS IN HUMAN PERCEPTION AND MEMORY

PRINCIPAL INVESTIGATOR:

Dr. David C. Lai

D D C
RECEIVED
NOV 19 1975
A

Contract No. DAHC15-72-C-0232

ARPA Order No. 2190

September 1975

Technical Report No. 6741-5

Department of Electrical Engineering
Stanford Electronics Laboratories
Stanford University Stanford, California 94305

## FOREWORD

This is the final report of our research on biocybernetic factors in human perception and memory which was begun in 1972 at Stanford University and was supported partially* or fully by the Advanced Research Projects Agency of the Department of Defense under contract DAHC15-72-C-0232, which is now terminating. This report presents a brief summary of the objectives and a description of the accomplishments of the project.

Since its inception, this project has been the result of the collaborative efforts of many individuals. Most of the staff members contributed to the writing of this report.

*Partial support for this project was provided from 1972-1973 by NASA/Ames Research Center under Grant NGR 05-020-575.

## PRESENT PROFESSIONAL PERSONNEL

Dr. D. C. Lai, Visiting Professor of Electrical Engineering, Principal Investigator

Dr. T. Kailath, Professor of Electrical Engineering and Director of Information Systems Laboratory, Co-Principal Investigator

Dr. J. E. Anliker, Consultant

Mr. A. Huang (M.S.E.E.), Scientific Programmer

Mr. L. D. Stricklan (B.S.E.E.C.S.), Scientific Programmer

Mr. J. R. Nickolls (M.S.E.E.), Graduate Student Research Assistant

Mr. A. Shah (M.S.E.E. and M.S. Stat.), Graduate Student Research Assistant

Biocybernetic Factors in Human Perception and Memory


## SUMMARY

The objective of this research project is to develop biocybernetic techniques for use in the analysis and development of skills required for the enhancement of concrete images of the "eidetic" type. The scan patterns of the eye during inspection of scenes are treated as indicators of the brain's strategy for the intake of visual information. We attempt to determine the features that differentiate visual scan patterns associated with superior imagery from scan patterns associated with inferior imagery, and simultaneously, to differentiate the EEG features correlated with superior imagery from those correlated with inferior imagery. For this purpose, we have designed a closely-coupled man-machine system to generate image enhancement and to train the individual to exert greater voluntary control over his own imagery. The models for EEG signals and saccadic eye movement in the man-machine system have been completed. These models are used for monitoring and prediction of EEG signals and eye positions. At this moment, all parts but the feedback path of the man-machine system have been implemented. We shall describe in this report the details of these models and discuss their usefulness.

We have assumed that the strategy of an individual with superior visual memory is to fixate his eyes at the optimal locations of the visual scene at the optimal time instants in relation to EEG. Through the EEG model, we have concluded that the EEG signals play the role of timing mechanisms for visual information acquisition and processing. By using our characterization of scan patterns, we are able to show that

the scan pattern is more consistent for individuals with high scores obtained from the Marks' Visual-Memory Task than those with lower scores. These results tend to confirm our assumption and help guide us in obtaining a firmer grip of these optimal locations and time instants. We have also developed and implemented a technique for presenting any part of a scene at a specified foveal location at a specified instant of time. If the specified locations and time instants are optimal, we expect that the image will be enhanced. Prediction techniques have been developed for both saccadic eye movements and EEG waveforms so that lead times may be provided for the presentation of appropriate visual cues (stimuli). We shall present and discuss many of these in this report.

TABLE OF CONTENTS


| Chapter | | Page |
|---|---|---|
| I | Introduction . . . . . | 1 |
| II | Analysis and Modeling of Eye Movements During Scene Inspection . . . . . | 7 |
| III | Modeling of EEG Signals During Visual Stimulation and EEG Waveform Prediction . . . . . | 30 |
| IV | Characterization of Scan Patterns . . . . . | 73 |
| V | Techniques for the Presentation of Visual Cues . . . . | 82 |
| VI | Conclusions . . . . . | 87 |
| | Appendix A Electronic Interface System . . . . . | 89 |
| | Appendix B (1) List of Persons who have Contributed to this Project . . . . . | 95 |
| | (2) List of Relevant Papers Published During the Project . . . . . | 96 |
| | (3) Lectures and Talks . . . . . | 98 |

## LIST OF FIGURES


| Figure Number | | Page |
|---|---|---|
| 1 | Block diagram of the closely-coupled man-machine system for monitoring and training of visual memory skills | 2 |
| 2 | Raw eye movements for a 20-second scan | 10 |
| 3 | Fixation sequence for the scan in Figure 2 | 11 |
| 4 | Stimulus overlaid by the fixation sequence in Figure 3 | 12 |
| 5 | Typical position and velocity plots of a 15° saccade | 15 |
| 6 | Averaged plots from 25 saccades of 10° amplitude | 16 |
| 7 | A model characterizing dynamic properties of saccadic eye movement | 18 |
| 8 | Model response | 21 |
| 9 | Actual and model simulated saccade position | 22 |
| 10 | Actual and model simulated saccade position | 23 |
| 11 | Actual and model simulated saccade position | 25 |
| 12 | Actual and model simulated saccade position and velocity with two-pulse input | 26 |
| 13 | Actual and model simulated saccade position and velocity with three-pulse input | 27 |
| 14 | Phase and amplitude perturbations | 33 |
| 15 | Simulated EEG perturbations resulting from flash at phases 0 and $\pi/2$ radians | 37 |
| 16 | Simulated EEG perturbations resulting from flash at phases of $\pi$ and $3\pi/2$ radians | 38 |
| 17 | Simulated EEG spectra for flash frequencies from .5 Hz to 12.5 Hz | 39 |
| 18 | Simulated EEG spectra for flash frequencies from 13 Hz to 25 Hz | 40 |

| Figure Number | | Page |
|---|---|---|


| | | |
|---|---|---|
| 19 | Simulated EEG spectra for sine frequencies from .5 Hz to 12.5 Hz . . . . . | 42 |
| 20 | Simulated EEG spectra for sine frequencies from 13 Hz to 25 Hz . . . . . | 43 |
| 21 | EEG spectra from subject L. M. for flash frequencies .5 Hz to 12.5 Hz . . . . . | 46 |
| 22 | EEG spectra from subject L. M. for flash frequencies 13 Hz to 25 Hz . . . . . | 47 |
| 23 | EEG spectra from subject F. M. for flash frequencies .5 Hz to 12.5 Hz . . . . . | 48 |
| 24 | EEG spectra from subject F. M. for flash frequencies 13 Hz to 25 Hz . . . . . | 49 |
| 25 | EEG spectra from subject R. S. for sine frequencies .5 Hz to 12.5 Hz . . . . . | 50 |
| 26 | EEG spectra from subject R. S. for sine frequencies 13 Hz to 25 Hz . . . . . | 51 |
| 27 | Actual and simulated EEG spectra in the absence of stimulation . . . . . | 52 |
| 28 | Actual and simulated EEG spectra during flash stimulation of 10.5 Hz . . . . . | 53 |
| 29 | Actual and simulated EEG spectra during flash stimulation of 21.5 Hz . . . . . | 54 |
| 30 | Actual and simulated EEG spectra during flash stimulation of 5.5 Hz . . . . . | 55 |
| 31 | Actual and simulated EEG spectra during flash stimulation of 7.5 Hz . . . . . | 56 |
| 32 | Autocorrelograms: solid curve from a typical EEG alpha waveform and dots from an autoregressive process fitted to the data . . . . . | 59 |
| 33 | A flowchart for the realization of the prediction scheme . . . . . | 68 |
| 34 | Actual and predicted waveform for lead time of 24 msec . . . . . | 69 |
| 35 | Actual and predicted waveform for lead time of 48 msec . . . . . | 69 |

| Figure Number | | Page |
|---|---|---|


| | | |
|---|---|---|
| 36 | Actual and predicted waveform for lead time of 60 msec | 70 |
| 37 | Actual and predicted waveform for lead time of 96 msec | 70 |
| 38 | Actual and predicted waveform for lead time of 120 msec | 71 |
| 39 | Prediction error variance vs. lead time | 71 |
| 40 | Computer derived scanpath superimposed on sketch of original scene | 74 |
| 41 | Sequence of foveal fixations | 75 |
| 42 | Scan of still life scene | 79 |
| 43 | Most probable transitions between cluster centers | 80 |
| 44 | Fovea-only visual field display | 84 |
| 45 | Peripheral visual field display | 84 |
| A.1 | View of subject in the head positioner with eye-tracker electronics | 90 |
| A.2 | View of eye-tracker optics and subject | 90 |
| A.3 | Requested fixation points | 93 |
| A.4 | Responses to requested fixation points | 94 |

# I. INTRODUCTION

This project has been aimed at the development and use of biocybernetic concepts and techniques for analyzing and developing skills that are essential for the enhancement of concrete images of the "eidetic" type. We have concentrated on the problem of achieving biocybernetic expansion of visual memory by using a closely-coupled man-machine system which performs real-time monitoring, analysis, and feedback of spatial and temporal cues that serve as keys to human memory encoding and recall. There is strong evidence that these cues are heavily depended on in memory encoding and retrieval by human nervous systems. The closely-coupled man-machine system is used for the measurement and prediction of human mnemonic performance to determine the spatial and temporal cues as well as for the control and enhancement of mnemonic skills. Such a man-machine system for visual memory tracking and training has been designed and is depicted in Figure 1. This system is capable of delivering optimal sequences of sensory stimulation conditionally related to eye position and brain state, and thus to explore systematically their relation to visual memory retrieval.

It is seen from the man-machine system that we emphasize the real-time monitoring and prediction of central nervous activities through the EEG signals and through the tracking of eye movement and eye fixations. Employing these real-time techniques, we have attempted to determine the temporal and spatial cues for human memory encoding and recall by monitoring of brain states and eye positions. Again, through this closely-coupled man-machine system, we utilize this information to arrange the desired coincidences between various brain states, eye positions, and

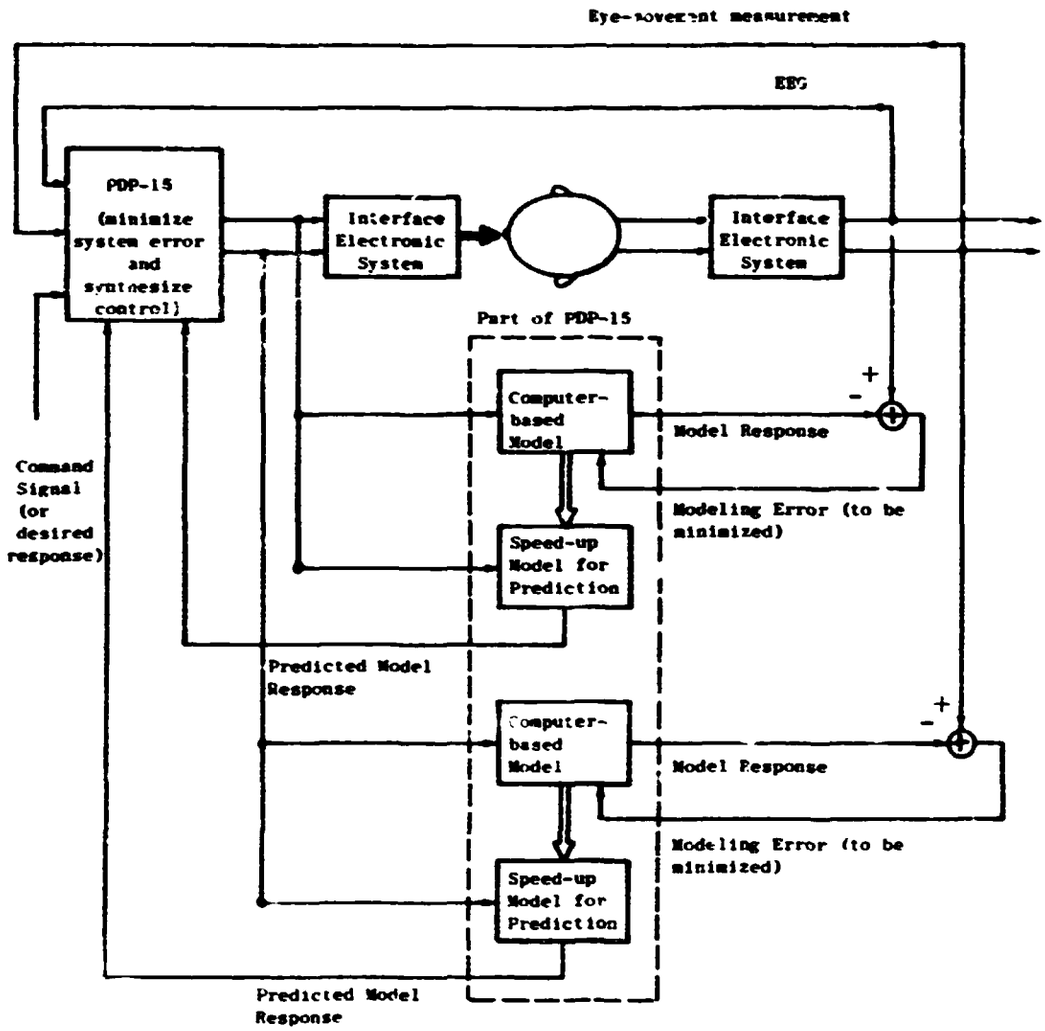


Figure 1 Block diagram of the closely-coupled man-machine system for monitoring and training of visual memory skills

the delivery of visual stimulation. The visual stimuli have been presented on projection screen or oscilloscope displays for binocular or monocular viewing. The eye movement was measured with the Biometrics' Eye Movement Monitor, Type SG; it is now measured with the Stanford Research Institute's (SRI) Cornsweet Eye Tracker. The brain states have been monitored through the EEG signals. It is expected that

greater control of image persistence and image dissipation can be obtained by combining these real-time monitoring and prediction techniques with a feedback scheme to close the control loop as depicted in the block diagram of the man-machine system. In other words, we strive to use the computer system to supplement and strengthen those deficiencies in human memory that ordinarily result in image dissipation based on the assumption that a superior scan pattern of visual inspection that results in a superior memory is more consistent and also less probable of natural occurrence than a visual inspection strategy that is less consistent. To summarize, we attempt to steer the subject toward improved encoding and decoding strategies for memory by using the techniques which have been developed and implemented on this man-machine system.

The closely-coupled man-machine system utilizes computer-based models in the system configuration to predict the kind of stimuli which should be used in order to produce the desired future responses. The EEG signals and the eye-movement measurement are shown as the responses which are closely controlled since the computer-based models are designed to mimic the actual physiological processes in regard to their stimulus-response relations. To be more specific, since the visual cues (stimuli) must be presented at appropriate locations in the visual field at the right instants of time, monitoring and prediction on real-time basis of both eye movement and EEG signals are essential. These models have been developed for the purpose of monitoring and prediction. We have completed the work on the computer-based models which will be described in detail in the following sections. These models have also been

implemented on the PDP-15. All of the man-machine system, except the interface electronic devices, can be realized on the PDP-15 computer. At the close of this project, we have implemented all but the feedback path of the man-machine system.

In order to determine the visual cues which serve as keys to both memory encoding an decoding, we have to characterize the scan patterns of observers during the inspection of scenes. With this quantitative characterization, we will then be able to differentiate quantitatively a superior scan pattern of visual inspection that results in a superior memory from an inferior one. This quantitative description is intended for use in the determination of those vital visual cues. We have developed and implemented a statistical method for the characterization of visual scan patterns. Our experimental results have established that observers with good visual memory, as scored by Marks' Visual-Memory Task, have a more consistent eye scan pattern in quantitative terms than those with poor visual memory. The characterization of the visual scan pattern and the related eye-movement measurement techniques will be discussed in Section IV.

Last, but not least, we will present a technique for the presentation of the visual cues (stimuli) at appropriate locations in the visual field at the right moments. Since our ultimate goal of this project is the visual memory enhancement through biocybernetic techniques, once the visual cues are determined, they can then be presented to the observer or trainee using our technique. In other words, this computer-implemented technique will enable us to deliver visual stimulation to coincide with the desired brain states and eye positions since it controls, in real-time

the monocular field of view of an observer inspecting outline drawings of visual scenes on a graphical CRT display. The details will be discussed in Section V.

In Section VI, we shall summarize our accomplishments and make concluding remarks. Some of these accomplishments have been published or presented in international scientific conferences. The list of publications relevant to this research project is included in Appendix B.

In summary, we have designed a closely-coupled man-machine system for the purpose of developing and use of biocybernetic techniques for analyzing and developing skills that are essential for the enhancement of concrete images of the "eidetic" type. This man-machine system has been implemented except the feedback path. In this system, we have developed models for EEG signals during visual stimulation and for eye movement during inspection of stationary scenes, respectively. These models are then used for the purpose of monitoring and prediction of various brain states and eye positions so that the desired coincidences between various brain states, eye positions, and the delivery of visual stimulation can be arranged. This arrangement of the desired coincidences can be carried out by a technique we developed and implemented. The electronic interface systems in the man-machine system serve a very important role in data acquisition and monitoring of the brain states and eye positions. These electronic interface systems consist of EEG recording machines with Grass preamplifiers, eye-movement measuring instrument (SRI Eye Tracker) and related interfacing hardware and software. We shall cover some of the unique features of the interface

systems in Appendix A. This report will conclude with Appendix B which includes: (1) a list of the names of those who have contributed to this project; (2) a list of all relevant papers that have been or are to be published; and (3) a list of lectures and talks given.

## II. ANALYSIS AND MODELING OF EYE MOVEMENTS DURING SCENE INSPECTION

In the closely-coupled man-machine system depicted in Figure 1, we have two boxes, each labeled as computer-based model; one is for eye movement and the other is for EEG signals. These computer-based models are used for monitoring and prediction of eye positions and various brain states, respectively. The monitoring of the eye positions is necessary for the determination of the spatial cues that serve as keys to visual memory encoding and retrieval and the prediction of eye position is essential for the presentation of these cues at the desired locations of the visual field. In this section, we shall discuss the development of such a model for eye movements during inspection of two-dimensional scenes.

### 1. An Algorithm for Automatic Identification of Fixations and Saccades

Eye movements during inspection of two-dimensional stationary scenes consist mainly of two components: fixations and saccades. The first step in our analysis of eye movements is to separate the data into these two components. We need to determine the beginning and end points of the fixations and saccades. This helps us to determine the sequence of fixations during a volitional scan of a two-dimensional scene. The separation of saccades from fixations is useful for the modeling to be described later. In the past, the delineation of fixations and saccades and the scoring of the fixation sequences has been done by hand. We have developed an algorithm which does this automatically and can thus reduce large amounts of raw eye-movement data to a sequence

of fixation points very quickly. With modifications, the algorithm can perform in real time. In addition, it gives us an objective method of data analysis as opposed to the earlier methods.

The detection of saccade onset is essentially a problem of signal detection. We can consider the movements during fixation as noise and the saccade as the signal. At any instant, we compute the quantities

$$R_x = \left|X_F - \sum_{i=1}^{k} \omega_i x_i\right| , \quad R_y = \left|Y_F - \sum_{i=1}^{k} \omega_i y_i\right|$$

where $(x_i, y_i)$ are sampled values of the horizontal and vertical components of the raw data; $(X_F, Y_F)$ is the location of the fixation; and $\{\omega_i\}$ is a weighting function of length $k$. The algorithm indicates the onset of a saccade at $t = 0$ if either $R_x > T$ or $R_y > T$, where $T$ is a preset threshold value; otherwise, the weighting window $\{\omega_i\}$ is moved forward. The threshold $T$ is a parameter of the algorithm which depends on the noise level in the measurement, the size of the smallest saccade that has to be detected, the amount of delay (k) allowed before detection, etc. This approach is essentially equivalent to using a matched filter since the weights $\{\omega_i\}$ are determined using the saccade model to be described later. Based on this model, we can determine the error probabilities for different size saccades and set $T$ accordingly.

We use a slightly different approach to determine fixations since the end of a saccade is usually much slower than its onset. Now we compute

$$n = \# \left\{ j : \left|x_j - \sum_{i=1}^{\ell} g_i x_i\right| < T_s \wedge \left|y_j - \sum_{i=1}^{\ell} g_i y_i\right| < T_s \ , \ 1 \le j \le \ell \right\}$$

where $\{g_i\}$ is an empirically determined weighting function and $T_s$ is a threshold value depending on the noise variance. In effect, we are

computing the number of points in a sample window of length $\ell$ which falls within a square of size $T_s$ around the window weighted mean $\left(\sum g_i x_i , \sum g_i y_i\right)$. The algorithm moves to the fixation state if $n$ exceeds a preset value $n_s (< \ell)$ ; otherwise, the sample window is moved forward. In practice, a simple averaging function is found to be adequate for $\{g_i\}$.

We have written a program to implement this algorithm. The program reads raw eye-data from the magtape and uses the algorithm to determine the fixation points. These are plotted and numbered. The program also outputs the starting and ending times and the standard deviations of each of the fixations. An example is shown in Figures 2, 3, and 4. Figure 2 shows the raw eye-movement data. Figure 3 shows the sequence of fixation points obtained from this algorithm, and Figure 4 shows the fixation points superimposed on the actual stimulus used. It is clear that a considerable data reduction has been achieved and the result is easier to understand and analyze. Other advantages of this algorithm include easy adaptation to different noise levels and/or measuring instruments by changing some parameters, and a quantitative estimation of error probabilities. In fact, the algorithm has been used quite successfully during the course of this project on data obtained from both the Biometrics unit and the SRI eye tracker by simply changing the thresholds.

## 2. Modeling of Saccadic Eye Movement

The next step in the analysis of eye movements is the investigation of saccadic movement. We need to be able to monitor and predict the

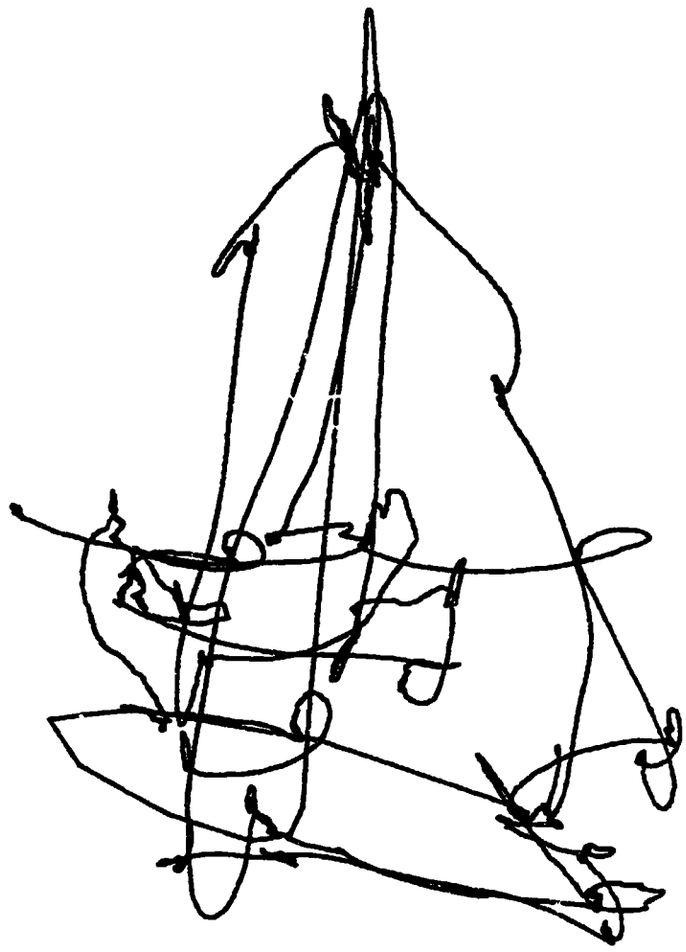

Figure 2 Raw eye movements for a 20-second scan. Scale = 2.5 deg/inch

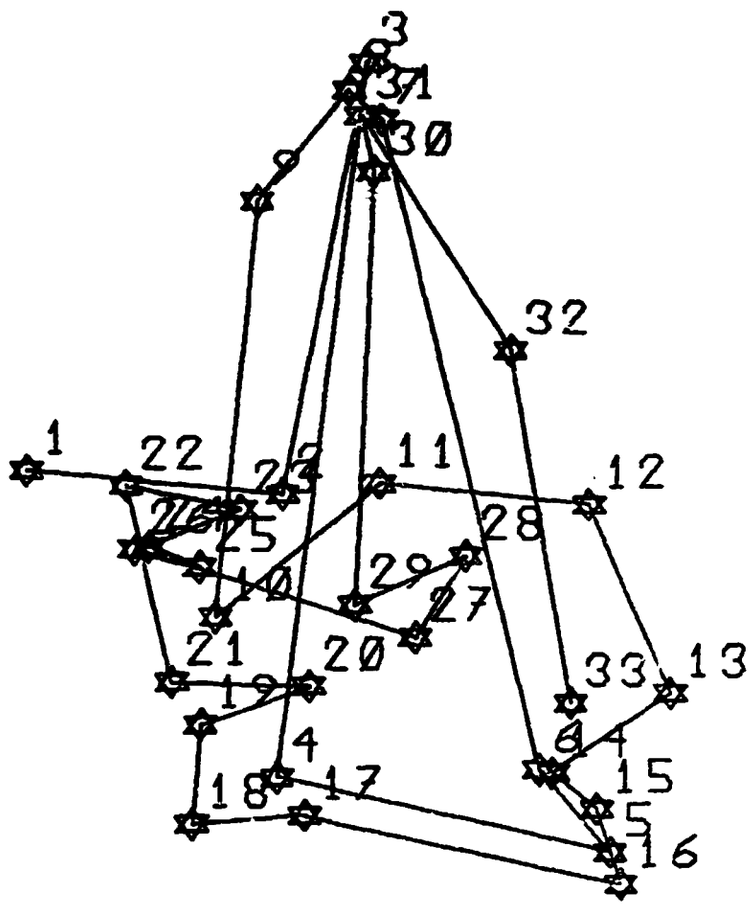


Figure 3 Fixation sequence for the scan in Figure 2

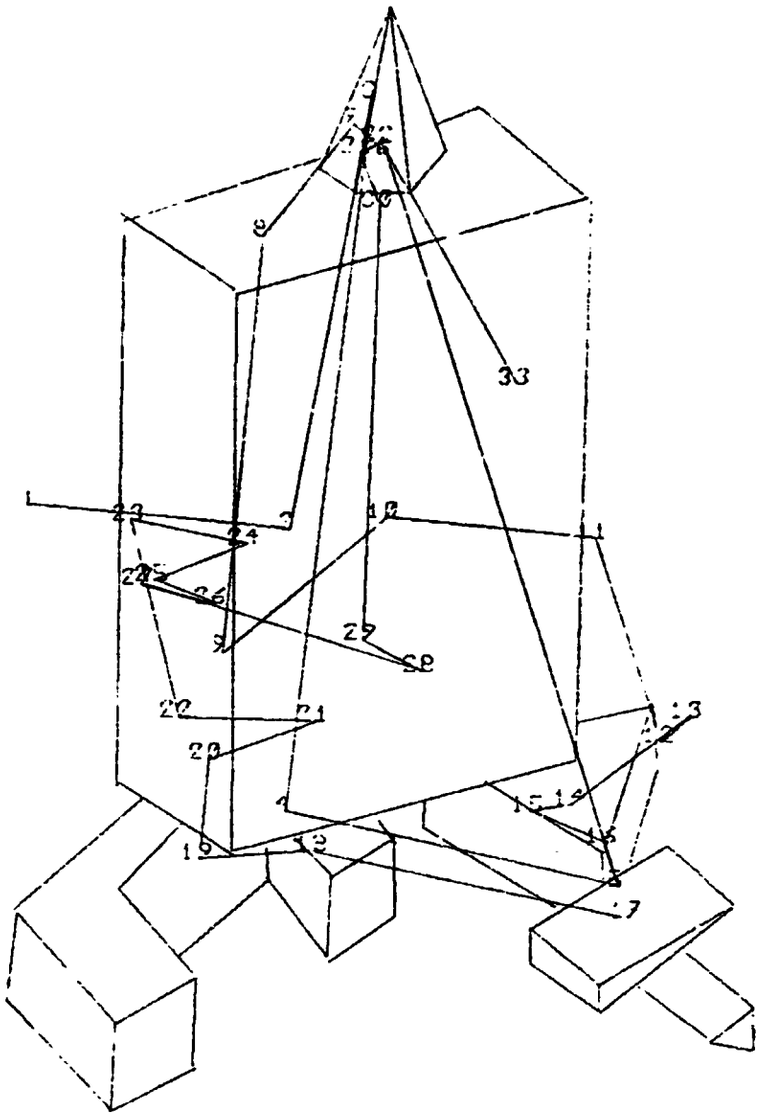

**Figure 4 Stimulus overlaid by the fixation sequence in Figure 3**

saccade duration and length in order to present visual cues (stimuli) at the appropriate locations in the visual field at the desired moments. Thus, the detailed dynamics of the saccadic movement are of interest to us. Hence, our approach is first to develop an appropriate model which embodies the dynamic characteristics of the saccadic system. This model is then utilized for monitoring and prediction of the saccadic movement.

The human saccadic eye-movement control system has been of great interest to researchers in neurophysiology and bioengineering. The general shapes of the position, velocity, and acceleration curves of the eye movement have been reported extensively. We have attempted to fit the model responses to empirical data by classical least-squares techniques. This enables us to estimate certain parameters of the model. These parameters which will be used for predicting the final eye positions have only been determined by indirect means in the reported models. We have also made important modifications to the model so that its output will accurately characterize the observed responses. We shall describe and discuss the model modifications, the parameter estimates, the curve-fitting results, and the use in monitoring and prediction.

For the present, we are concerned with horizontal eye movements only. For this purpose, an experiment for the study of horizontal saccades has been designed and used. A row of LEDs equidistantly located, only one of which is lighted at any given time, is used as stimulus. We will refer to the leftmost position as the rest position and the other six as the target positions. The target signal is supplied by a digital computer. The subject is instructed to follow the light spot, which repeatedly jumps from the rest position to one of the target

positions and back. The successive target positions are chosen from a table of random permutations to avoid anticipation by the subjects. An interval of at least 1 second is provided between each position change. Eye movements are recorded and stored as described elsewhere in this report.

Using the algorithm described above, we first mark the starting points of the saccades. Then the saccade position and velocity are plotted and equal length saccades are averaged with each sample lined up at the start. As an example, we show position and velocity plots of a typical saccade in Figure 5 and the averaged plots from 25 saccades of one subject in Figure 6. The saccades observed agree with those reported by other researchers in all aspects such as duration, overshoot, response delay, etc.

In order to monitor and predict the saccadic eye movements, we intend to fit the model output to the saccade position data by estimating the model parameters from the data. The endpoint of the saccade can then be predicted from the model output by using these parameters.

Let the horizontal position $x$ at time $t_i$ after the onset of the saccade be

$$x_i = \theta(a_1, a_2, \ldots, a_k; t_i) + n_i \qquad (1)$$

where $a_1, a_2, \ldots, a_k$ are the model parameters and $n_i$ is the noise term which represents the errors introduced by the instrument, the data collection errors, the inherent random nature of the biological system, etc. We shall use the least-squares estimation to determine $a_1, a_2, \ldots,$

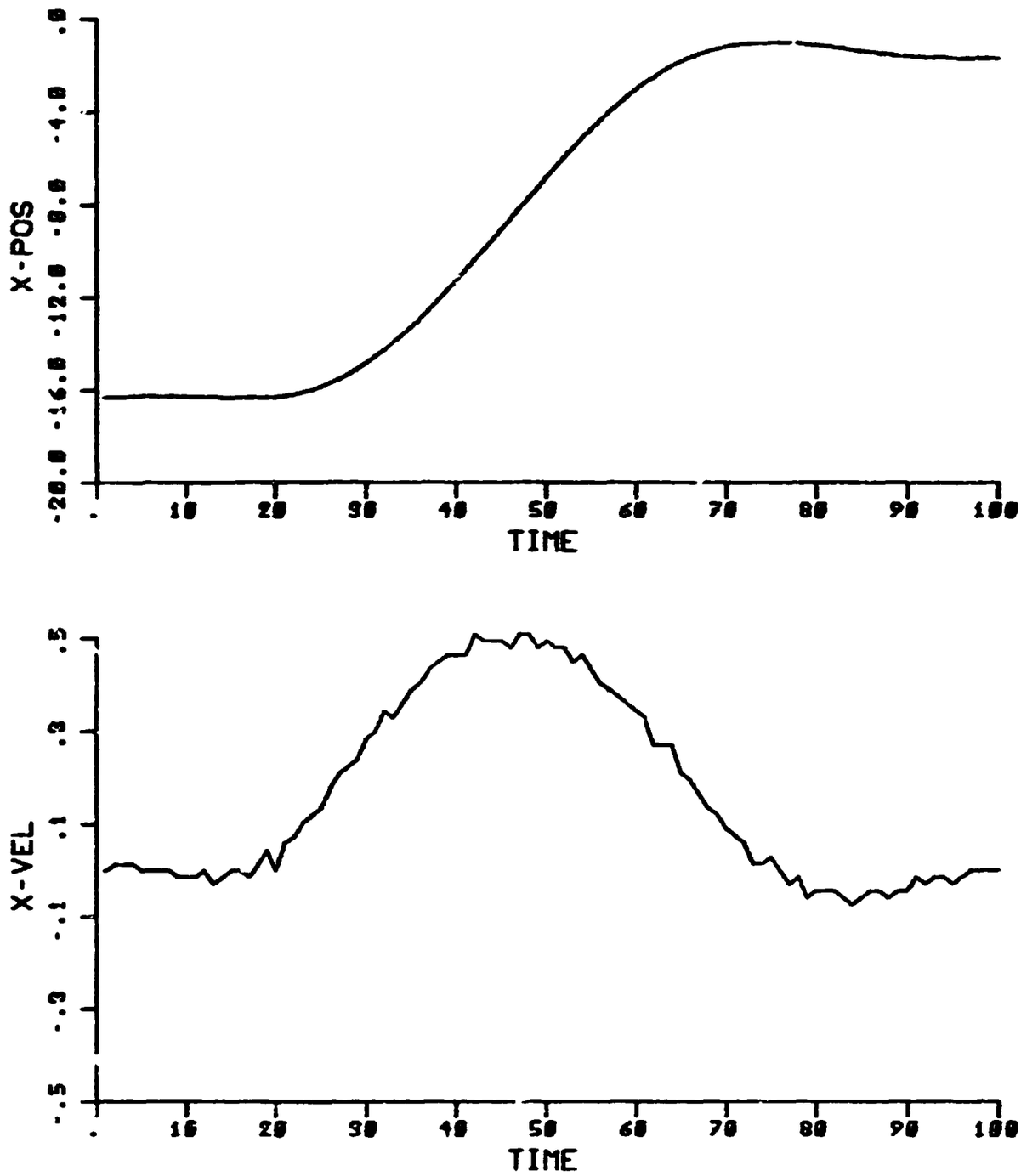


Figure 5 Typical position and velocity plots of a 15° . ccade

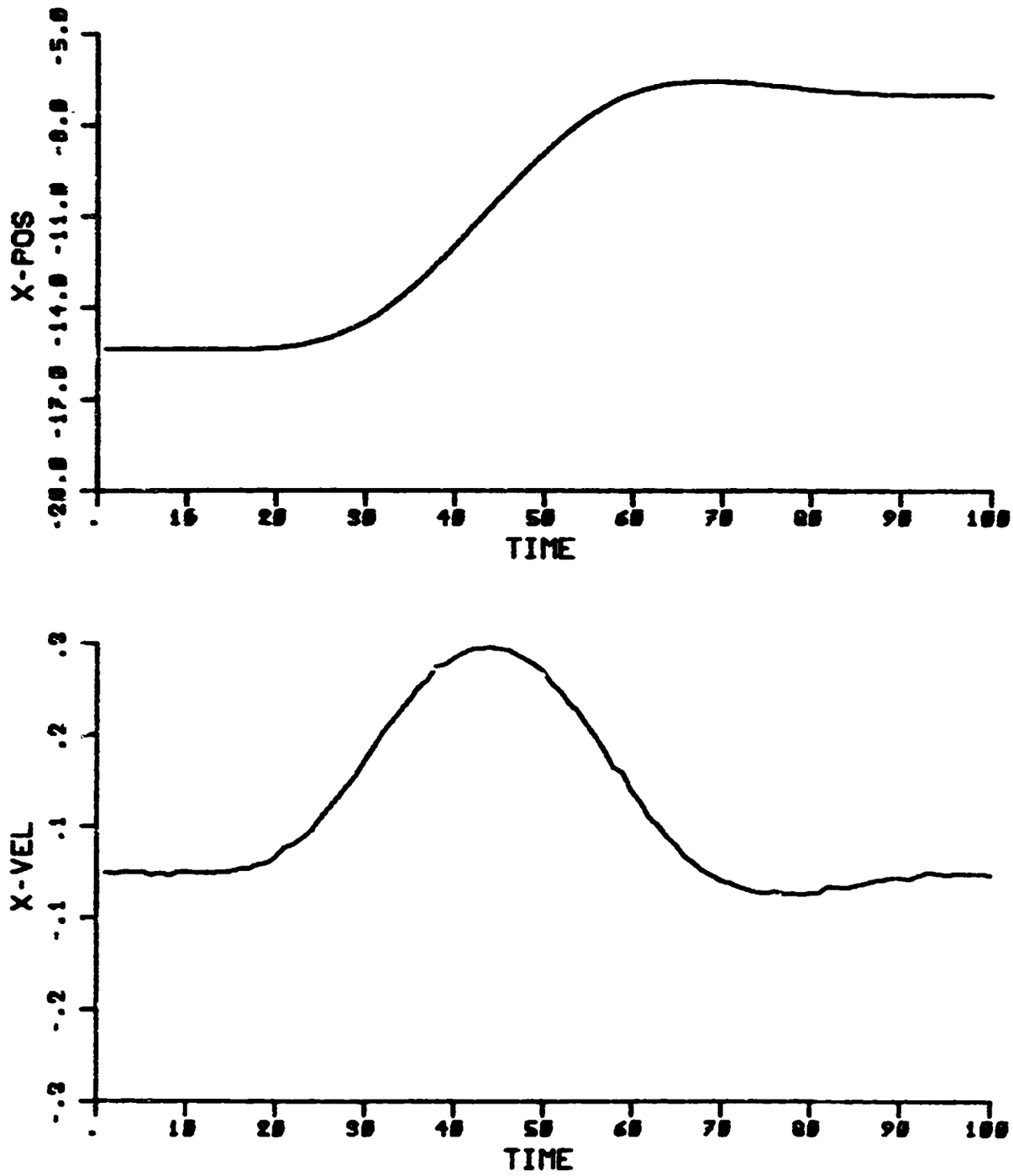


Figure 6 Averaged plots from 25 saccades of 10° amplitude

$a_k$ . They are determined by minimizing the mean-square error

$$S = \sum_{i=1}^{n} \left[ x_i - \theta(a_1, a_2, \ldots a_k; t_i) \right]^2$$

where $n$ is the number of samples observed; i.e., by solving the set of equations

$$\begin{aligned} \frac{\partial S}{\partial a_1} &= 0 \\ \frac{\partial S}{\partial a_2} &= 0 \\ &\vdots \\ \frac{\partial S}{\partial a_k} &= 0 \ . \end{aligned} \tag{2}$$

In the case when $\theta$ is a linear function of the parameters $a_1, a_2, \ldots, a_k$, Eq. (2) is reduced to a set of linear equations which can be solved to obtain the parameter estimates. If $\theta$ is nonlinear, then an iterative process has to be applied in order to solve for $a_1, a_2, \ldots a_k$ .

If we assume the noise $n_i$ to be white Gaussian, the least squares estimates are known to be identical to the maximum likelihood estimates which are unbiased, consistent, and asymptotically efficient. With the above assumption, we can also estimate the variances of the parameters and use $\chi^2$-test and t-test for goodness of fit. This gives us a quantitative measure of the goodness of our model.

The functional form for $\theta$ is determined by the particular model used. It undoubtedly relates to the dynamics of the eye-movement system. We have chosen to use Robinson's model for its simplicity. This model is block diagramed in Figure 7.

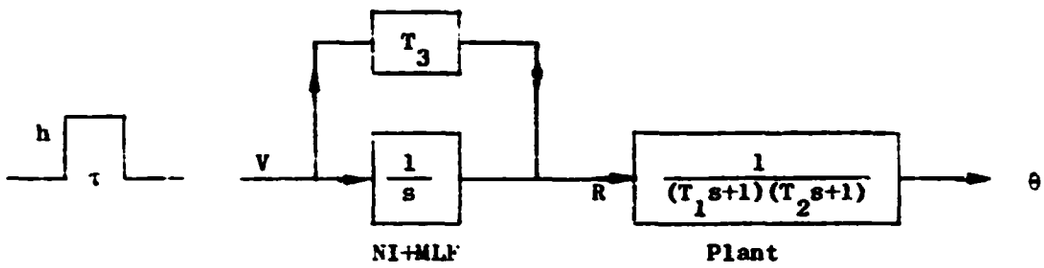


Figure 7 A model characterizing dynamic properties of saccadic eye movement

Here we have shown the dynamic part of the model only; the controller part is left out. The input to the system is a pulse of height $h$ and width $\tau$. This produced a saccade of amplitude equal to the area under the pulse; i.e., $h\tau$. NI is the neural integrator and MLF the medial longitudinal fasciculus which is a feed forward path in parallel with the integrator and provides a lead network to compensate for the plant lag. $R$ represents the oculomotoneuron firing rate. For a pulse input, we see that $R$ is a pulse step as desired. The plant is a second-order over-damped system with time constants $T_1$ and $T_2$. Robinson chose the MLF gain $T_3 = T_1$. However, he suggested that in order to produce the observed overshoots and undershoots $T_3 > T_1$ and $T_3 < T_1$, respectively, should be used. For our purpose, we have decided to retain $T_3$ as a separate parameter. The output $\theta$ is the eye position. The complete transfer function is then

$$\frac{\theta}{V} = \frac{T_3 s + 1}{s} \quad \frac{1}{(T_1 s+1)(T_2 s+1)} \quad .$$

For the assumed pulse input, the output $\theta(t)$ becomes

$$\theta(t) = h\left[t + \left(T_3 - T_2 - T_1\right) + \frac{\left(T_1-T_3\right)}{T_1-T_2} T_1 e^{-t/T_1} + \frac{\left(T_2-T_3\right)}{T_2-T_1} T_2 e^{-t/T_2}\right], \quad t \le \tau$$

$$= h\left[\tau + \frac{\left(T_1-T_3\right)}{T_1-T_2} T_1 \left(e^{-t/T_1} - e^{-(t-\tau)/T_1}\right) + \frac{\left(T_2-T_3\right)}{T_2-T_1} T_2 \left(e^{-t/t_2} - e^{-(t-\tau)/T_2}\right)\right], \quad t > \tau \quad . \tag{3}$$

The position and velocity curves given by the above for $h = .5$ deg/ms and $\tau = 20$ ms corresponding to a 10° saccade are shown in Figure 8. The values of the other parameters used are $T_1 = 150$ ms and $T_2 = 7$ ms. (These values are suggested by Robinson.) Curves are shown for $T_3 = 190$ ms, 150 ms, and 110 ms. Note the overshoot and undershoot for $T_3 > T_1$, and $T_3 < T_1$, respectively.

Note that there are four unknown parameters, $h$, $T_1$, $T_2$, and $T_3$. For estimation, we have to solve Eq. (2) for $k = 4$. However, from the theoretical evaluation of the parameter variances, we found that the estimate of $T_1$ will have a very large variance. Thus, the estimate will not be very meaningful and hence, a fixed value of $T_1 = 150$ ms will be used. As will be seen later, this does not affect the results significantly. We have also found that, for reasons of numerical calculation, it is better to estimate $T_3/T_1$ than $T_3$ itself. Thus, three parameters $a_1 = h$, $a_2 = T_2$, and $a_3 = T_3/T_1$ were estimated by using the data from $t_0$ to $t_0 + \tau$, where $t_0$ is the time of the onset of the saccade and $\tau$ is the input pulse width which is estimated from

the saccade velocity by noting that the velocity reaches a maximum at $t_0 + \tau$ as shown in Figure 8. The estimated parameters are then substituted into Eq. (3) to obtain the complete saccade curve and the prediction of the final position is made simply by extrapolation.

Typical results from the parameter estimation and prediction schemes are shown in Figures 9 and 10. The model output matches the actual data quite closely. The goodness of fit has been tested using the $\chi^2$-test on the sum of the squares of the residuals, $S$, and the t-test on the individual residuals at significance level $P = .05$. Note that the estimates of $T_2$ are 10.9 ms and 13.6 ms as opposed to the value suggested by Robinson. This result is typical and the mean value of $T_2$ is about 13.0 ms, although it varies between subjects. It is, however, significantly different from 7 ms. $T_3/T_1 > 1$ is observed in most cases, although the difference is not significant as far as the final value prediction is concerned. The values of $h$ and $\tau$ depend on the saccade size which implies that the size is controlled by both the amplitude and the width of the pulse. The exact relationship is being investigated.

In most responses, an overshoot of the final position was observed. This overshoot is not produced by the model, as can be seen in Figures 9 and 10. Even if we vary $T_3$, the overshoot could not be produced. This is because for $T_3 > T_1$, the overshoot decays with a time constant $T_1$, whereas the actual overshoot decays much faster (at about the same rate as the initial rise). In addition, we could not fit the model response beyond $\tau$ to the observed data within the chosen significance level $P = .05$. This indicates that the model must be modified to

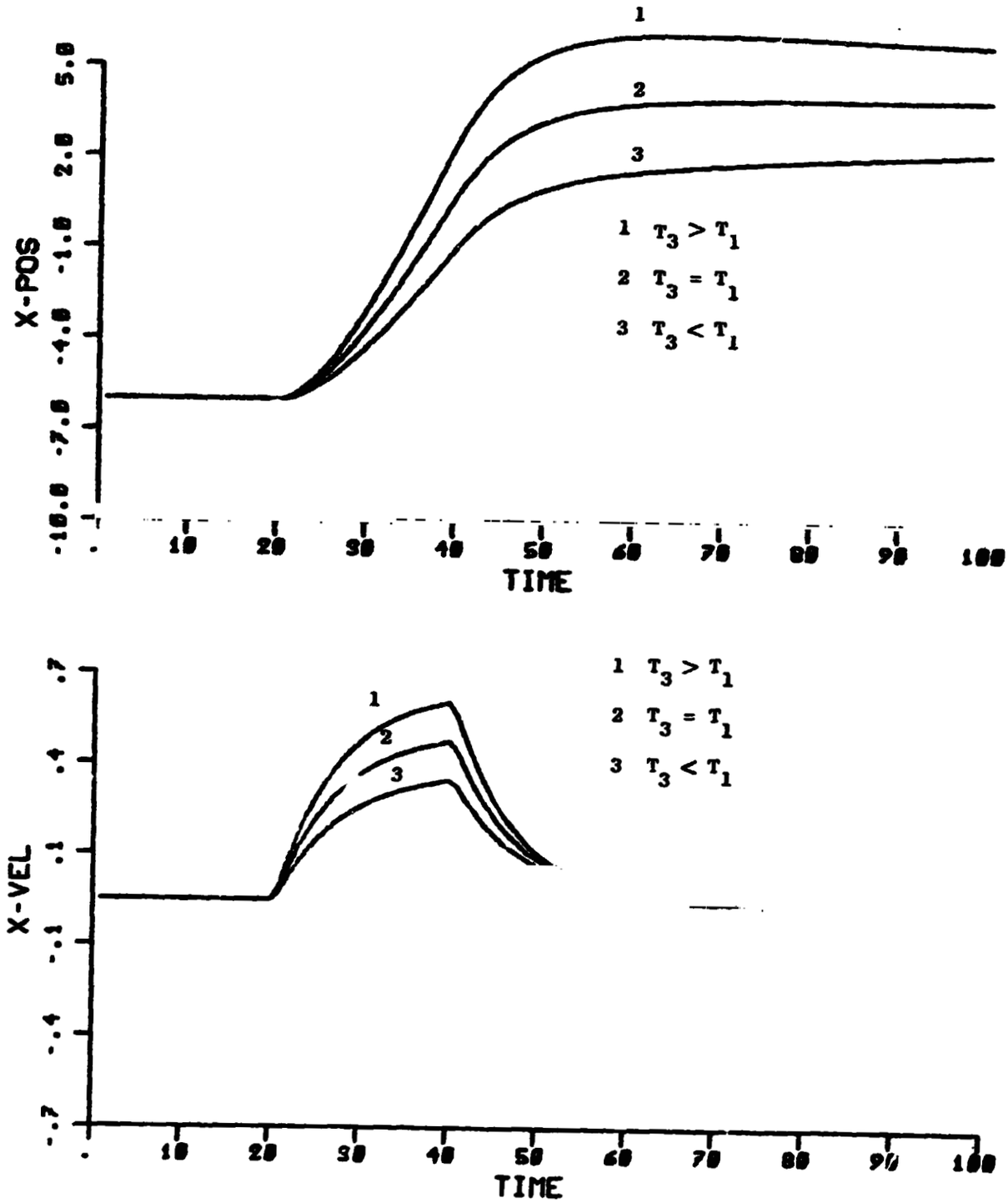


Figure 8 Model response for $T_1$ = 15[illegible] ms, $T_2$ = 7 ms, $\tau$ = 20 ms, h = .5 deg/ms, $T_3$ = 190, 150, 110 ms

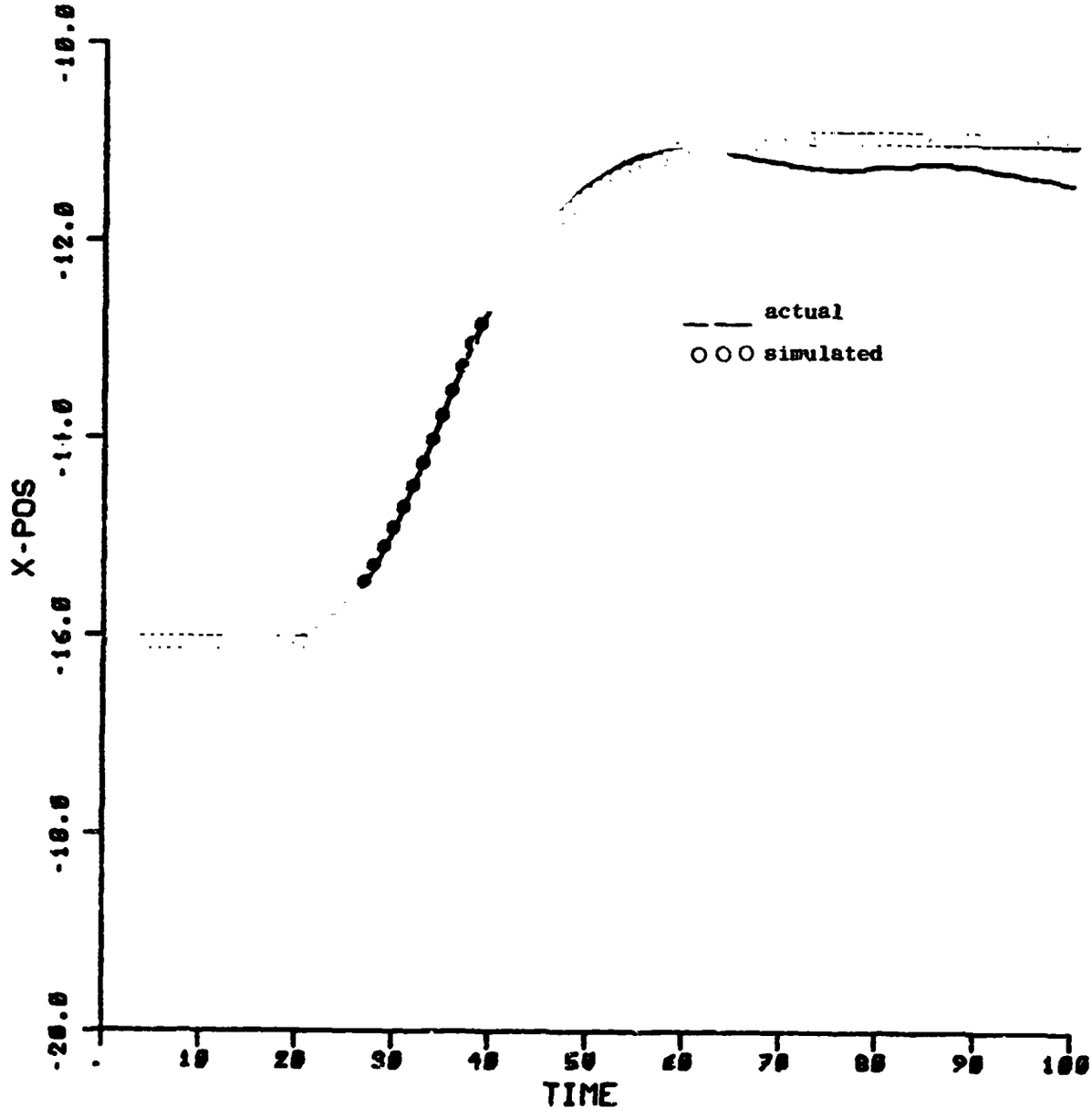


Figure 9 Actual and model simulated saccade position

$t_0$ = 20 ms, $T_1$ = 150 ms, $T_2$ = 10.9 ms,

$T_3$ = 160.5 ms, $\tau$ = 16 ms, h = .28 deg/ms

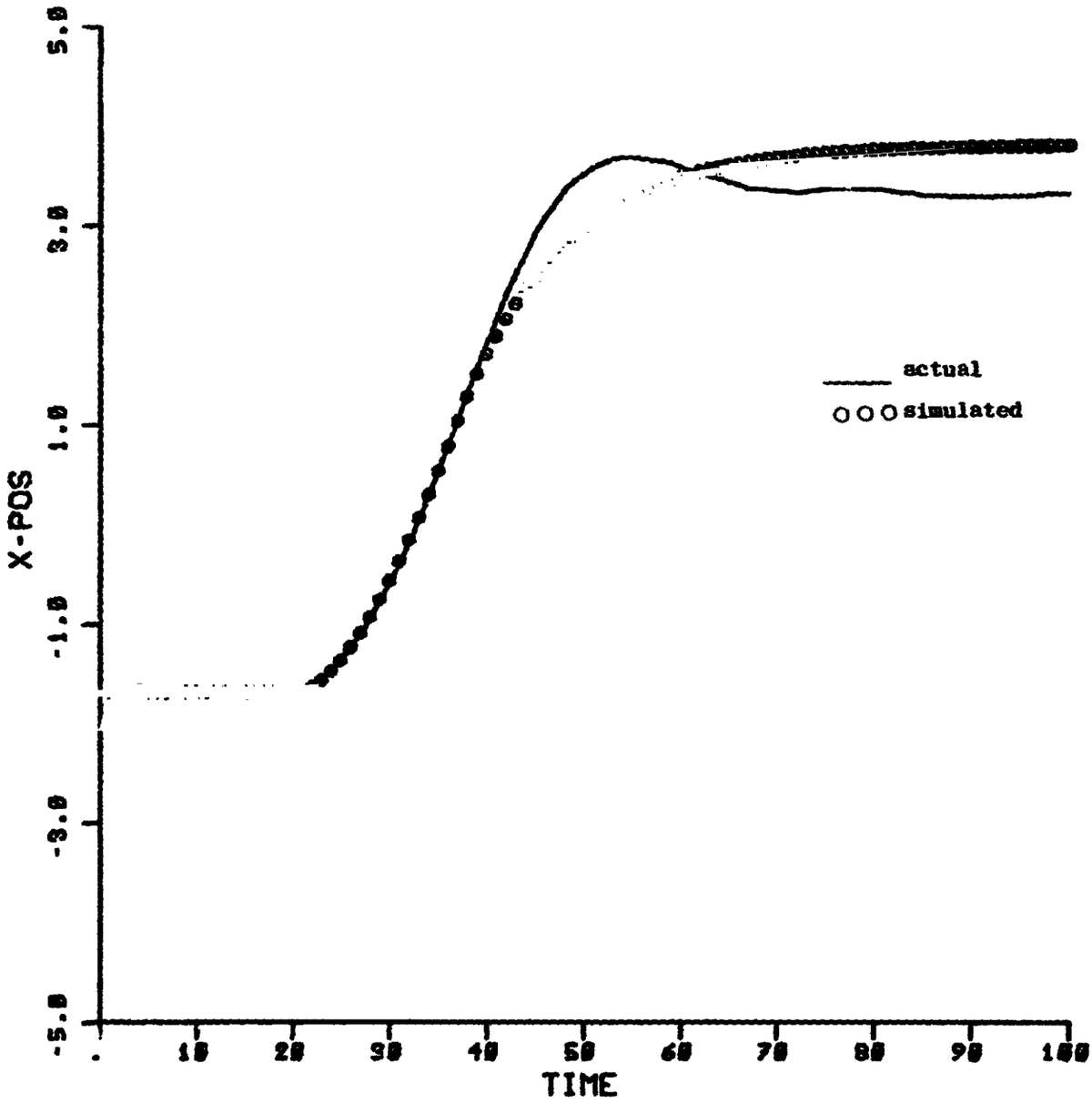


Figure 10 Actual and model simulated saccade position
$t_0$ = 20 ms, $T_1$ = 150 ms, $T_2$ = 13.6 ms,
$T_3$ = 168.2 ms, $\tau$ = 24 ms, h = .39 deg/ms

produce the right response. The fact that the overshoot decays with a time constant of about $T_2$ and the input to the agonist and the antagonist muscles used by Clark and Stark suggests that the input to the model consists of a combination of pulses rather than a single pulse. A study of the velocity curve in Figure 6 also suggests that a positive pulse followed by a negative pulse can produce the desired output. Thus, our model input is changed to two pulses as shown below:

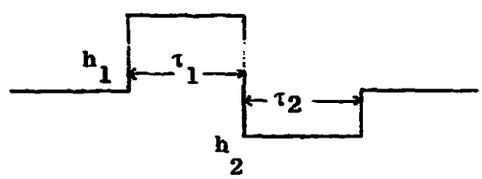


where the saccade amplitude = $h_1\tau_1 + h_2\tau_2$ . More generally, we can use p pulses with saccade amplitude equal to

$$\sum_{i=1}^{p} h_i \tau_i \quad .$$

In practice, we found that no more than three pulses were ever necessary.

The results of this modification are seen in Figures 11 and 12. For all multi-pulse input fits, $T_3 = T_1 = 150$ ms was assumed. Figure 11 shows the results of estimation from a single pulse input. Figure 12 shows the same saccade with the model output from a two-pulse input keeping other parameters the same as before. The fit in the second case is clearly much better. Figure 12 also shows the fit of the velocity curves from the data and from the model. Thus, excellent fits are obtained to both the position and velocity curves with this model. Figure 13 shows a much more dramatic result where a three-pulse input to the model is used. The justification for using such an input can be clearly seen from the velocity curve which first rises to a maximum

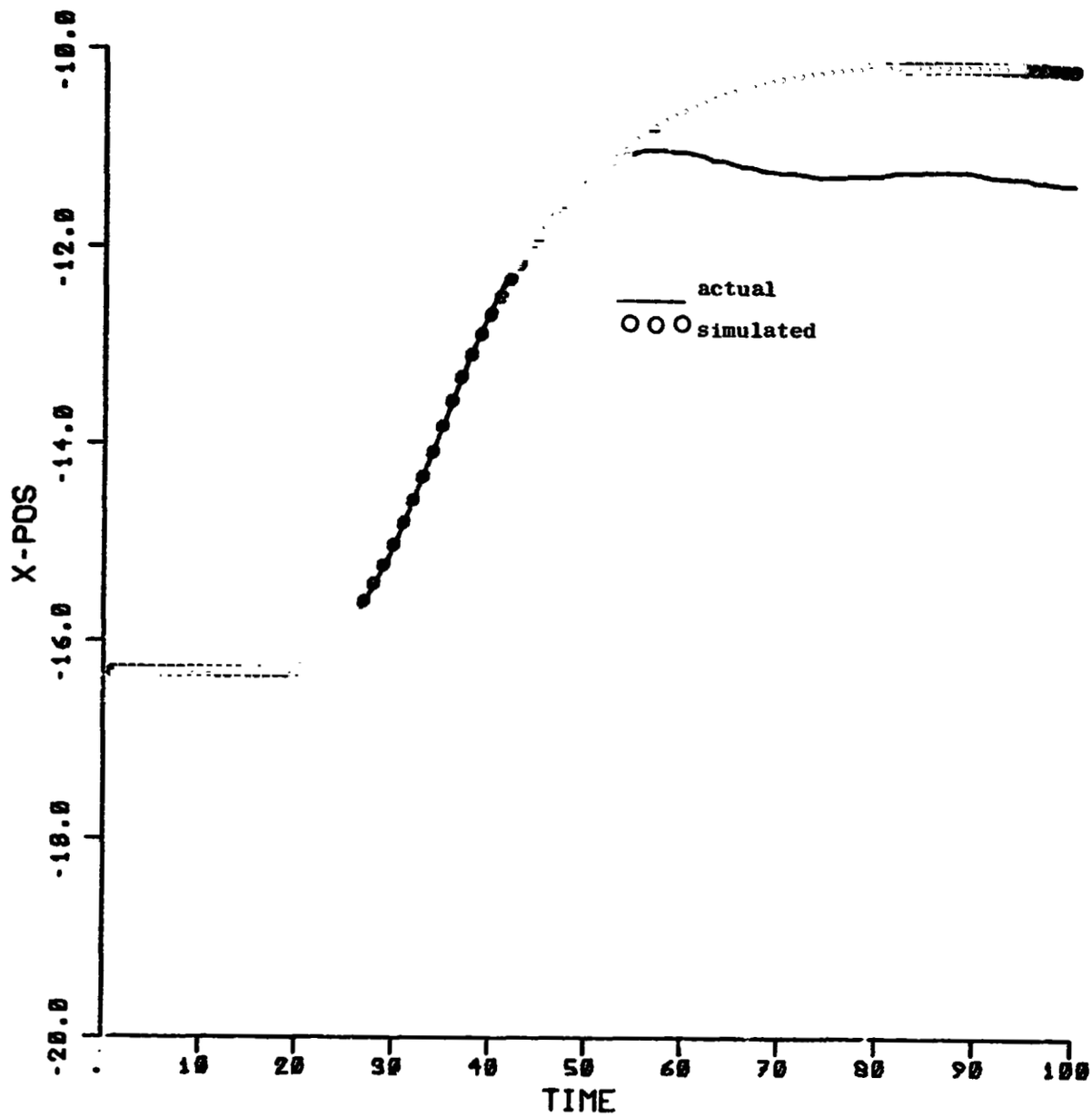


Figure 11 Actual and model simulated saccade position
$t_0$ = 20 ms, $T_1$ = 150.0 ms, $T_2$ = 13.1 ms,
$T_3$ = 150.0 ms, $\tau$ = 18 ms, h = .36 deg/ms

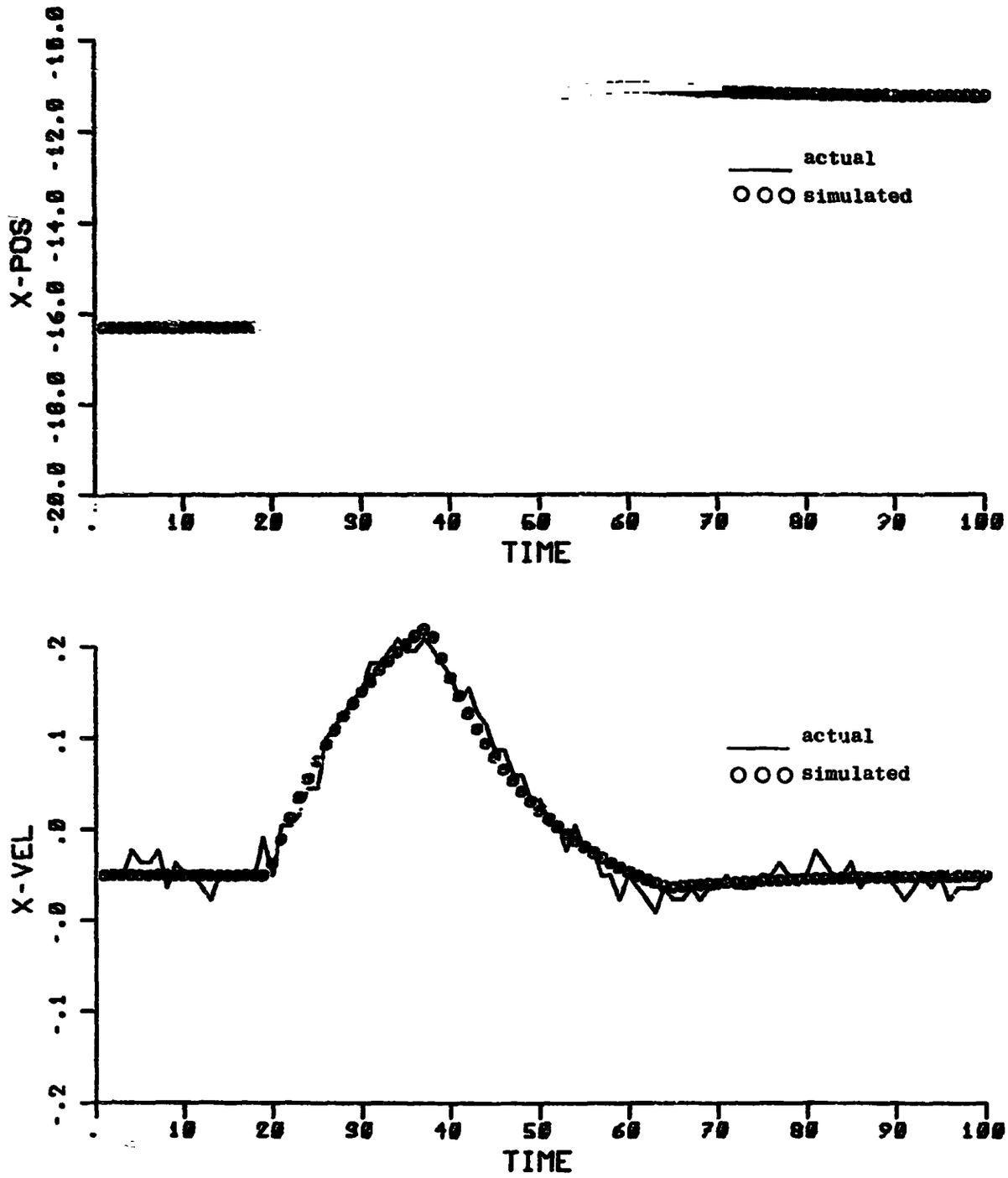


Figure 12 Actual and model simulated saccade position and velocity with two-pulse input

$t_0$ = 20 ms, $T_1$ = 150 ms, $T_2$ = 13.1 ms, $T_3$ = 150 ms, $\tau_1$ = 18 ms, $h_1$ = .36 deg/ms, $\tau_2$ = 27 ms, $h_2$ = -.05 deg/ms

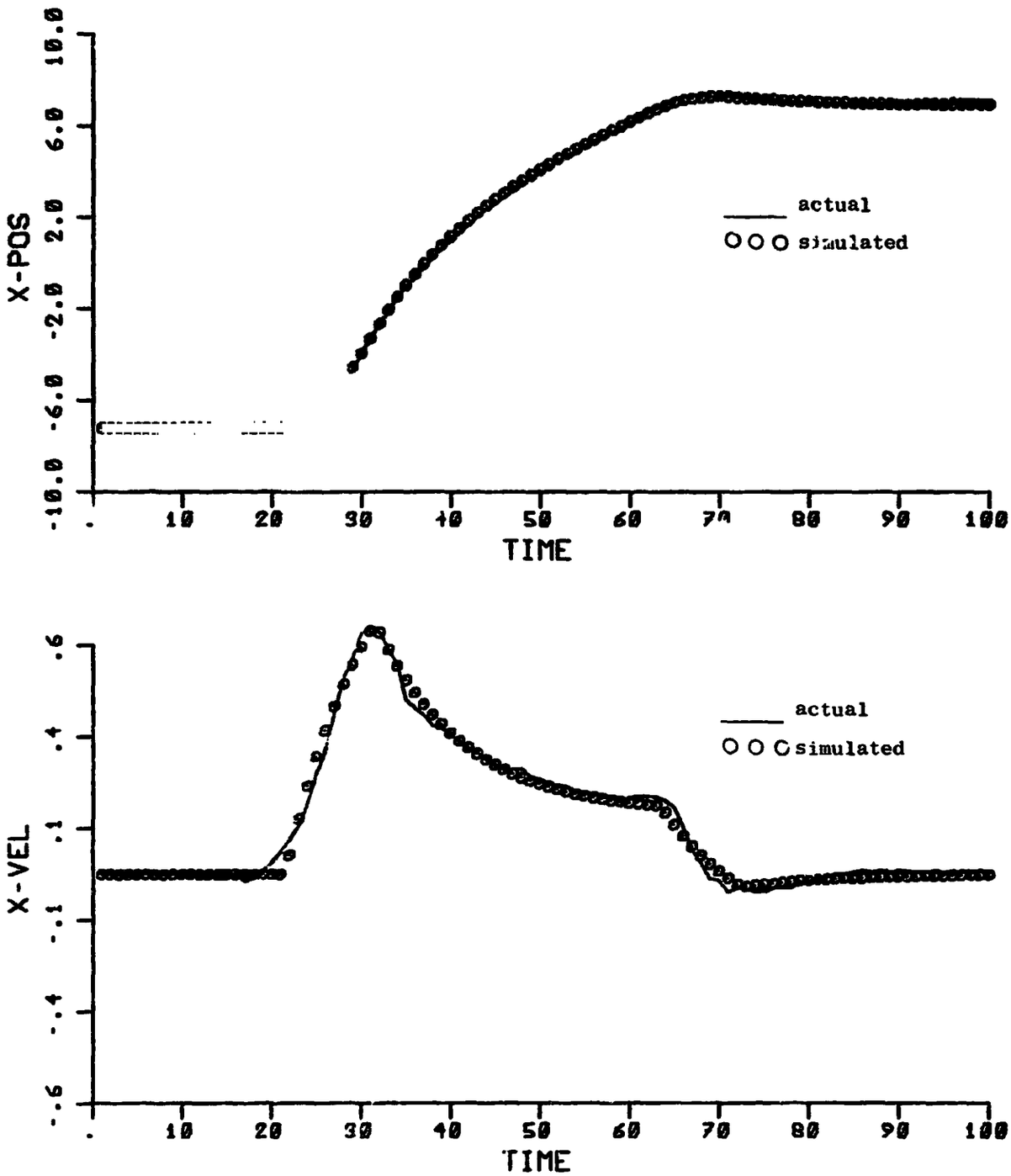


Figure 13 Actual and model simulated saccade position and velocity with three-pulse input

$t_0$ = 20 ms, $T_1$ = 150 ms, $T_2$ = 9.9 ms,

$T_3$ = 150 ms, $\tau_1$ = 10 ms, $h_1$ = 1.05 deg/ms, $\tau_2$ = 32 ms,

$h_2$ = .16 deg/ms, $\tau_3$ = 9 ms, $h_3$ = -.18 deg/ms

value, then approaches a steady positive value, followed by a rapid fall to a negative maximum and decay to zero. This identifies four distinct regions, suggesting four different input levels or three pulses (one level being zero). In fact, for the fitting, the pulse widths are identified by the instants where the velocity signal changes character. This would be easier to identify on a more noise-free system where the second derivative or acceleration can be observed. However, it is clear that the input is more complex than a single pulse. At present, we are trying to investigate the relationships between the heights and widths of the various input levels for different saccade lengths for the purpose of prediction. Similar responses are observed for equal length saccades which indicates that some identifiable relations exist. We are also trying to extend the results to vertical and oblique saccades.

The above approach is useful for prediction of the final position of the saccade, given a part of the saccade; i.e., we can use it for prediction only after a certain time has elapsed since the onset of the saccade. However, we also need to know when a saccade will occur in response to a stimulus. Normally, there is a delay of between 150 ms to 250 ms from the presentation of the stimulus to the saccadic response. If we can predict the actual delay, we can predict the course of the eye movements following the presentation of the stimulus by using this delay in conjunction with the above model. We decided to use information in the EEG alpha rhythm to predict the onset of the saccade. Gaarder et al. have shown that fixation saccades are initiated during a particular phase of the alpha. This is in accordance with Wiener's hypothesis that the alpha cycle serves as a clock which

provides timing for the data gathering and processing portions of the visual system. This result was obtained from microsaccades occurring during fixation. We want to determine if it applies for the large saccadic movements as well. If so, we can use an EEG-alpha-wave predictive scheme to predict the phase of the waveform and then use this information for estimating the onset of the saccade.

The same experiment as described earlier for studying horizontal saccades and in addition to record simultaneously the EEG signals collected as described in subsequent sections has been performed. The EEG was filtered in the alpha range. Two methods were used to determine the relation between the saccade onset and the alpha phase. First, the quadrant of alpha during which the saccade started was determined. The $\chi^2$-test was used to test the distribution of saccades in each of the four quadrants, which was found to be significantly different ($p < .05$) from a uniform distribution. This test is identical to the one used by Gaarder et al. In addition, the alpha was averaged with the saccade onsets lined up. Results indicate that there is indeed a preferable phase of the alpha rhythm for onset of the saccade. This fact can be exploited for the prediction of the onset of saccades if a scheme can be found for predicting the EEG alpha waveforms; espeically, their phasic variations. Such a method will be described in the next section.

## III. MODELING OF EEG SIGNALS DURING VISUAL STIMULATION AND PREDICTION OF EEG ALPHA WAVEFORMS

In order to determine the temporal cues that are important in visual memory, it is necessary to understand the relation between the temporal structure of visual perception and the EEG alpha cycle. To this end, we have investigated the changes produced in the EEG signal by simple visual stimuli. In particular, we are modeling and investigating the various EEG entrainment phenomena caused by periodic photic stimuli and the phasic changes in EEG due to photic stimuli. This will enhance our knowledge in several areas: it enables us to unify several seemingly different EEG phenomena under one principle, provides a model for the phase-dependency of stimulus efficiency, and enables us to study the phase-dependencies of onset times of saccades. A number of researchers have suggested that the alpha cycle is phase locked with a clock signal which provides the time base for a sampled-data system consisting of the eye, its control mechanism, and the visual cortex. The evidence for this has been accumulated slowly; it is known that visual perception times and reaction times are on the order of one alpha cycle and dependent upon the phase of the stimulus. In addition, some recent work has shown that a saccade is most easily initiated on certain phases of the alpha rhythm, which coupled with the fact that vision is blocked during a saccade, suggests that the alpha cycle delineates visual data sampling and processing periods.

The above discussion outlines the motivation for modeling the EEG signal during simple visual stimulation; the modeling efforts to date have been based on a simple nonlinear oscillator which is amenable to

analysis and simulation.

## 1. A Nonlinear Mathematical Model for Entrainment of EEG Signals by Periodic Photic Stimulation

The model is a van der Pol oscillator representing the behavior of a subject's EEG during periodic visual stimulation by a stroboscope or a set of LED goggles. The stimuli are delivered for 20 seconds at some fixed frequency followed by a 10-second stimulus-off period. This sequence is repeated for each desired stimulus frequency.

The van der Pol oscillator can be represented by

$$\ddot{x} - \mu\left(1 - x^2\right)\dot{x} + \omega_0^2 x = \omega_0^2 E(t)$$

where $x(t)$ denotes the EEG signal; $\omega_0$ is the unstimulated alpha frequency; $E(t)$ is the external excitation (stimulus); and $\mu$ is the nonlinear coupling coefficient.

When $E(t)$ is a sinusoid, a first approximation to the solution $x(t)$ can be made by a classical technique, such as harmonic balancing. The possible solutions can be classified in the following way when $E(t) = E_0 \sin(\omega_1 t + E_0)$:

(1) natural oscillation ($E_0$ is small):

$$x(t) = A \sin(\omega_0 t + \phi) \;;$$

(2) harmonic entrainment ($\omega_0 \approx \omega_1$):

$$x(t) = A(t) \sin(\omega_1 t + \phi(t));$$

(3) mth-order subharmonic entrainment ($m\omega_0 \approx \omega_1$):

$$x(t) = A(t) \sin\left(\frac{\omega_1}{m} t + \phi(t)\right) \;;$$

(4) nth-order superharmonic entrainment ($\omega_0 \approx n\omega_1$):

$$x(t) = A(t) \sin(n\omega_1 t + \phi(t));$$

(5) combined frequency oscillations (all other cases):

$$x(t) = A_0(t)\ \sin(\omega_0 t + \phi_0(t)) + A_1(t)\ \sin(\omega_1 t + \phi_1(t)).$$

Some initial data have been collected with a set of specially constructed LED goggles which provide a sinusoidally modulated intensity, and the results agree well with the above solution classes. However, since the experimental stimulus is often a train of flashes, we have developed an analysis technique for approximating the solution of the van der Pol equation when $E(t)$ is a pulse train.

We assume that the unperturbed oscillation $(E(t) = 0)$ is correctly represented by

$$x(t) = a_0 \sin \theta(t)$$

where the angular displacement can be written in terms of frequency and phase:

$$\theta(t) = \omega_0 t + \phi(t) .$$

We wish to examine the result of $E(t)$ being a series of impulses of strength $q$ at a frequency $\omega_1$ .

Following a method due to Blacquière, we can assess the perturbation caused by one impulse. At an angular displacement

$$\theta_n = \omega_0 t_n + \phi$$

we apply the nth impulse. Its effect will be seen directly in $\ddot{x}(t)$ , causing a small step change

$$\Delta\dot{x} = \int_{t_n}^{t_n+\Delta t} x(\tau)d\tau = q\,\omega_0^2$$

over time $\Delta t$ . However, $x$ will be continuous, so $\Delta x = 0$ .

To a first approximation, we can expand $\Delta x$ and $\Delta\dot{x}$ as below:

$$\Delta x = \Delta a \sin \theta_n + a_0 \Delta\phi \cos \theta_n = 0$$

$$\Delta\dot{x} = \Delta a\omega_0 \cos\theta_n - a_0\omega_0 \Delta\phi \sin\theta_n = q\omega_0^2$$

where $\Delta a$ represents the change in amplitude and $\Delta\phi$ represents the change in phase of the system. Solving the above equations simultaneously for $\Delta a$ and $\Delta\phi$, we obtain

$$\Delta a = q\omega_0 \cos\theta_n \ ,$$

and

$$\Delta\phi = -\frac{q\omega_0}{a_0} \sin\theta_n \ .$$

In Figure 14, we demonstrate the amplitude and phase perturbations as a result of an impulse falling on angular displacement $\theta_n$.

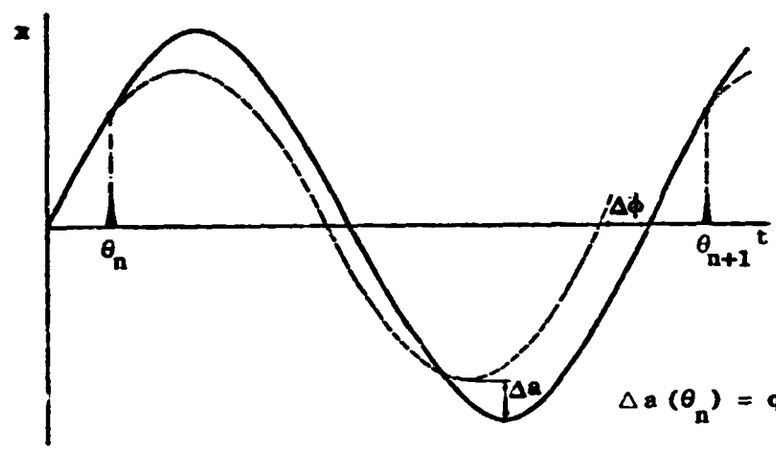


$$\Delta a(\theta_n) = q\omega_0 \cos\theta_n$$

$$\Delta\phi(\theta_n) = -\frac{q\omega_0}{a_0} \sin\theta_n$$

Figure 14 Phase and amplitude perturbations

The unperturbed solution would have followed the dashed line, and the perturbed solution follows the solid line.

In order to deal with a series of these impulses, $\Delta a$ will be assumed to be negligible. This is reasonable since a more detailed analysis shows that the amplitude change decays exponentially with time. Let $T_0 = \frac{2\pi}{\omega_0}$ and $T_1 = \frac{2\pi}{\omega_1}$ be the alpha and stimulus periods,

respectively. Then referring again to Figure 14, we see that applying the nth pulse at displacement $\theta_n$ results in a new displacement $\theta_n + \Delta\Phi(\theta_n)$ . Since the pulses are spaced $T_1$ seconds apart, the (n+1)th pulse will arrive at displacement

$$\theta_{n+1} = \theta_n + \Delta\Phi(\theta_n) + T_1 \quad .$$

Clearly, for entrainment to occur, we must have the congruence relation

$$\theta_{n+1} \equiv \theta_n \quad (\text{modulo } T_0)$$

or

$$\theta_n + \Delta\Phi(\theta_n) + T_1 \equiv \theta_n \quad (\text{modulo } T_0)$$

Hence

$$\Delta\Phi(\theta_n) + T_1 = k\, T_0 \ , \ k = 0, 1, 2, \ldots \quad .$$

When $k = 0$ , we have the unlikely situation of resetting the phase of oscillation; the required phase change $\Delta\Phi(\theta_n)$ is very large. We will not consider this case here.

For $k = 1$ , the solution is called harmonic entrainment, and for $k \geq 2$ , it is called $k^{th}$-order superharmonic entrainment, where $k$ represents the number of alpha periods elapsed per stimulus impulse. It is easy to show that this is stable near

$$\left|\theta_n\right|_{\text{mod } T_0} = 0 \ ,$$

as one would expect from the form of $\Delta\Phi$ .

In a similar fashion, for subharmonic entrainment to occur,

$$\theta_{n+m} \equiv \theta_n \quad (\text{modulo } T_0)$$

or

$$\theta_n + \sum_{i=n}^{n+m-1} \Delta\Phi(\theta_i) + mT_1 \equiv \theta_n \text{ (modulo } T_0) \quad .$$

Hence,

$$\sum_{i=n}^{n+m-1} \Delta\Phi(\theta_i) + mT_1 = T_0 \quad .$$

When $m = 1$ we have harmonic entrainment again, and for $m \geq 2$, $m^{th}$-order subharmonic entrainment occurs. The stability of this solution is currently being investigated, but it appears that for $m = 2$ a small stable range exists.

In summary, when the stimulus frequency is near the alpha frequency, harmonic entrainment is possible. When the alpha frequency is near an integer multiple of the stimulus frequency, superharmonic entrainment is possible. And when the stimulus frequency is near an integer multiple of the alpha frequency, subharmonic entrainment is possible.

When the stimulus frequency is not in one of the above ranges, combined frequency oscillations exist. Thus, we have the same five solution classes for both sinusoidal and impulsive stimuli. The major differences lie in the amplitudes required to produce the various effects, and in the fact that the impulsive stimulus will produce integer harmonics of its fundamental frequency due to its inherent harmonic content. Results obtained from EEG data on the model are described and compared in the next section.

## 2. Model Simulation

It is necessary to simulate the nonlinear oscillator model to

obtain reasonably accurate solutions since nonlinear analysis is by nature approximate. We are using a variable order differential equation solver (DVDQ) which has an Adams-Faulkner predictor and an Adams-Moulton corrector. It provides for up to twentieth order interpolation of output values positioned independently of the changing stepsize, which greatly facilitates signal processing of the simulated solution by allowing a constant sample period.

The sine wave stimulus is handled in a straightforward fashion, but the impulse train is treated specially. Since it is known analytically that the exact change in $\dot{x}(t)$ is $q\omega_0^2$ (by integration) at the time an impulse is called for, the state vector is perturbed and the integration restarted. The management of impulse arrival and sample output is performed by a discrete event-queuing scheduler on a priority basis; impulse arrival has priority over all events to avoid frequency shifts in the impulse train. Error propagation as a result of restarting the integration is linear with the requested error tolerance and adequately small.

Figures 15 and 16 show the phase and amplitude perturbations caused by a single flash landing on phases of 0 , $\pi/2$ , $\pi$ , and $3\pi/2$ radians. The simulations match the first order approximations developed in the previous section very well. These perturbations produce appropriate entrainment phenomena, as seen in the spectra of Figures 17 and 18; there is one spectrum for each stimulus frequency, representing 5.12 seconds of impulse driven simulation at a 100-Hz sampling rate. The five phenomena predicted in the previous section can be clearly seen; viz., harmonic entrainment, subharmonic entrainment, superharmonic

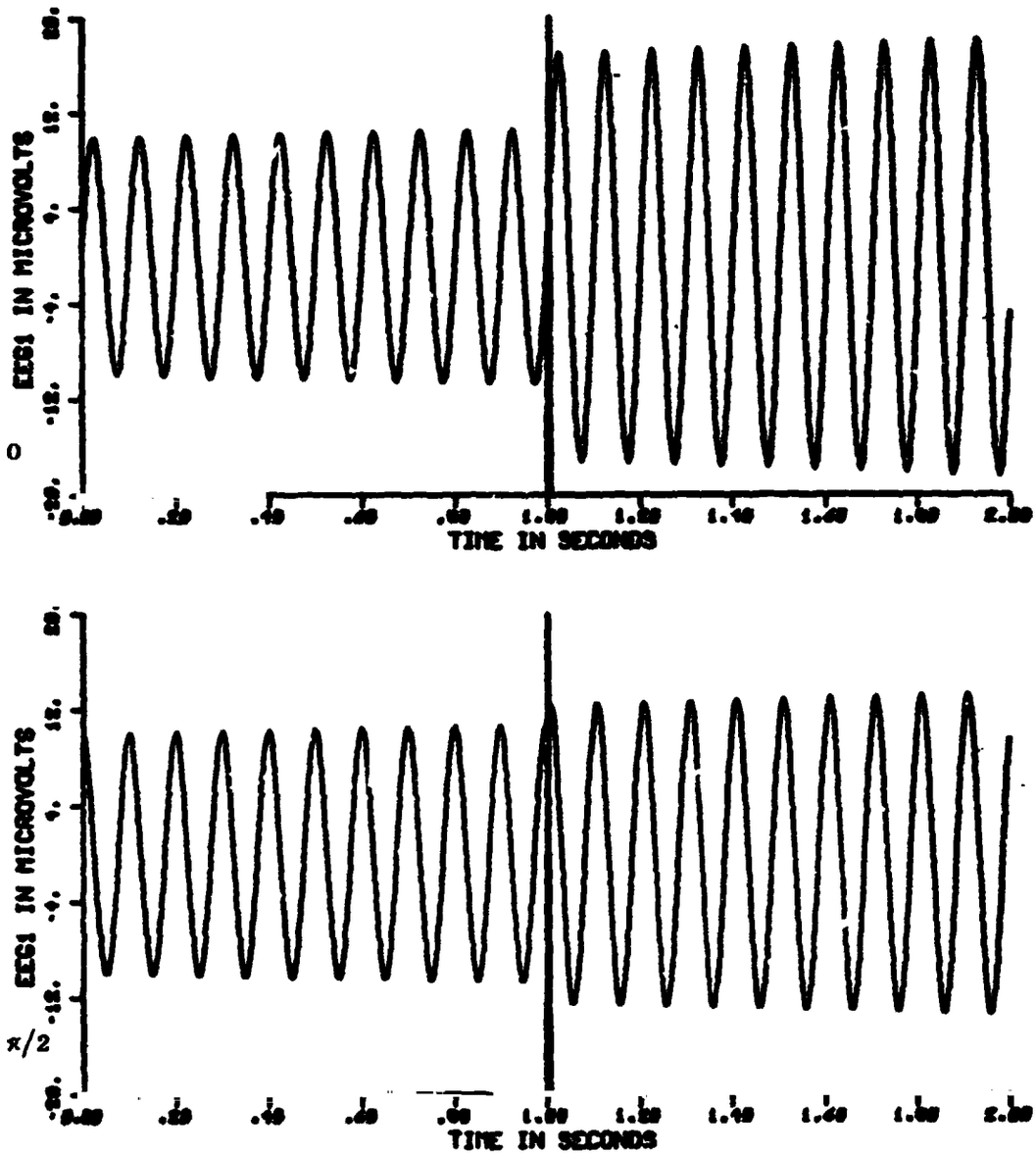


Figure 15 Simulated EEG perturbations resulting from flash at phases of 0 and $\pi/2$ radians

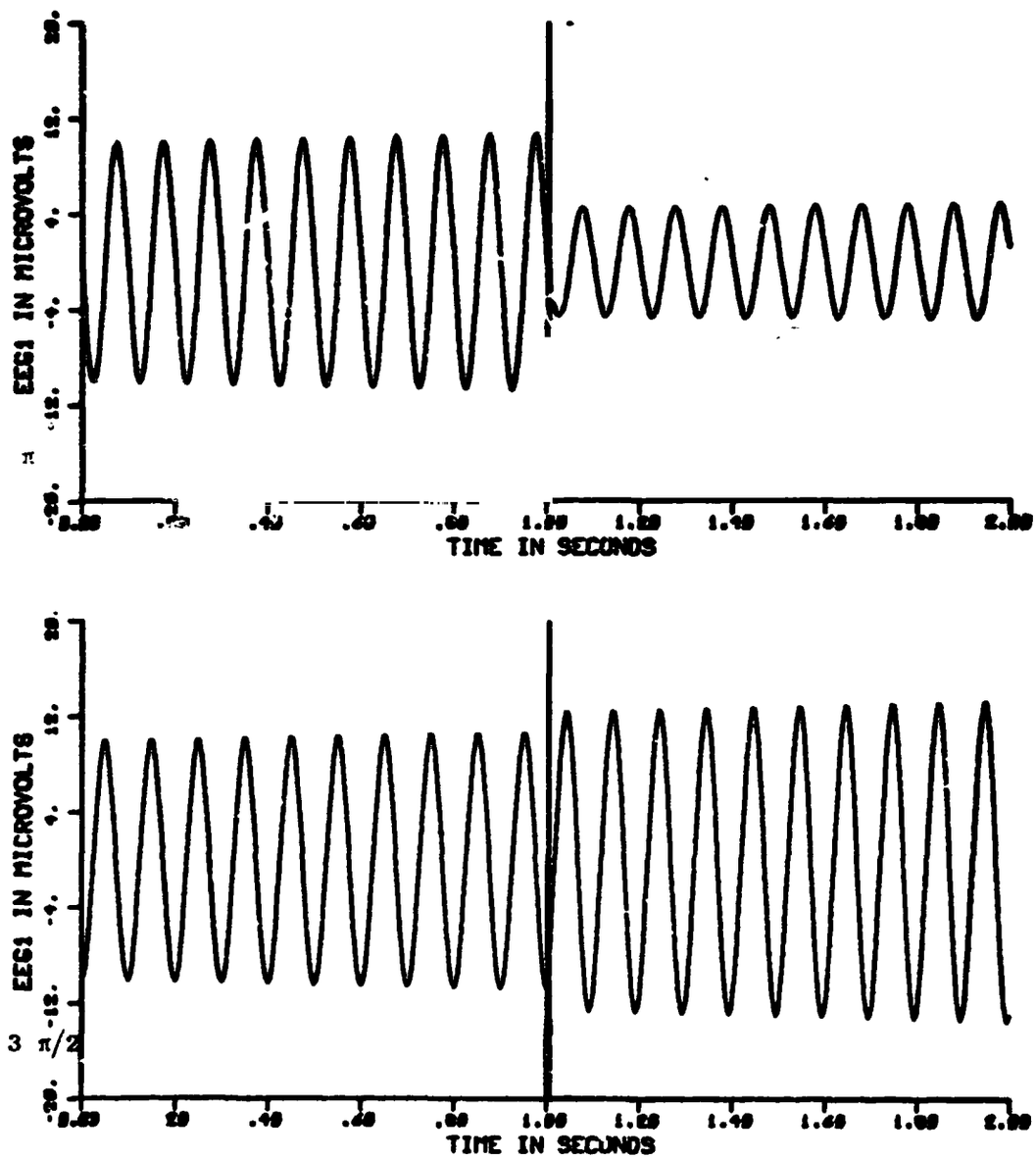


Figure 16 Simulated EEG perturbations resulting from flash at phases of π and 3 π/2 radians

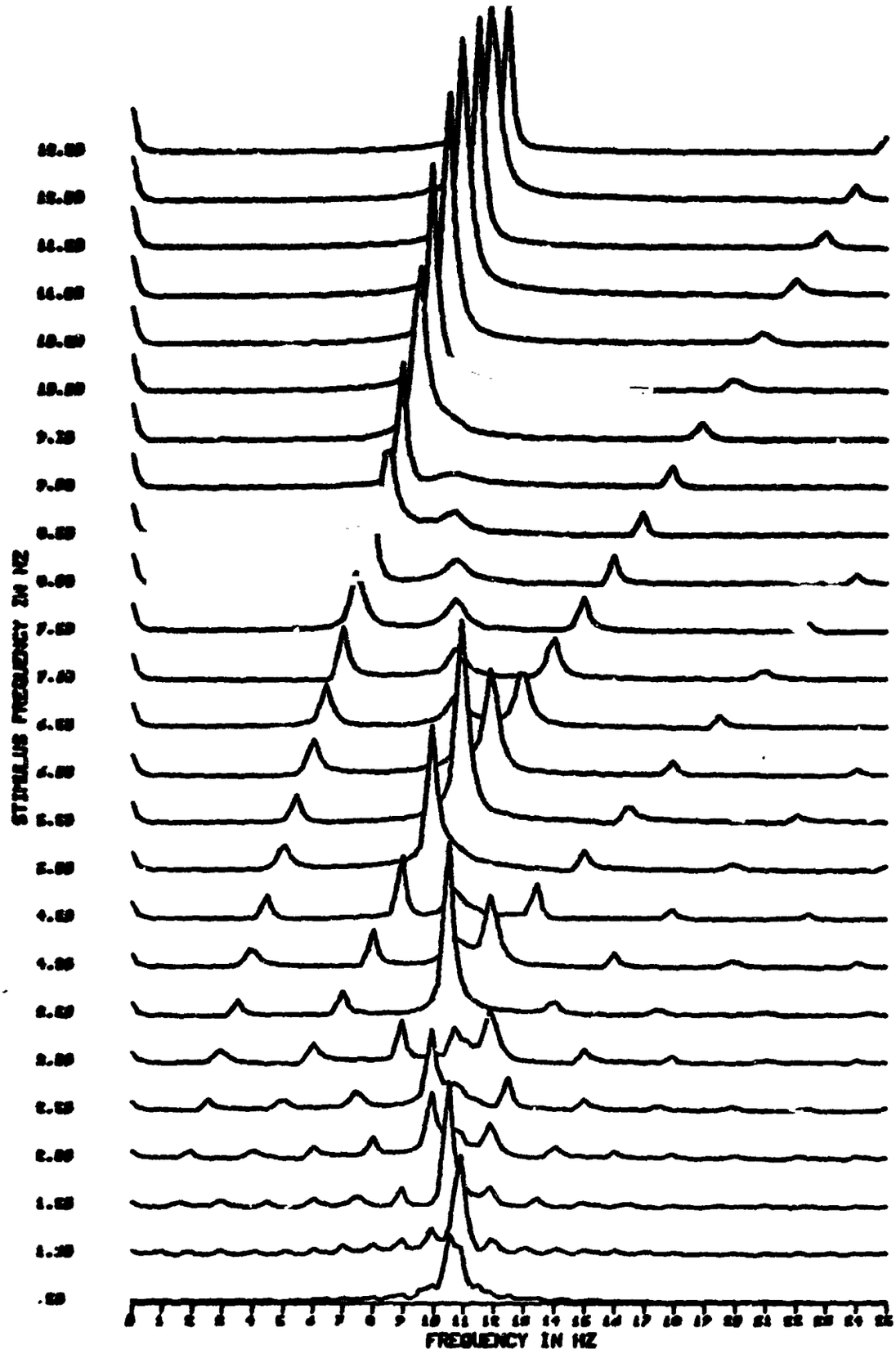


Figure 17 Simulated EEG spectra for flash frequencies from .5 Hz to 12.5 Hz

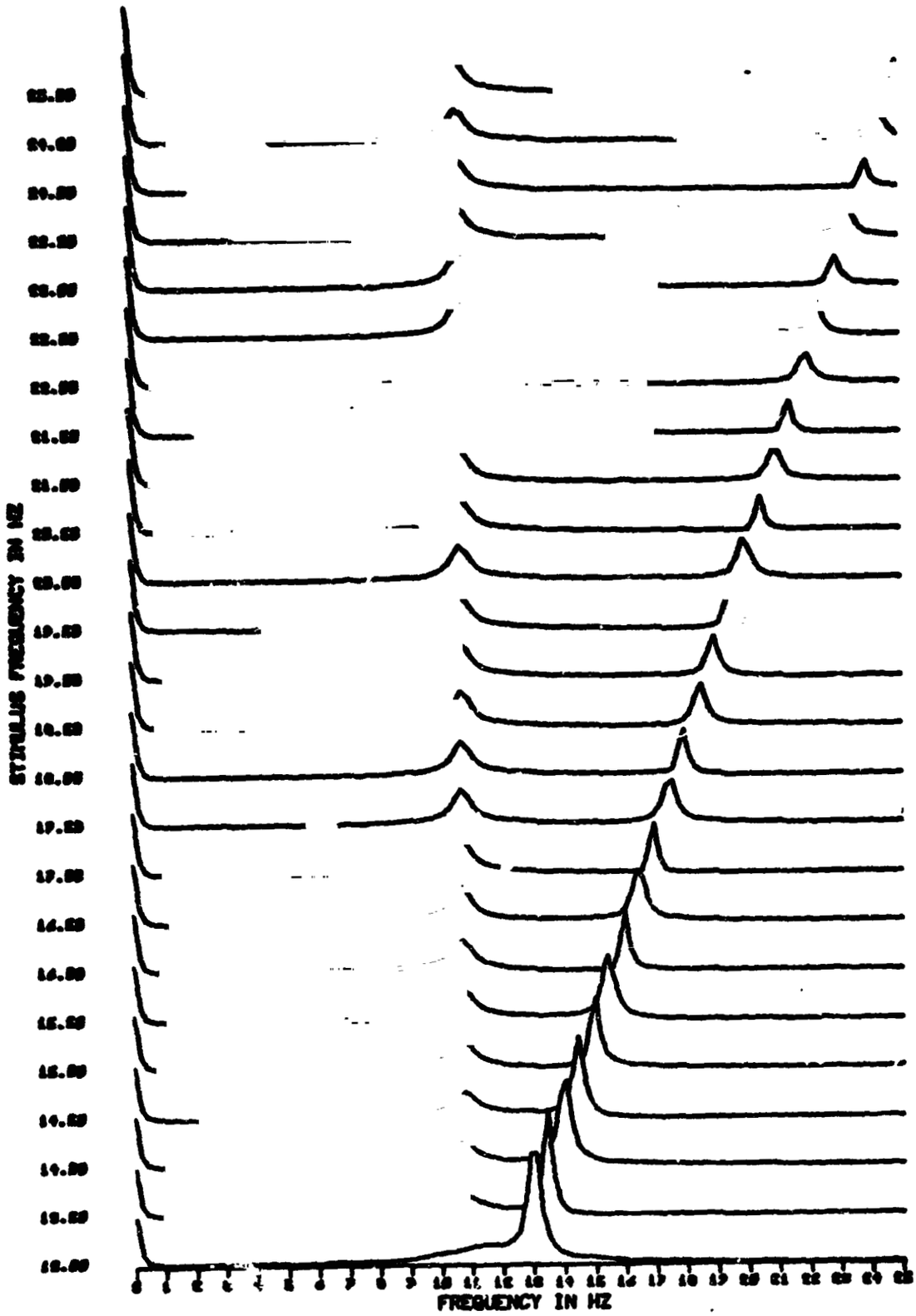


Figure 18 Simulated EEG spectra for flash frequencies from 13 Hz to 25 Hz

entrainment, combined frequency oscillations, and stimulus harmonics. These effects can again be seen in Figures 19 and 20 which are spectra from 5.12 seconds of sine wave driven simulations. These spectra will be compared with those obtained from experimental data in a section below; the next section discusses data collection and processing.

## 3. Data Collection and Processing

The data collected to test the model have been obtained from a very simple experimental paradigm. Subjects are presented a series of stroboscope flashes or sinusoidally modulated intensities through closed eyelids; the stimulus is delivered for 20 seconds at some fixed frequency, followed by a 10-second rest period. This sequence is repeated for each desired frequency, typically .5 Hz through 25 Hz in .5 Hz steps. The frequency pattern can be selected arbitrarily. The EEG signals are obtained from left and right occipital electrodes referenced to yoked earlobes; the ground electrode is on the mastoid. The Grass preamp bandpasses the signal between 1 Hz and 300 Hz, and the A/D analog prefilter is a 6-pole Bessel with a 100 Hz lowpass cutoff frequency. Digitizing is at 1000 Hz, and subsequent filtering is done by a transversal filter to avoid further phase distortion. Power spectra are computed by Fast Fourier Transform on 5.12 seconds of the data, forming the power spectrum and then averaging three such spectra 4.0 seconds after the start of the stimulus. This procedure substantially reduces the noise, which is further reduced for viewing aesthetics by the non-causal recursive filter

$$H(z) = \frac{z^2 + 2z + 1}{4z} \quad .$$

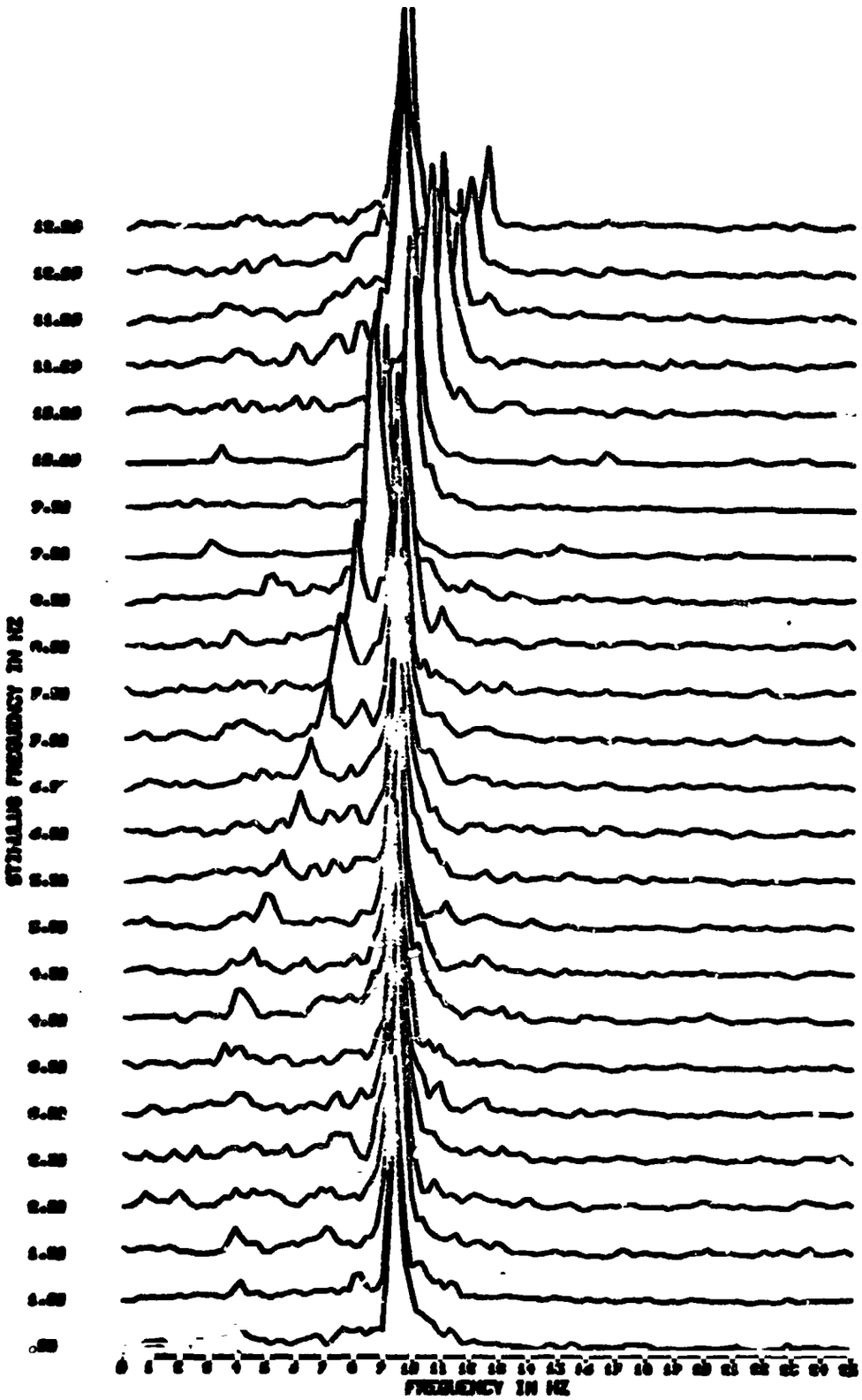


Figure 19 Simulated EEG spectra for sine frequencies from .5 Hz to 12.5 Hz

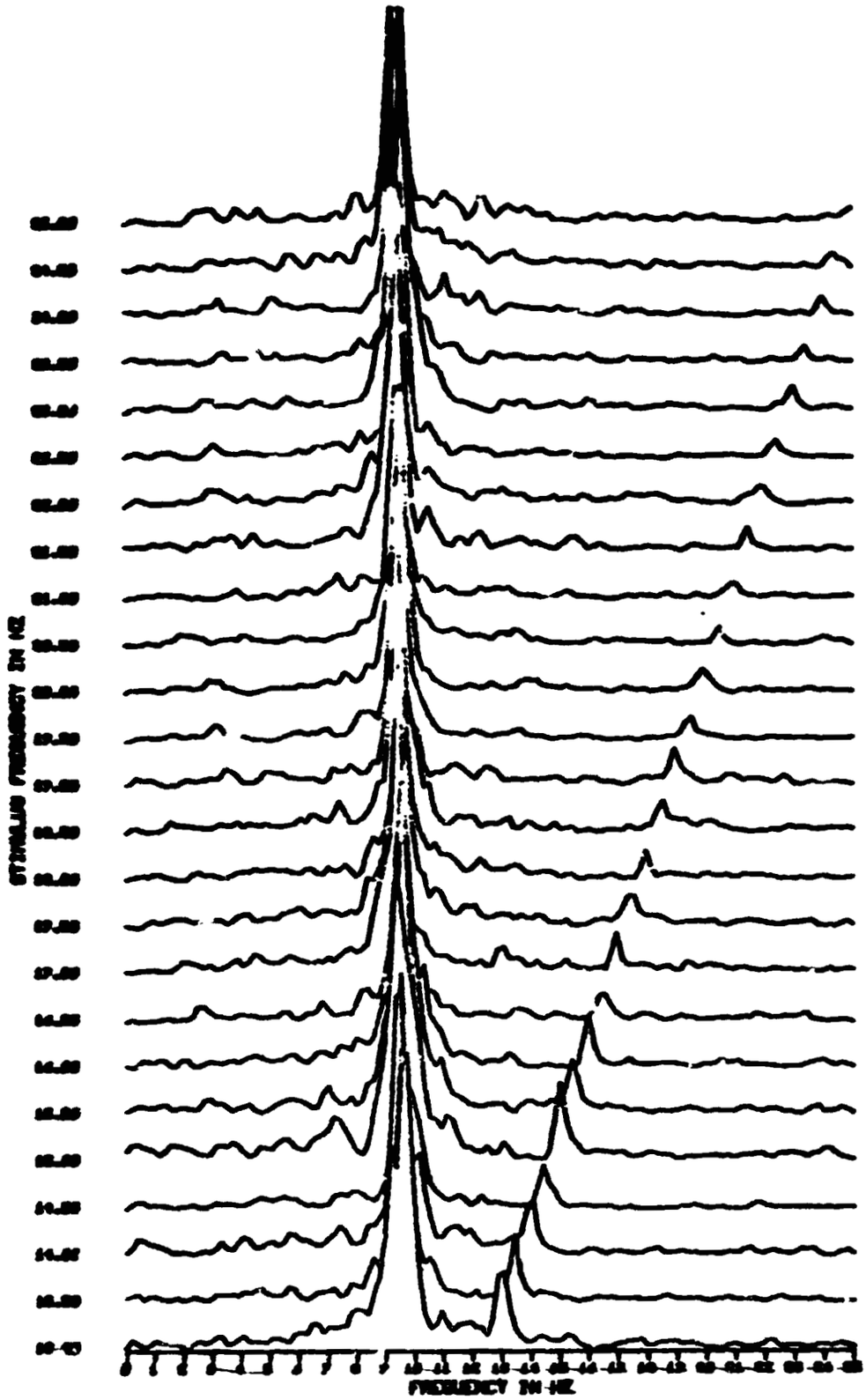


Figure 29 Simulated EEG spectra for sine frequencies from 13 Hz to 25 Hz

The resulting spectra may be superimposed with hidden lines removed by classical graphics techniques; a small amount of information must be saved after each spectrum is plotted.

The stroboscopic stimuli are produced by a Grass PS-2 strobe lamp in a sound-proof enclosure. It is driven by a relay contact. The sinusoidally modulated intensity stimuli are produced by a pair of hemispherical goggles, each containing ten LEDs, driven by a current source controlled by a D/A converter on the PDP-15. The voltage supplied is proportional to $\exp(\sin \omega_1 t)$ since the LED amplitude is linear with current and sinusoidal intensity is desired. Both stimuli are delivered through closed eyelids to ensure a uniform visual field.

## 4. Comparison of Model Simulations and Experimental Data

The comparison of model simulated results with experimental results is subject to difficulties arising from the noise in the data and the random nature of much of the EEG signal. The alpha frequency is not fixed and is in fact nonstationary; it is influenced by the subject's level of alertness and other uncontrollable factors. The response of the EEG to a stimulus is only measurable in the average, since individual responses are masked or corrupted by noise. Averaging can also mask certain characteristics of the response, depending upon the scheme used.

The best comparison of model-produced results and data for entrainment phenomena is a comparison of their power spectra. This allows the data spectrum to be relatively free of noise by averaging successive spectra from the same stimulus epoch. Examples of stroboscopically stimulated

data spectra may be seen in Figures 21 through 24. Note the excellent match overall with the simulated spectra discussed previously. The last subject has virtually no alpha rhythm, but exhibits all of the entrainment phenomena predicted, so the model accounts surprisingly well for extreme cases. Figures 25 and 26 show spectra for a sinusoidally stimulated subject. Note the reduction in harmonic amplitude as predicted by the simulation. Some detailed comparisons of each type of phenomena follow. Figure 27 shows the unstimulated case with the model parameters adjusted to match the subject (records were selected from Figures 21 and 22). Figure 28 illustrates harmonic entrainment, with subharmonic and superharmonic entrainment treated in Figures 29 and 30. Figure 31 is an example of combined frequency oscillation. The model simulations agree well with the data. Additional comparisons may be found in previous reports.

Further comparisons are in progress, especially the comparison of phase and amplitude changes induced by the stimuli. Preliminary results indicate that the model predictions are reasonable first order approximations to the data, but that revisions in the model will likely be necessary to fully account for the observed phenomena. The excellence of match in the frequency domain bears out the goodness of the phase shift predictions for small phase shifts, but it appears that larger shifts are occurring than predicted for certain cases.

In sum, a nonlinear model for the behavior of the EEG during visual stimulation has been analyzed and compared with actual EEG data. The model accounts for several phenomena well in a unified fashion, and suggests other phenomena of interest. The model specifies a trigonometric

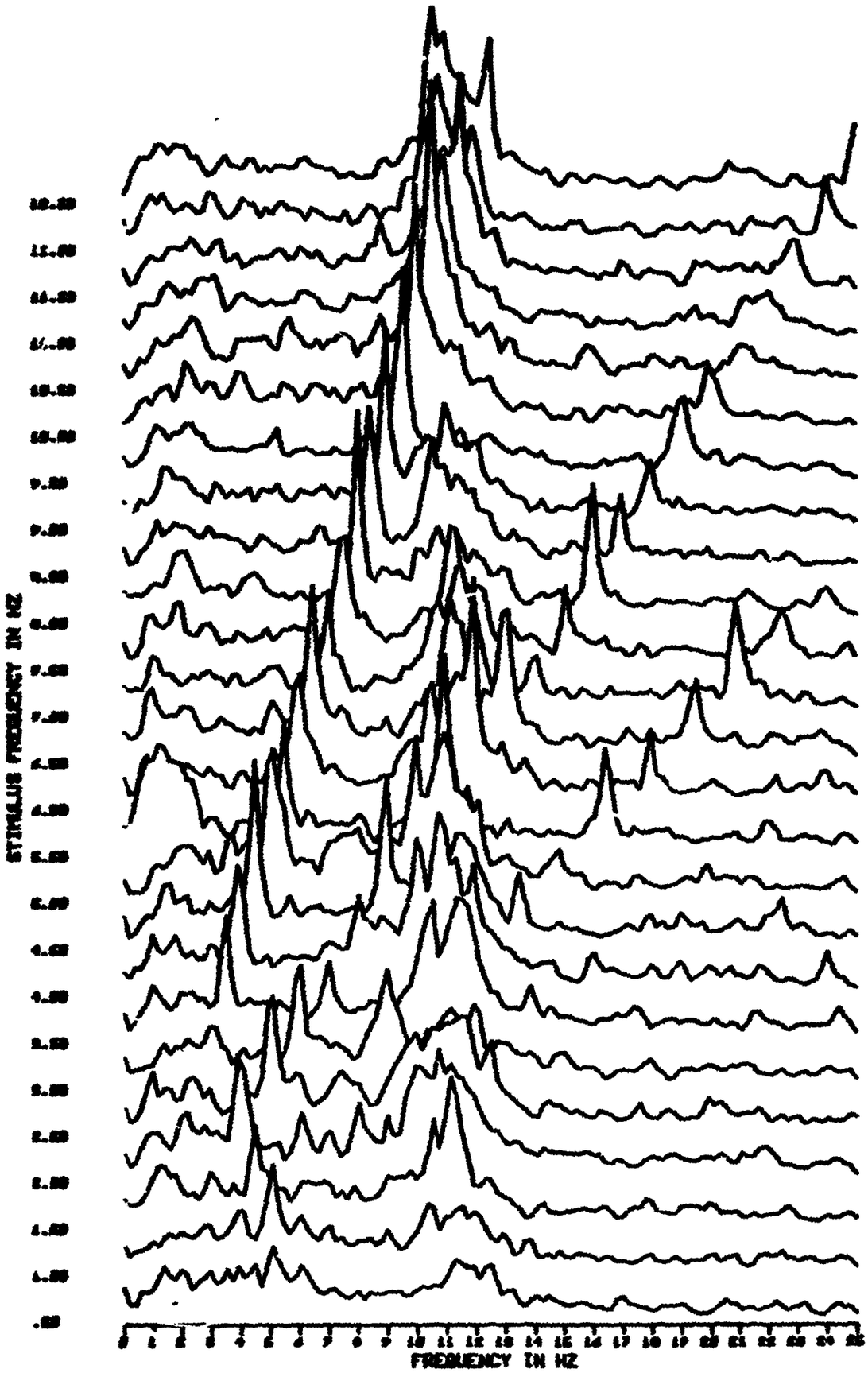


Figure 21 EEG spectra from subject L. M. for flash frequencies .5 Hz to 12.5 Hz

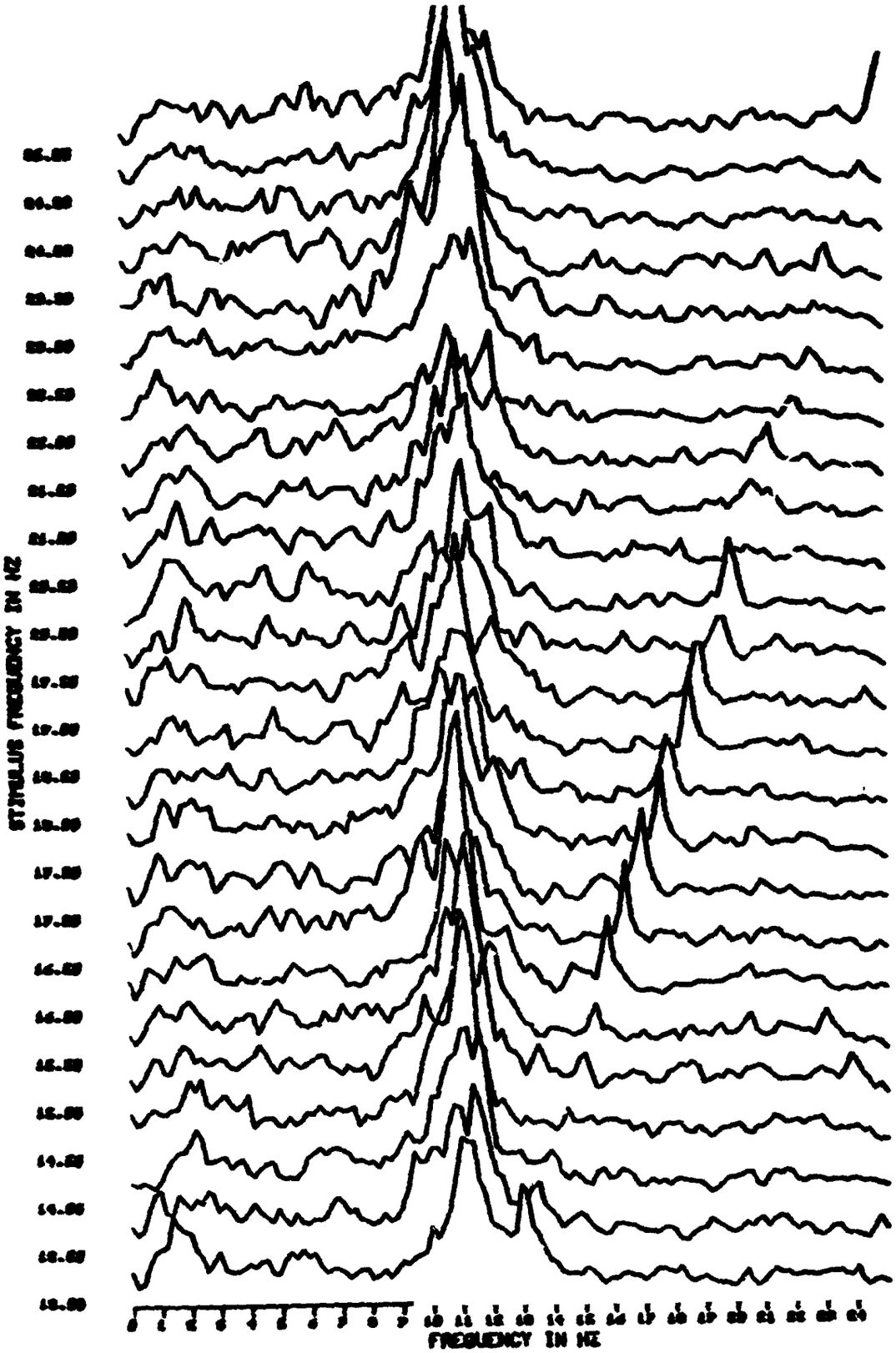


Figure 22 EEG spectra from subject L. M. for flash frequencies 13 Hz to 25 Hz

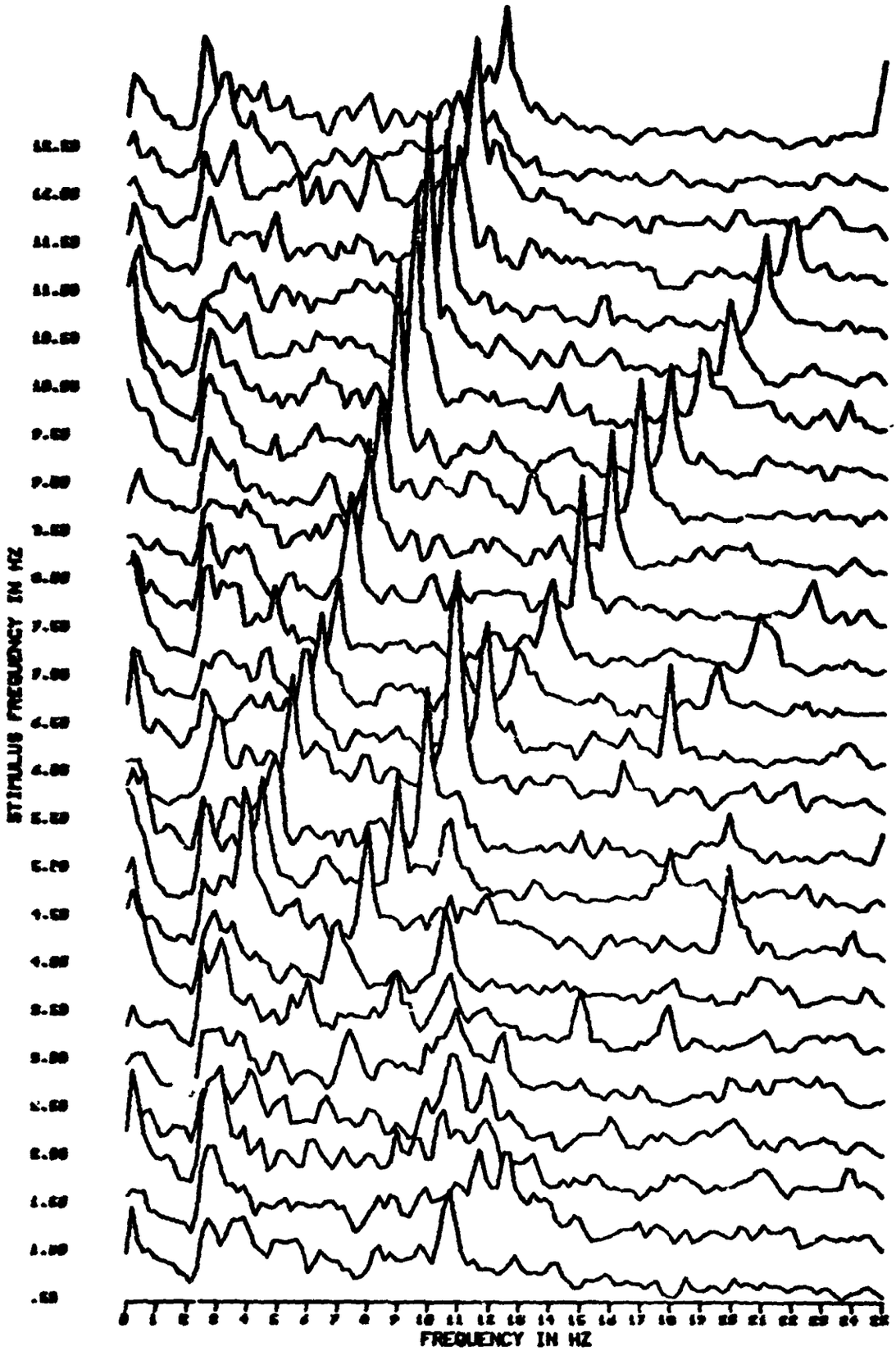


Figure 23 EEG spectra from subject F. M. for flash frequencies .5 Hz to 12.5 Hz

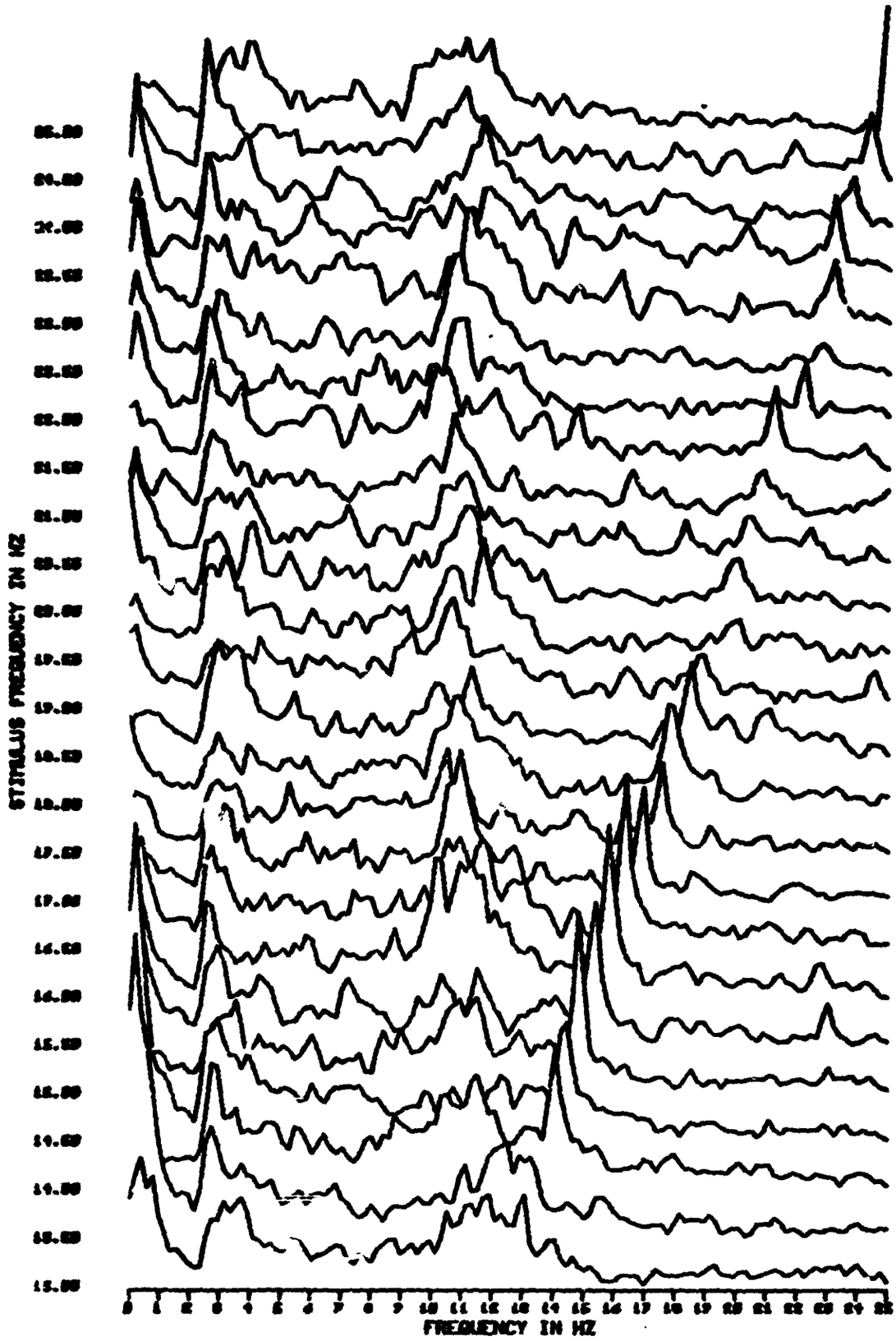


Figure 24 EEG spectra from subject F. M. for flash frequencies 13 Hz to 25 Hz

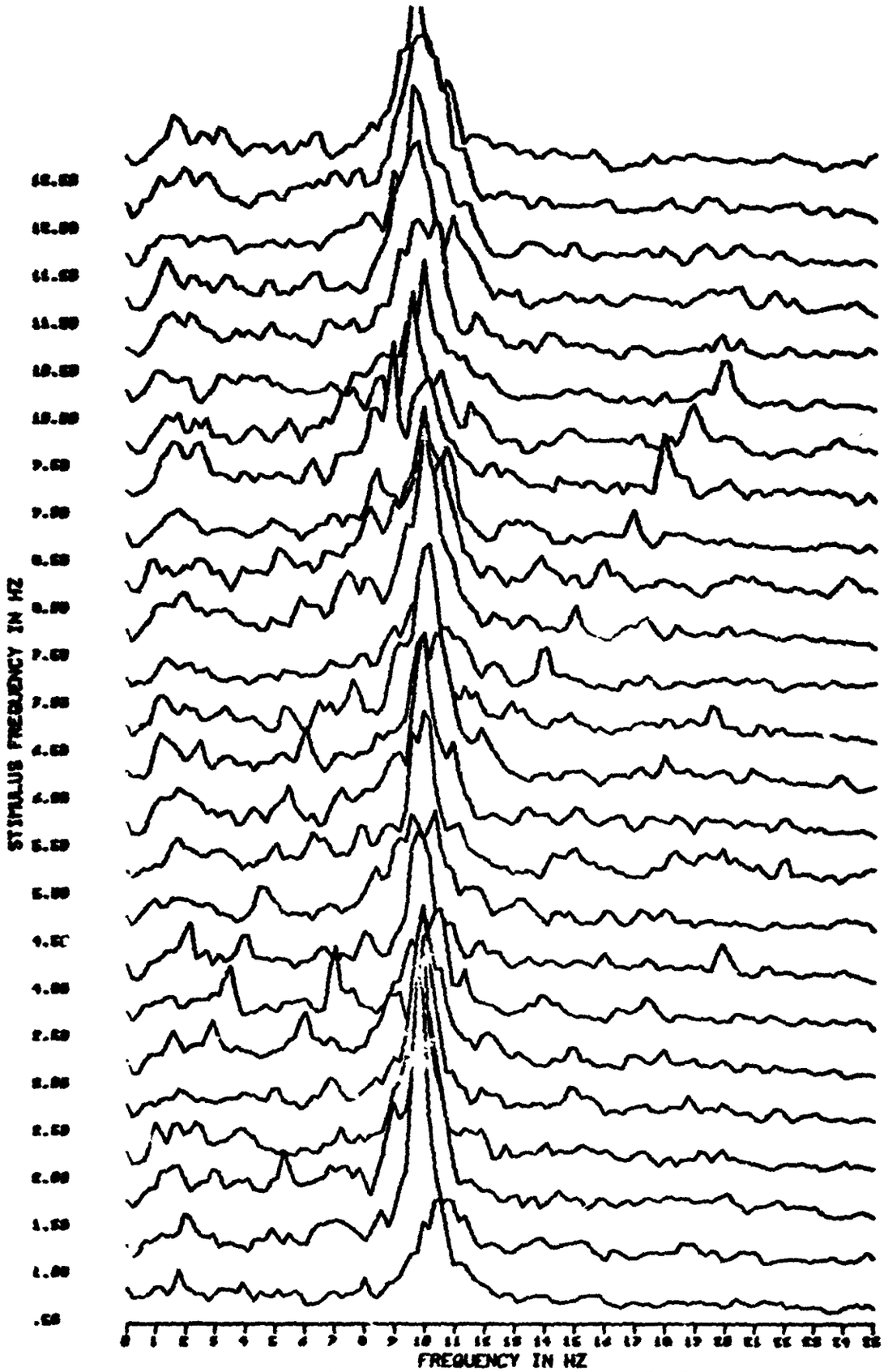


Figure 25 EEG spectra from subject R. S. for sine frequencies .5 Hz to 12.5 Hz

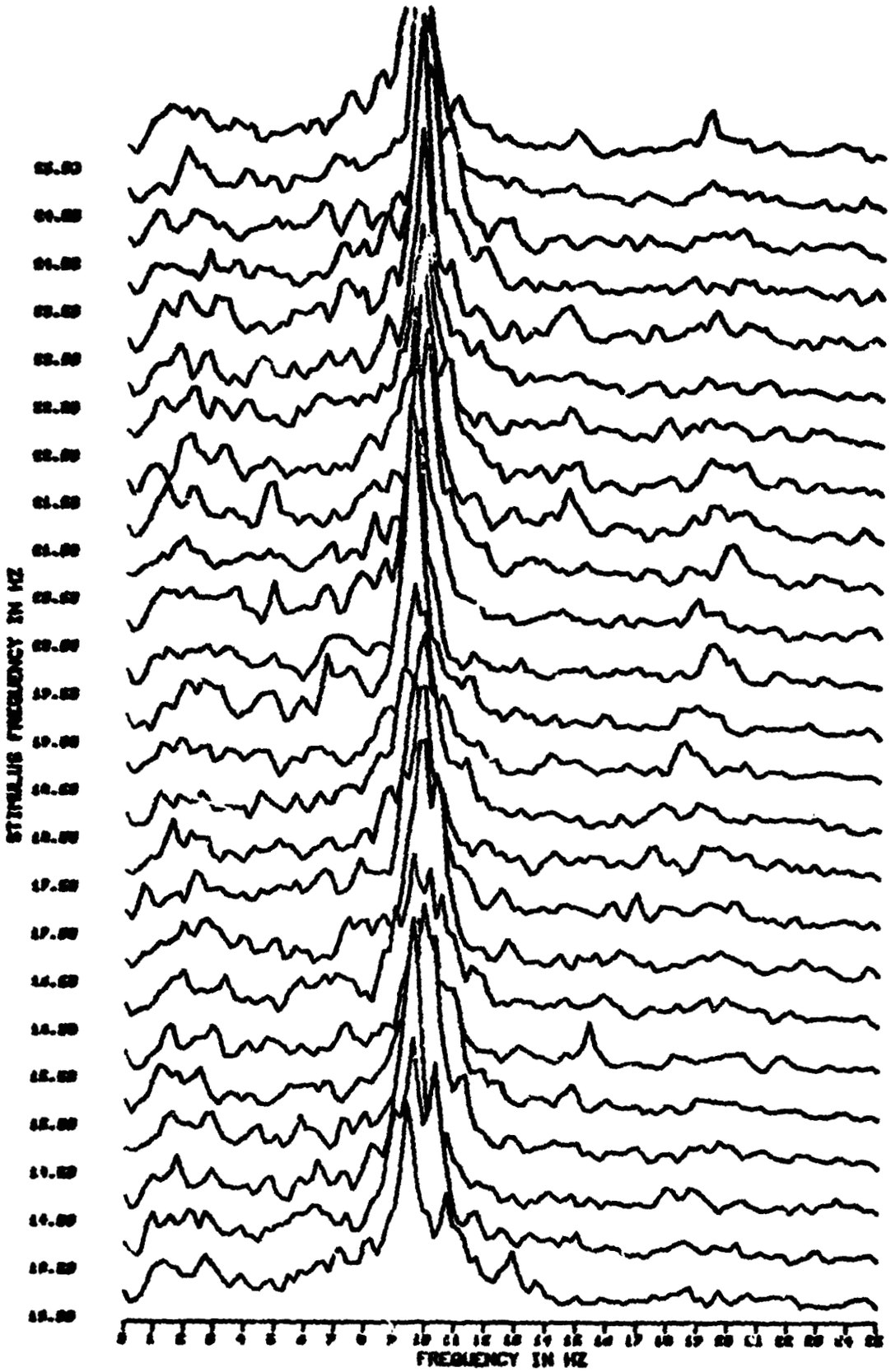


Figure 26 EEG spectra from subject R. S. for sine frequencies 13 Hz to 25 Hz

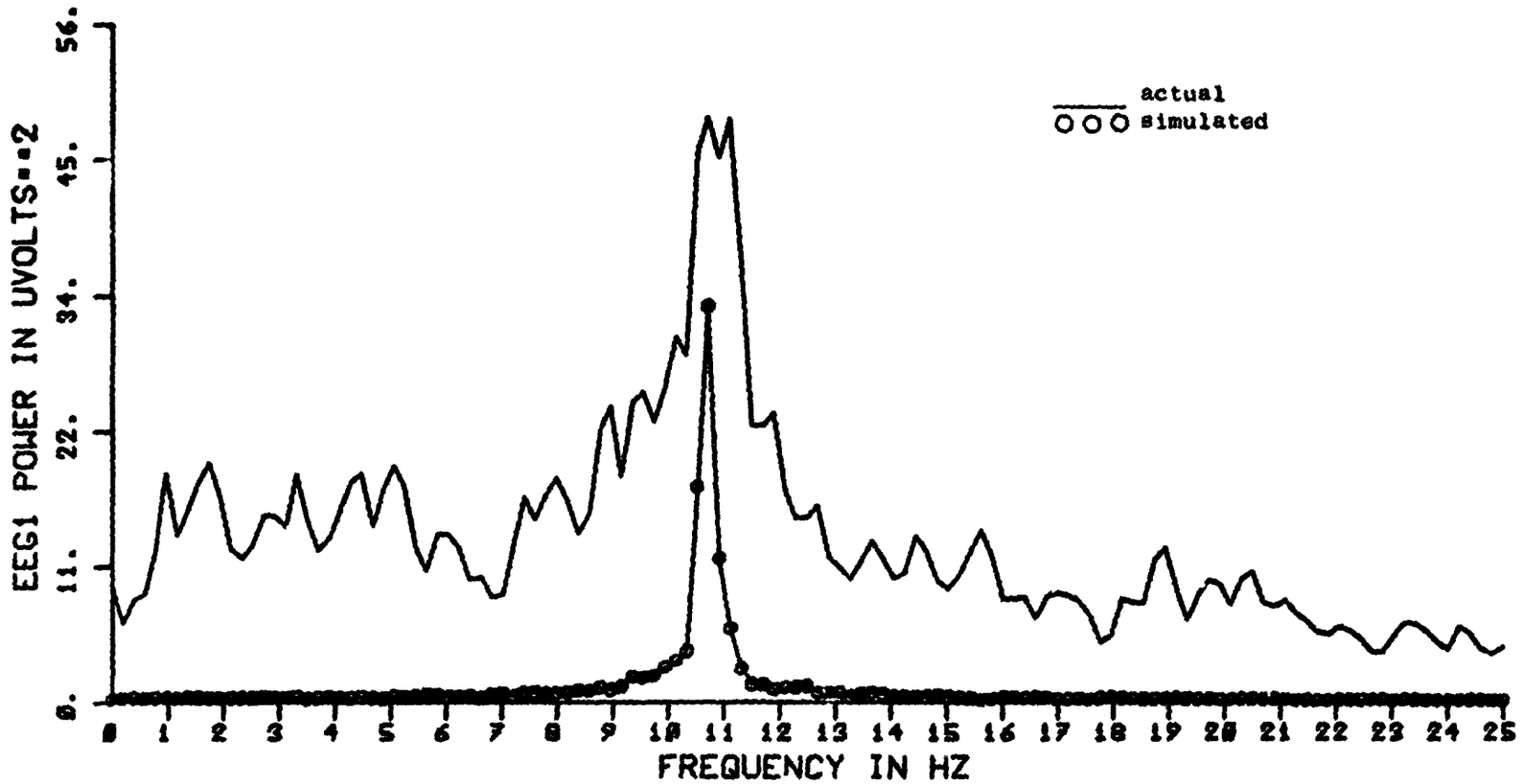


Figure 27 Actual and simulated EEG spectra in the absence of stimulation

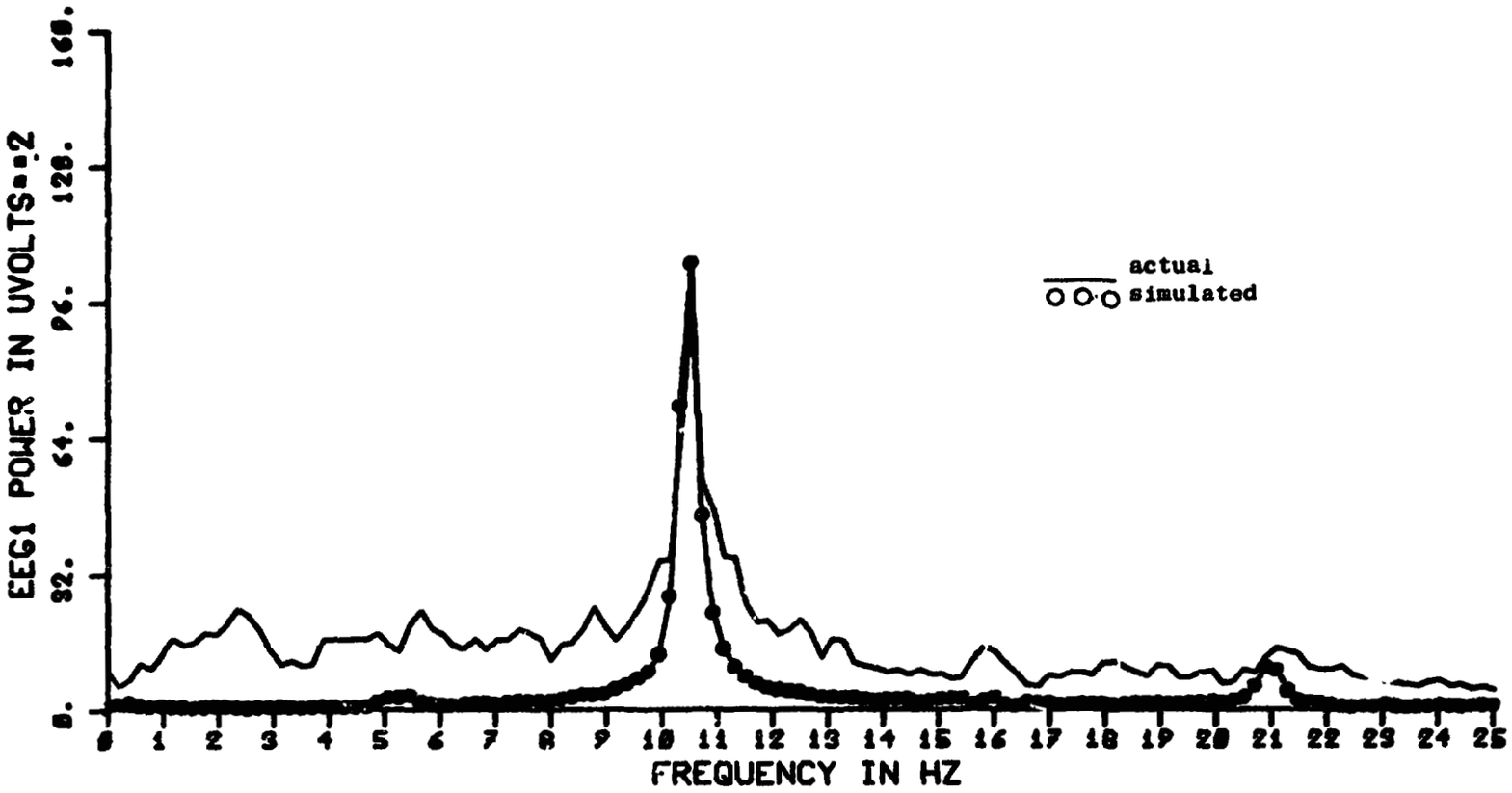


Figure 28 Actual and simulated EEG spectra during flash stimulation of 10.5 Hz

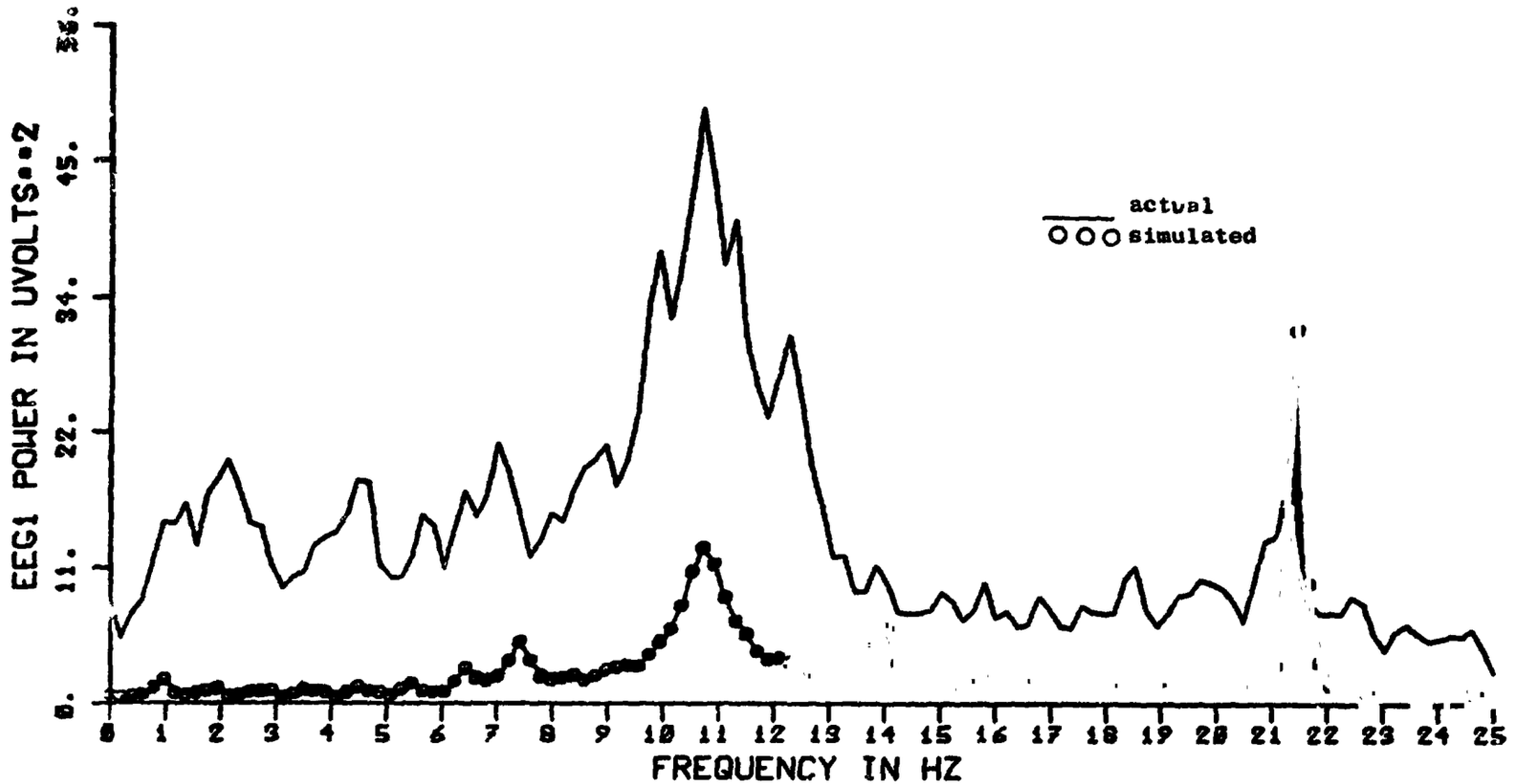


Figure 29 Actual and simulated EEG spectra during flash stimulation of 21.5 Hz

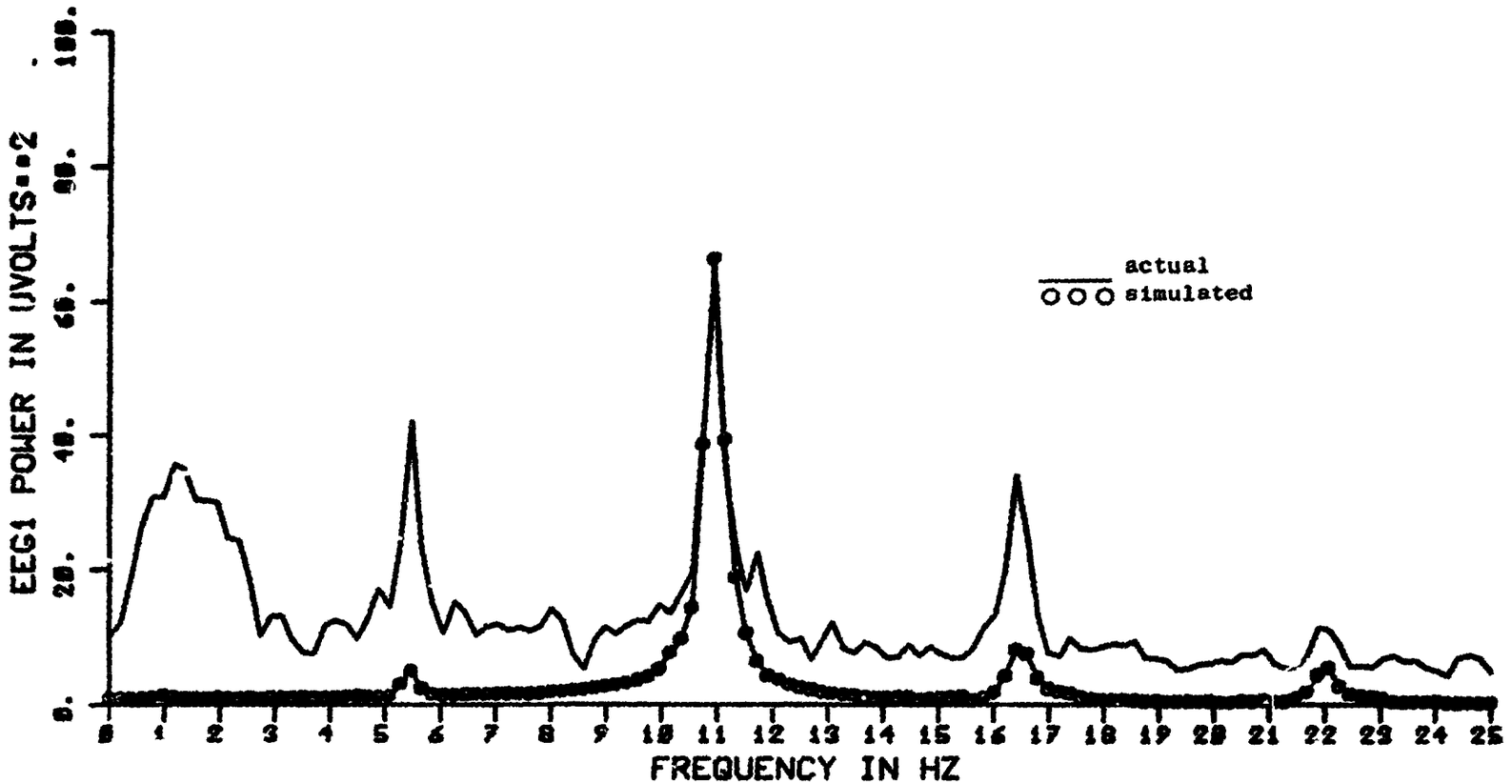


Figure 30 Actual and simulated EEG spectra during flash stimulation of 5.5 Hz

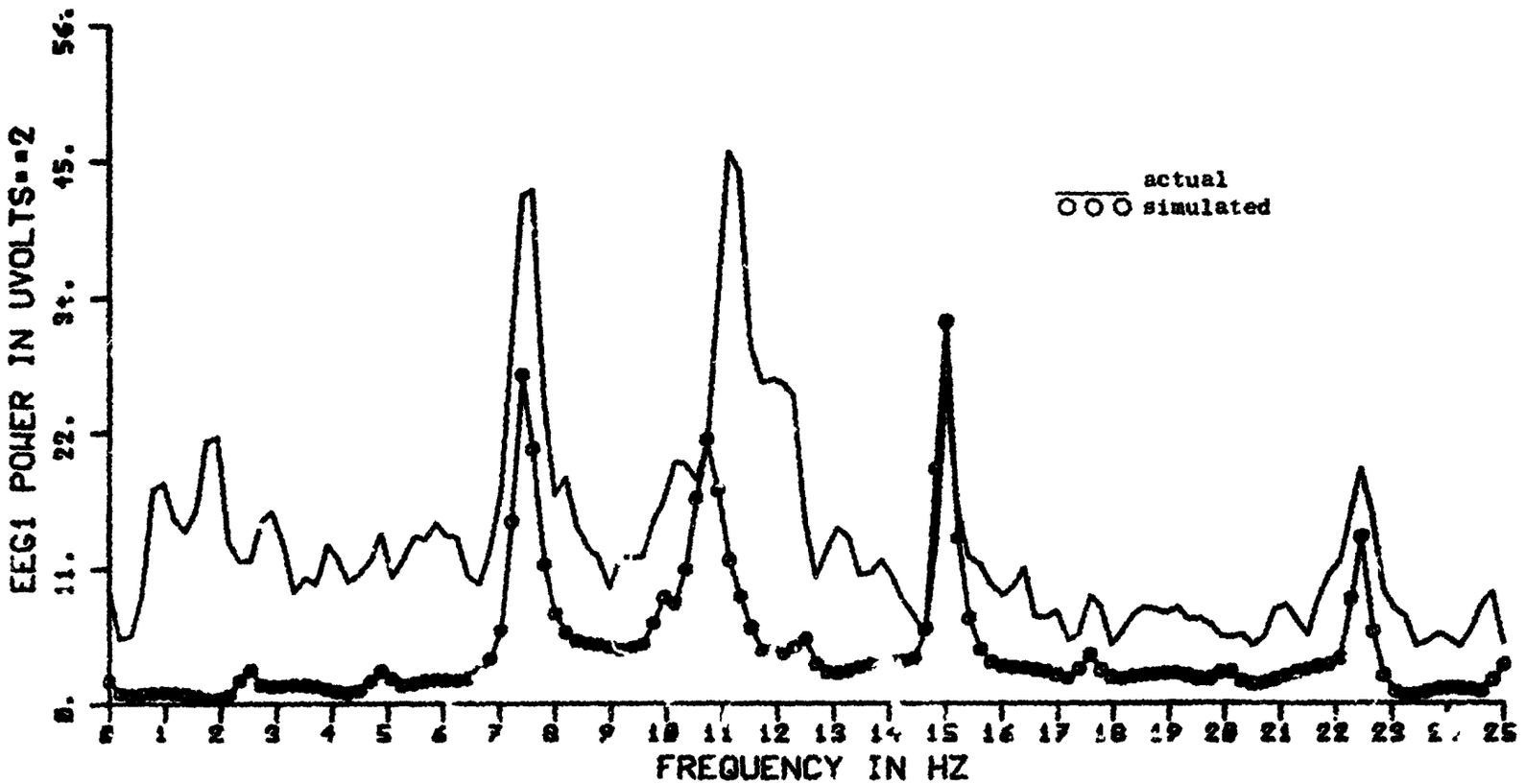


Figure 31 Actual and simulated EEG spectra during flash stimulation of 7. Hz

form for the excitability of the EEG as a function of phase, which explains well the various entrainment phenomena seen in EEG data. Detailed phase analyses are in progress which indicate that the model prediction is good to a first degree, but needs some revision. One possibility at this point is the existence of an excitability function at half the alpha frequency. The phase-dependency of the model response has considerable bearing on the phase-dependency of saccade onset.

## 5. Prediction of EEG Alpha Waveforms

In order to present the visual stimuli to coincide with the most favorable brain state and to predict the onset of saccadic eye movement, it is necessary to have the capability to predict the EEG alpha waveforms, in particular, their phasic features. In conjunction with the EEG model, we have developed and implemented an EEG-waveform predictive scheme by using autoregressive processes. The development and implementation of this scheme will be described in detail. Our discussion will be centered around the modeling of EEG data by an autoregressive process and its use for forecasting.

The fitting of time-series models to EEG signals has been treated in the literature. They have been specifically applied to EEG analysis in the following areas: use for EEG spectral analysis; use of the mixed model to define certain parameters for describing the stationary parts of the EEG signal; and use of the one-step ahead prediction error to compare two different models. Our interest lies in the prediction of the alpha activity in the EEG for a longer lead time.

Although autoregressive processes have been used for prediction

of time series in general, they have not been used for prediction of EEG data. In those general cases, the signal or time series is assumed to be stationary. EEG signals are, in general, nonstationary. For expedience, they may be considered piecewise-stationary; i.e., stationary over short intervals of time. Hence, in our application, we are restricted to limited sample lengths. This restriction creates certain problems which we shall discuss later.

To model a discrete time series $X_i$ , $i = 1, 2, \ldots$, by an autoregressive process of order $p$ , we may write

$$X_t = a_1 X_{t-1} + a_2 X_{t-2} + \ldots + a_p X_{t-p} + \epsilon_t$$

where $a_1, a_2, \ldots, a_p$ are the parameters of the process to be estimated and $\epsilon_t$ is a zero-mean white Gaussian noise. It is generally assumed that the process $X_t$ has zero mean; otherwise, the mean is subtracted from the entire series. In general, the autocorrelation function of an autoregressive process consists of two components; viz., decaying exponential and damped sinusoidal waveforms. It has been recognized that the real roots of the characteristic equation of the autoregressive process, i.e.,

$$1 - a_1 B - a_2 B^2 - \ldots - a_p B^p = 0 \quad ,$$

give rise to the decaying expoentials and its complex-conjugate-root pairs are responsible for the damped sinusoids in the autocorrelation function. We show in Figure 32 the autocorrelation function of an EEG sample filtere in the alpha range. It is seen that the EEG autocorrelation function may be well approximated by a sum of decaying exponentials and damped sinusoids. In Figure 32 , we superimpose the autocorrelation

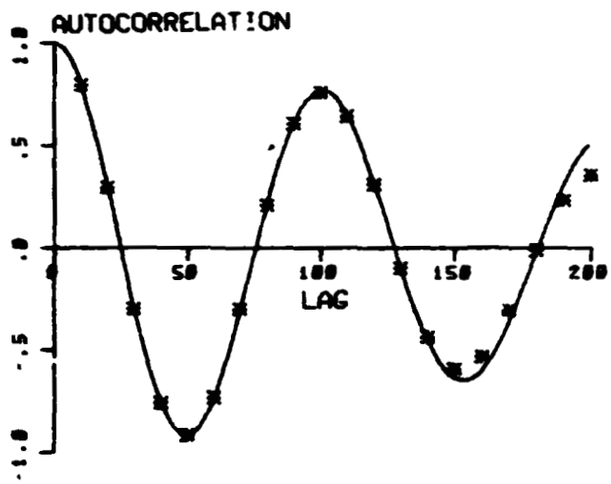


Figure 32 Autocorrelograms: solid curve from a typical EEG alpha waveform and dots from an autoregressive process fitted to the data

function of an autoregressive process fitted to EEG data to show our assertion. This leads naturally to the temptation of modeling EEG signals by autoregressive processes. Since autocorrelation function is not a unique process, there are other processes which will give rise to the same autocorrelation function. We chose an autoregressive process based on its simplicity in implementation.

To accomplish our aim in prediction, we have broken down the problem into two parts:

(1) Estimation of the autoregressive parameters;

(2) Generation of "good" forecasts according to some criteria using the above estimation.

Since the EEG process is considered piecewise stationary, the parameter estimates have to be updated continuously. Thus, a scheme is needed for updating the parameter estimates as new data arrive. For estimation of the parameters, we have used the least-squares principle. These estimated parameters are then used to generate the minimum mean-square error forecasts for a specified lead time. We developed a new modified scheme for this purpose.

To furnish the basis for our modified scheme, we shall describe a scheme ordinarily used. The development and implementation of a modified scheme to suit our needs will then be presented. Results have been obtained by applying our scheme to real EEG data. We will present these results to show the utility of our prediction method.

We will concentrate our discussion to a parameter estimation method. Later we will present our modifications to this method in order to improve the performance for our purpose. Let us consider

the $p^{th}$-order process

$$X_t = a_1 X_{t-1} + a_2 X_{t-2} + \dots + a_p X_{t-p} + e_t$$

where $e_t$ is white Gaussian noise. The order of the autoregressive process is estimated by successively fitting models with higher order to the data and determining when the last parameter $a_p$ becomes small enough.

The least-square estimates of the parameters can be shown to satisfy the following set of linear equations

$$\begin{cases} a_1 Q_{22} + a_2 Q_{23} + \dots + a_p Q_{2,p+1} = -Q_{12} \\ a_1 Q_{23} + a_2 Q_{33} + \dots + a_p Q_{3,p+1} = -Q_{13} \\ a_1 Q_{2,p+1} + a_2 Q_{3,p+1} + \dots + q_p Q_{p+1,p+1} = -Q_{1,p+1} \end{cases}$$

where the $Q_{ij}$'s are given by

$$Q_{11} = \sum_{i=1}^{n} X_1^2$$

$$Q_{1j} = -\left(X_1 X_j + X_2 X_{j+1} + \dots + X_{n-j+1} X_n\right)$$

and

$$Q_{ij} = X_i X_j + X_{i+1} X_{j+1} + \dots + X_{n-j+1} X_{n-i+1} ,$$

$$i \neq 1 , \; j \neq 1$$

Knowing $Q_{ij}$'s , we solve the set of equations to obtain the least-square estimates of the parameters $a_1, a_2, \dots, a_p$ . The least-square estimate of the noise variance is given by

$$\hat{\sigma}_e^2 = \frac{1}{n} \left( Q_{11} + \left| Q_{12}, Q_{13}, \dots, Q_{1,p+1} \right| \left| a_1, a_2, \dots, a_p \right|' \right) .$$

Previous discussions furnish us a numerical procedure for estimation of the parameters $a_1, a_2, \dots, a_p$ and $\sigma_e$ in the least-square sense from the data $(X_1, X_2, \dots, X_n)$ . Based on this procedure, one can model

a weakly stationary process by a $p^{th}$-order autoregressive process. Since EEG data exhibit nonstationarity, this method has to be modified for our problem. Besides, our interest is in the use of the parameter for prediction rather than modeling.

Having obtained the estimates of the parameters, we turn our attention to the problem of prediction. We need a scheme whereby the prediction can be made for a certain lead time and then when a new data point becomes available, the forecast can be updated without repeating the original process all over again.

We will consider here minimum mean-square forecasts only. Denote the estimation of $X_{t+\ell}$ obtained at time $t$ by $X_{t+\ell|t}$. At time $t$, the values of the samples up to time $t$ are known. The minimum mean-square error forecast is given by (using the projection theorem):

$$X_{t+\ell|t} = a_1 X_{t+\ell|t} + a_2 X_{t+\ell-2|t} + \dots + a_p X_{t+\ell-p|t} ,$$

which provides the forecasts in the form of a difference equation. Given the sample values $X_t$, $X_{t-1}$, ..., $X_{t-p+1}$, we can progressively calculate $X_{t+1|t}$, $X_{t+2|t}$, ... by using the above equation. Using this procedure, we can generate forecasts for any lead time utilizing the parameters estimated earlier. However, the forecasts at each point have to be updated as soon as the sample $X_{t+1}$ becomes available. It is rather cumbersome to do in the above form. Hence, a different approach is required.

Instead of writing the original equation as

$$X_t = a_1 X_{t-1} + a_2 X_{t-2} + \dots + a_p X_{t-p} + e_t ,$$

we will express $X_t$ in a weighted infinite sum of $e_t$, $e_{t-1}$, ... as

$$X_t = \sum_{j=0}^{\infty} b_j e_{t-j} ,$$

where the $b_j$'s can be expressed as

$$b_0 = 1$$

$$b_1 = a_1 b_0$$

$$b_2 = a_1 b_1 + a_2 b_0$$

$$\vdots$$

$$b_j = a_1 b_{j-1} + a_2 b_{j-2} + \dots + a_p b_{j-p} , \quad j \geq p .$$

The minimum-mean-square-error forecast is

$$X_{t+\ell|t} = \sum_{j=\ell}^{\infty} b_j e_{t+\ell-j} \quad . \tag{4}$$

This form lends itself easily to updating. This can be demonstrated by $X_{t+\ell|t+1}$ after $X_{t+1}$ arrives. We may write

$$X_{t+\ell|t+1} = \sum_{j=\ell-1}^{\infty} b_j e_{t+\ell-j}$$

and hence

$$X_{t+\ell|t+1} - X_{t+\ell|t} = b_{\ell-1} e_{t+1} \quad . \tag{5}$$

Thus, at time $t + 1$ , the forecasts for lead lengths up to $\ell - 1$ can be easily obtained from the predicted values at time $t$ for lead lengths up to $\ell$ by using Eq. (5) and by recognizing

$$e_{t+1} = X_{t+1} - X_{t+1|t} .$$

This provides a convenient scheme for updating forecasts as more data become available.

The variance of the forecast error may be easily obtained from Eq. (4). Since the $\ell$-step ahead forecast error at time $t$ is given by

$$e_{t+\ell|t} = X_{t+\ell} - X_{t+\ell|t} = \sum_{j=0}^{\ell-1} b_j e_{t+\ell-j} \quad .$$

The variance $V(\ell)$ may then be expressed as

$$V(\ell) = \sum_{j=0}^{\ell-1} b_j^2 \sigma_e^2 \tag{6}$$

This variance gives us a measure of the goodness of fit for the model. Since we have assumed the e's to be normal, the conditional probability density function $P(X_{t+\ell}|X_t, X_{t-1} \ldots)$ is normal with mean $X_{t+\ell|t}$ and variance $V(\ell)$. Based on this information, we can obtain confidence intervals for the forecasts. For example, 95% of the normal distribution mass lies within $\pm$ 1.96 $\sigma$ of the mean where $\sigma$ is the standard deviation. Hence, $X_{t+\ell|t} \pm 1.96\sqrt{V}$ is the 95% confidence interval for the forecast, i.e., the probability that the actual value will lie in that range is .95.

The previous formulation gives the forecasting procedure to predict values $\ell$ samples ahead from any time $t$. In order to increase the lead time for forecasting, one has to increase the value of $\ell$. It is, however, evident from Eq. (6) that the error variance becomes larger as $\ell$ increases and the confidence interval for a given level of confidence will also increase accordingly. Another way to increase the lead time would be to increase the sampling interval and thus keep the value of $\ell$ as low as possible so that the level of performance of the predictor may be maintained. However, the sampling rate or sampling interval for a signal is determined by the bandwidth of the signal. If the signal is furnished in digital form, then one has little choice in altering the sampling interval. One could, of course,

increase this interval by dropping every $k^{th}$ block of data points. In any event, the increase in sampling interval means reduction in the number of data points in a given interval of time. This reduction in data points leads to a higher variance for the estimates. Besides, the number of data points may be so much reduced, since the EEG signal is considered stationary only for a short period of time, that the estimates are not statistically significant. For these reasons, we reformulate the autoregressive model in a more general form as

$$X_t = a_1 X_{t-k} + a_2 X_{t-2k} + \dots + a_p X_{t-pk} + e_t$$

which, when $k = 1$, reduces to the case discussed earlier. This is equivalent to an autoregressive model for the time series

$$(X_t, X_{t-k}, X_{t-2k} \dots) .$$

The least-square estimates of the parameters can be obtained by a logical extension of the earlier results; viz.,

$$\begin{aligned} a_1 Q_{22} + a_2 Q_{23} + \dots + a_p Q_{2,p+1} &= -Q_{12} \\ a_1 Q_{23} + a_2 Q_{33} + \dots + a_p Q_{3,p+1} &= -Q_{13} \\ &\vdots \\ a_1 Q_{2,p+1} + a_2 Q_{3,p+1} + \dots + a_p Q_{p+1,p+1} &= -Q_{1,p+1} \end{aligned} \tag{7}$$

where the $Q_{ij}$'s are now redefined as

$$Q_{11} = \sum_{i=1}^{n} X_i^2$$

$$Q_{1j} = -\left(X_1 X_{(j-1)k+1} + \dots + X_{n-(j-1)k} X_n\right)$$

$$Q_{ij} = X_{(i-1)k+1} X_{(j-1)k+1} + \dots + X_{n-(j-1)k} X_{n-(i-1)k} ,$$

$$i \neq 1 \quad , \quad j \neq 1 .$$

The least-square estimates are the solutions of this new set of equations.

The forecast equations are modifield in a similar manner to give

$$X_{t+k\ell|t} = a_1 X_{t+k(\ell-1)|t} + a_2 X_{t+k(\ell-2)|t} + \cdots$$

$$+ a_p X_{t+k(\ell-p)|t}$$

and Eq. (4) becomes

$$X_{t+k\ell|t} = \sum_{j=\ell}^{\infty} b_j e_{t+k(\ell-j)}$$

with the $b_j$'s defined in terms of the $a_j$'s as before. In essence, the scheme processes the available data in such a regrouped fashion by resampling the data in $k$ multiples of the original sampling interval that the level of performance is not degraded. The performance of this scheme on EEG data will be discussed next. The usefulness of the scheme is demonstrated by our results.

We developed a computer program to implement an algorithm for recursive estimation of parameters and forecast of future values by using the new modified scheme. The program was written in FORTRAN for a PDP-15 computer. As an example for illustration, we applied our scheme to real EEG data, which were recorded while the subjects with closed eyes were stimulated by stroboscopic flashes for 50 seconds at the rate of 10 flashes per second, then no stimulation for 50 seconds, then another 50 seconds of stimulation, etc. The signals were sampled at an interval of 1.2 msec. Since we are mainly interested in the alpha component of the EEG, the data were filtered to obtain the components around the alpha range (7-13 Hz) through a transversal filter. The computer program reads this EEG data as its input. Other required information such as the number of sample points $N$ for which the process is considered stationary, the order of the process $P$, the resampling

value $K$, the prediction lead length $L$ and the window width NWND for updating the parameters are also read in as input. (For efficiency, the parameters are not updated with each new data point, but only after NWND new data points have been read in.) A flow chart of the program is shown in Figure 33. As soon as the above variables and the initial $N$ points are entered, the program computes the least-square estimates of the parameters by solving the set of linear equations (7). The error variance $\sigma_e^2$ is also estimated. These estimates are then used to generate minimum mean-square error forecasts up to $L$ steps ahead; i.e., forecast of $t + KL$ is obtained at time $t$. The variance of the forecast errors and the confidence interval for a certain significance level are also calculated. At this time, the next data point is read in; the residual is calculated as the difference between the actual value and the forecast; and the forecasts for the remaining points are updated by using Eq. (5). A new forecast for the value $L$ steps ahead is produced. This process is repeated until NWND new points have been exhausted. The procedure will repeat again starting with the recalculation of the parameter estimates.

Results of the prediction for various lead times are shown in Figures 34 through 38. In order to compare the predicted waveforms with the actual EEG, we plotted the predicted waveforms and then superimposed the actual EEG on top of them. The order of the autoregressive process was chosen as $p = 7$ by examining the partial autocorrelation function of EEG data for $k = 10$. The effective lead time in seconds is $k\ell T$ where $T$ is the sampling interval and $\ell$ denotes the lead time in number of samples. In Figures 34 through 38, the waveforms were

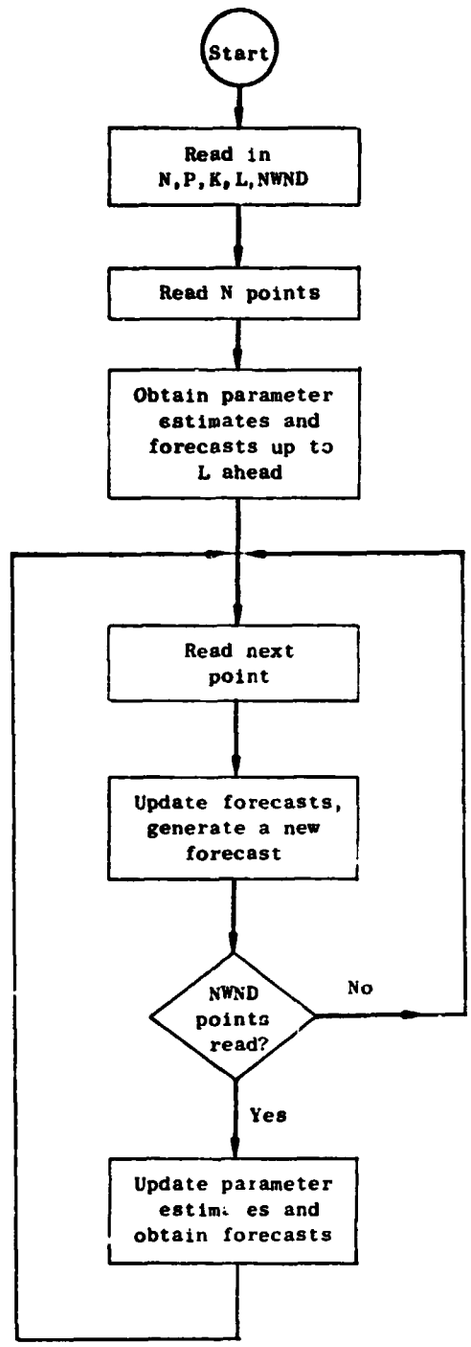


Figure 33 A flowchart for the realization of the prediction scheme

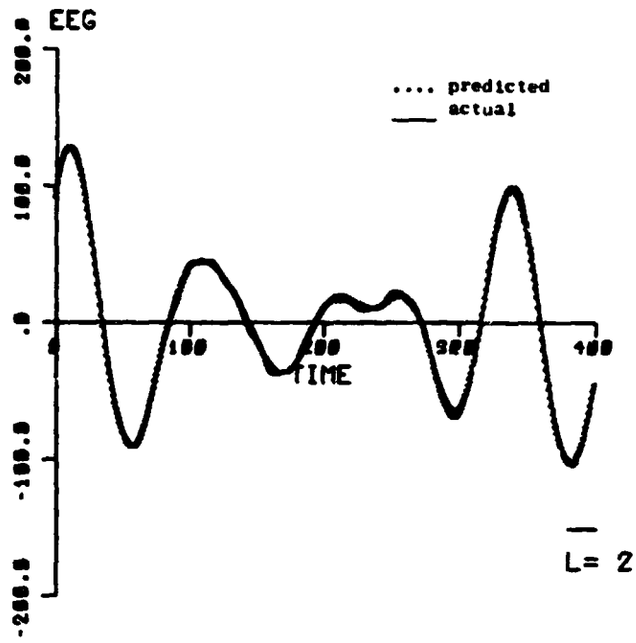


Figure 34 Actual and predicted waveform for lead time of 24 msec.

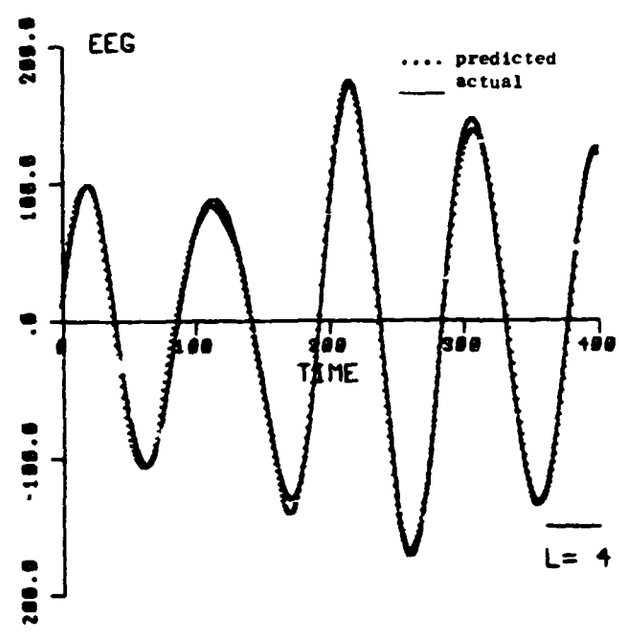


Figure 35 Actual and predicted waveform for lead time of 48 msec.

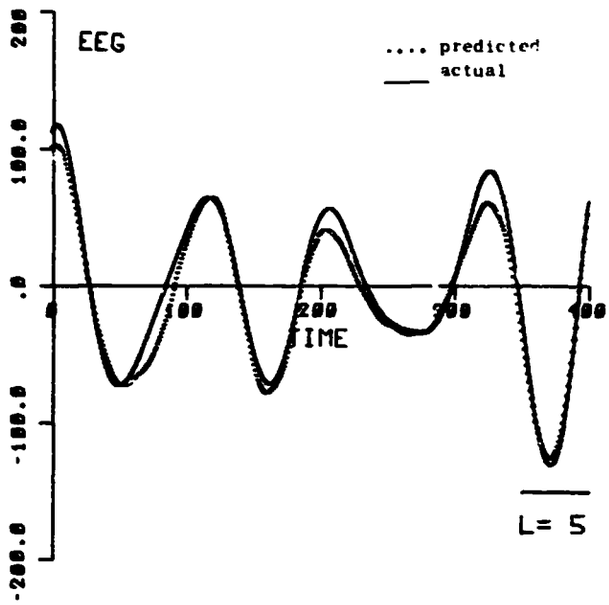


Figure 36 Actual and predicted waveform for lead time of 60 msec.

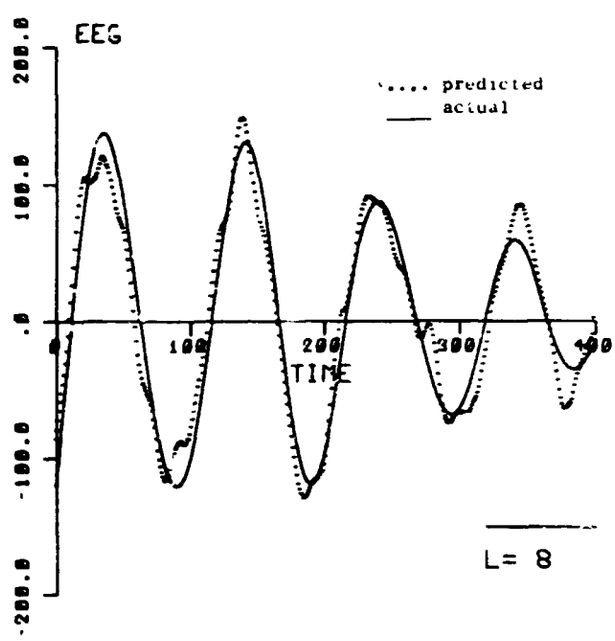


Figure 37 Actual and predicted waveform for lead time of 96 msec.

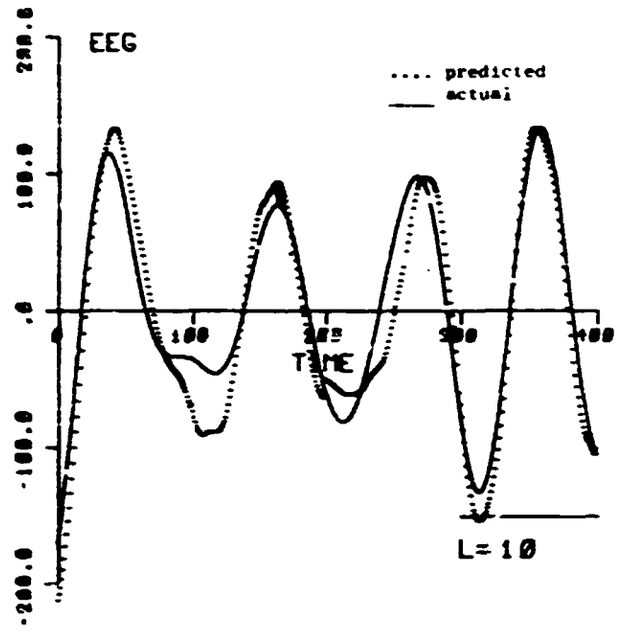


Figure 38 Actual and predicted waveform for lead time of 120 msec.

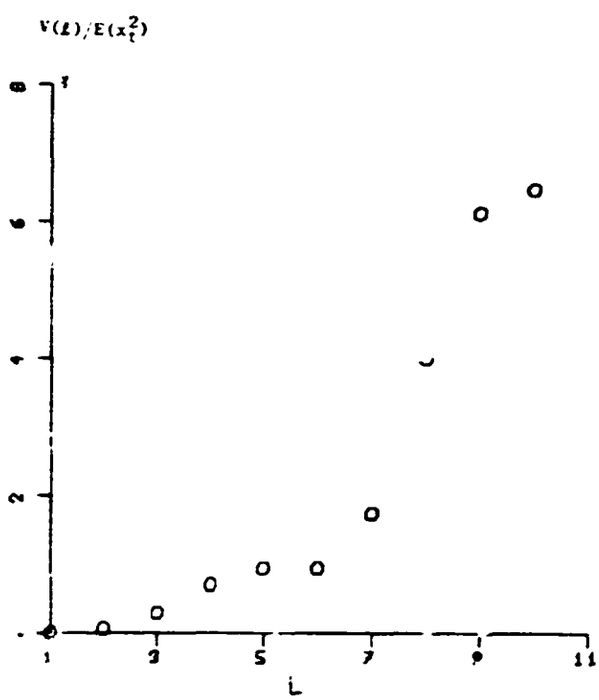


Figure [illegible] Prediction error variance vs. lead time

plotted against the sample numbers and the lead time $\ell$ was indicated at the lower right corner. For instance, in Figure 36, $\ell = 5$ means a lead time of $10 \times 5 \times 1.2 = 60$ msec., since $k = 10$ and $T = 1.2$ msec; hence, the length indicated for $\ell = 5$ represents 60 msec. The amplitude scale is relative. The solid curves represent the actual EEG and the dotted curves are the predicted waveforms. In Figure 34, we see that for a lead time of 24 msec., the two curves practically coincide with each other. This indicates a prediction with little error. We progressively increased the lead time from 48 msec. in Figure 35 to 120 msec. in Figure 38. It is observed from this series of figures that the coincidence of the predicted and the actual waveforms worsens. This indication of increasing error as lead time increases is expected. For a quantitative comparison, we computed the prediction error variance, which is used as a performance measure of the prediction scheme, for various lead times. This forecast error variance is shown in Figure 39. The vertical scale gives $V(\ell)/E(x_t^2)$ which represents the prediction error variance relative to the variance of the signal to be predicted. For example, for $\ell = 5$ (i.e., a lead time of 60 msec.) the error variance is 1% of the signal variance. This gives a measure of how close the predicted values will be to the actual values. We can see at a glance from Figure 39 that the performance deteriorates as lead time increases. In using this scheme, one can determine a maximum lead time for any given tolerance level. For our purposes, this scheme is satisfactory.

## IV. CHARACTERIZATION OF SCAN PATTERNS

One of the important aspects of the research done in this project has been the development of techniques and tools for the automatic analysis, characterization and display of scan patterns. In visual tasks, the sequence of fixations used in scanning the visual target is called the "scanpath", and we will refer to a "scan pattern" as a collection of information about the properties of one or more scanpaths recorded by one or several different observers. Naturally, to be able to differentiate a superior scan pattern which results in superior visual memory from an inferior one, we must first be able to characterize a scanpath in some terms other than just a list of (X,Y) fixation coordinates.

A graphical illustration of a sequence of the foveal fixations is shown in Figures 40 and 41. Figure 40 shows the outline drawing of a still life scene which was inspected by a subject with his scanpath superimposed. In Figure 41 we have plotted a sketch of the visual stimulus impressed on the fovea for each fixation point shown in Figure 40. The sketches show a visual field of 6° in diameter, a region which includes all of the fovea under practically any definition. These drawings, then, represent a time sequence of snapshots which are the visual input to the observer who must create a unified picture of the scene being viewed from the sequence of picture fragments shown in the sketches.

One observation which has often been made is that the fixation points tend to be grouped around certain features or areas of the visual image, and are relatively sparse elsewhere. Thus, we can measure

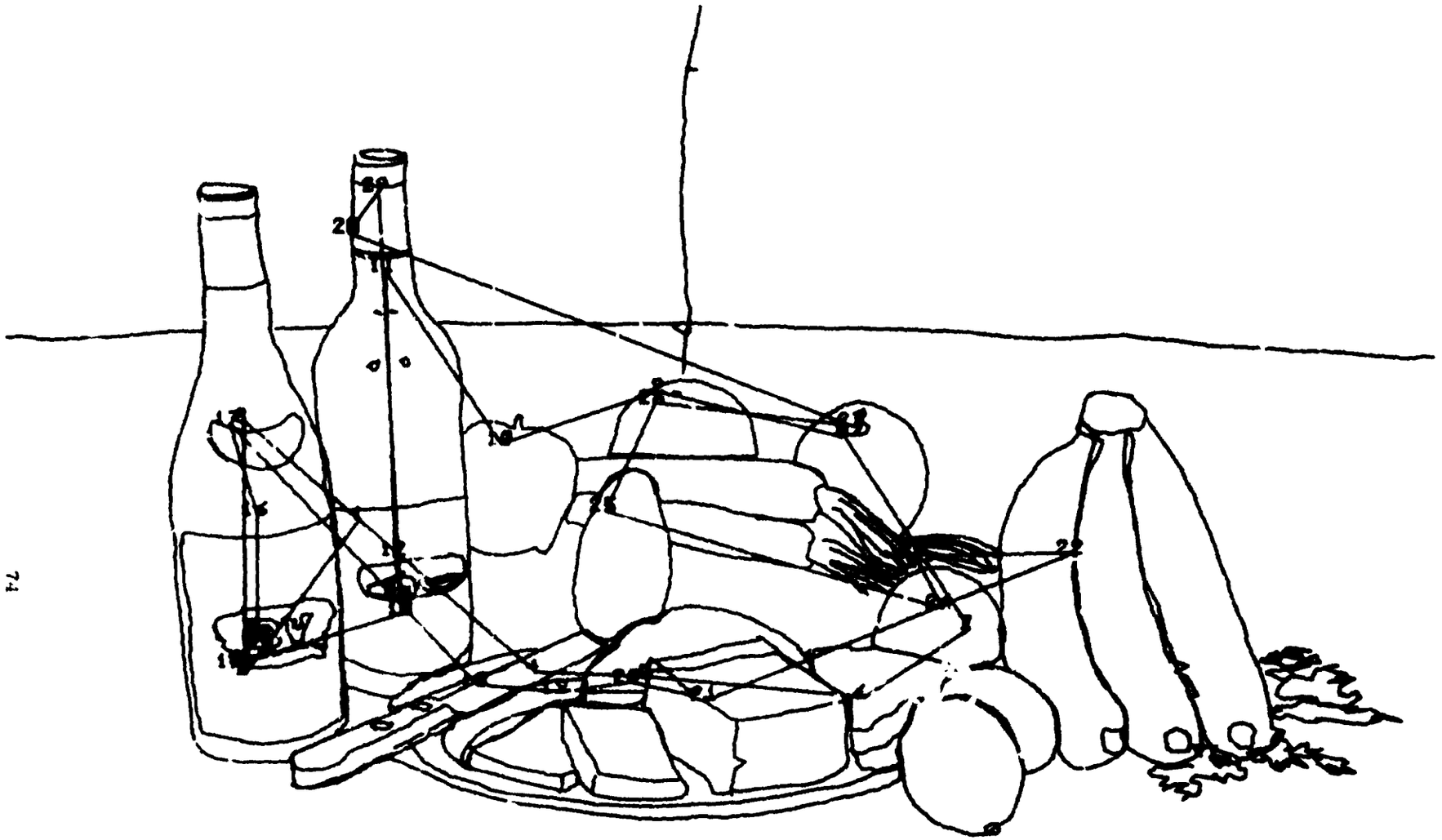

SLIDE 53 OBS: GM 5/30/75 15:35:00 RSP:N
STANDARD III

Figure 40 Computer derived scanpath superimposed on sketch of original scene

Figure 41 Sequence of foveal fixations

the nearness of one fixation point to another and assign a similarity measure to the two points based upon this distance. The ability to group or cluster a set of fixation points is an important step in the characterization of a scanpath, and several different techniques have been used to measure point similarities and to assign points to clusters.

The use of a "point similarity function" for clustering fixation points has been reported earlier and will not be reviewed here.

We have also used two alternate algorithms for selecting cluster centers, each with its own particular advantages and disadvantages. These algorithms are known as "ISODATA" and "Minimum-Spanning-Tree-Clustering" or MSTC.

In the ISODATA method, the number of clusters desired is given an input variable, and the algorithm partitions the fixation points into subsets such that the total distance between the fixation points in a cluster and the cluster center is minimized for all clusters. The cluster center starting points are usually selected randomly, and the algorithm keeps moving the cluster centers until the above criterion has been reached.

The MSTC algorithm automatically determine the number of clusters in the data and assigns fixation points to the clusters. Three variables given as input may be adjusted to change the criteria by which clusters are selected.

The chief advantages or disadvantages of these two algorithms are summarized below:

ISODATA

(1) Required the desired number of clusters, which usually is not known.

(2) Solutions often are not unique, but vary with starting conditions.

(3) The iterations can require a substantial amount of computing.

(4) Many points can be easily accommodated.

MSTC

(1) The solution is unique, and the number of clusters is automatically determined.

(2) The computation is quite fast.

(3) Many points requires a large amount of storage.

Our approach to characterizing scan patterns is based on the following two assumptions:

(a) There are a discrete number of "fixation centers" in the scene being viewed and each fixation point in the scan can be assigned to one of the fixation centers. This process of assignment or clustering is done using the MSTC algorithm described above. The center of the clusters should be in close agreement with the centers of the fixation. Due to the random nature of the fixation points, in any repetition (cycle) of the scanpath, the fixation points do not always coincide.

(b) A scanpath then becomes a sequence of transitions from one cluster center to another. Any saccade with starting and ending points in the same cluster is discarded.

From the set of all saccades leaving a given cluster center, we can find the transition or transitions which have the highest probability. These transtions are termed the "most-probable-saccades". The "most-probable-scanpath" is then defined to be the set of all most-probable-saccades. The most-probable-scanpath depends on how the clusters are chosen, and is not necessarily a closed path through the cluster centers. Its usefulness is that it concisely summarizes the most important aspects of the scanpath used by the observer in viewing the given visual target. A scan pattern is some set of most-probable-scanpaths for a given observer viewing the same or different targets, or for several observers viewing the same target, etc.

Figures 42 and 43 illustrate how these methods may be employed to reduce scanpath data to a more concise form. Figure 42 is a graph of a scanpath superimposed upon a line drawing representing the still life scene which the observer was viewing. The first recorded fixation (1) is in the center of the avocado. The last fixation (45) is in the middle of the carrot. The viewing time required to create this scan totaled 20 seconds. Figure 43 represents the same data after processing by the MSTC program. The program partitioned the fixation points into 11 subsets or clusters (using certain criteria supplied by the programmer) and then computed the most likely transitions from cluster to cluster. Clusters containing only one fixation point were ignored. The resulting plot shows the most likely saccades between areas containing large numbers of fixations, and presents the original data in a highly condensed format.

In order to compare one set of fixations or one scanpattern

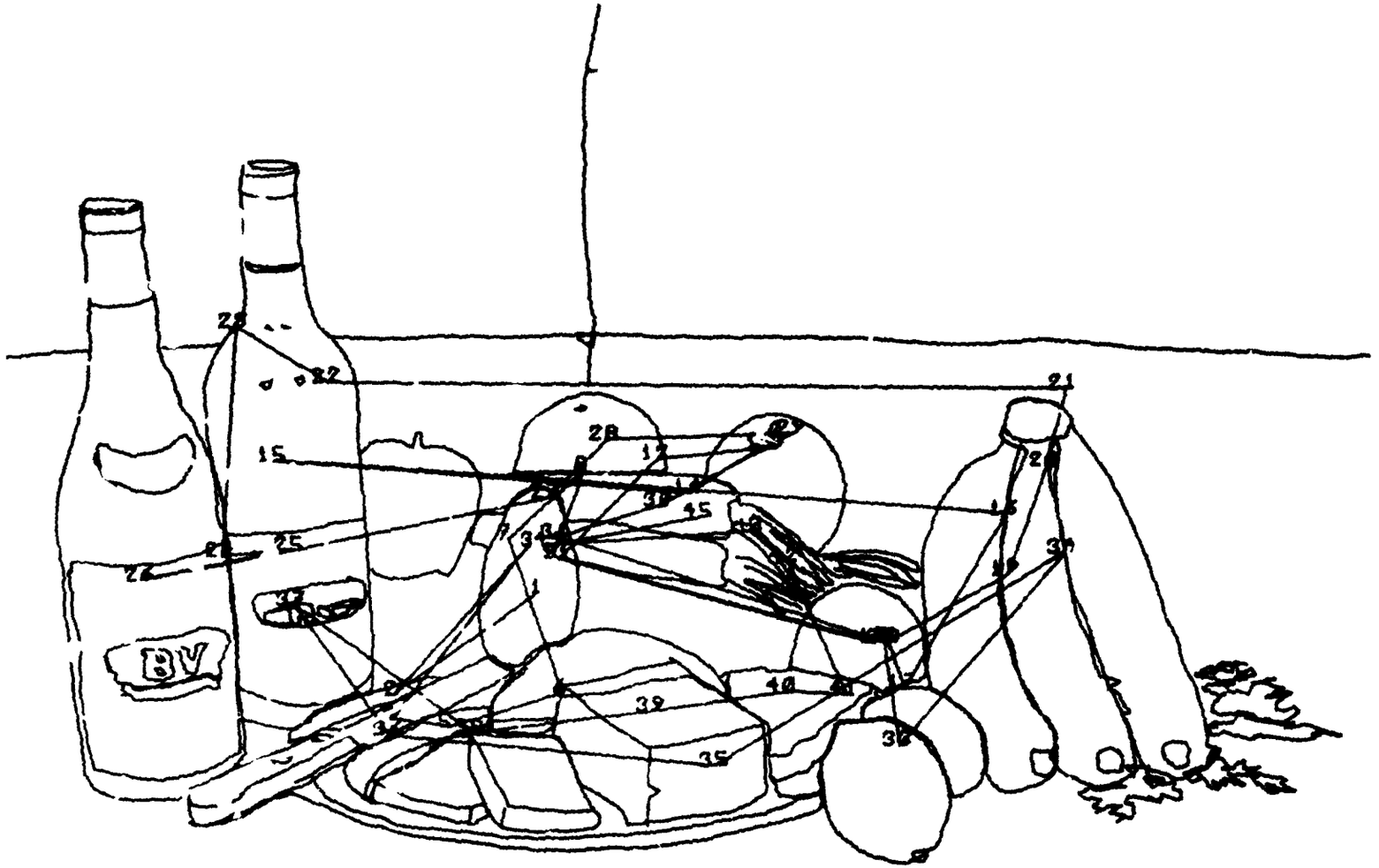


SLIDE 50 OBS: JR 7/7/75 RSP: N
STANDARD SLIDE

Figure 42 Scan of still life scene

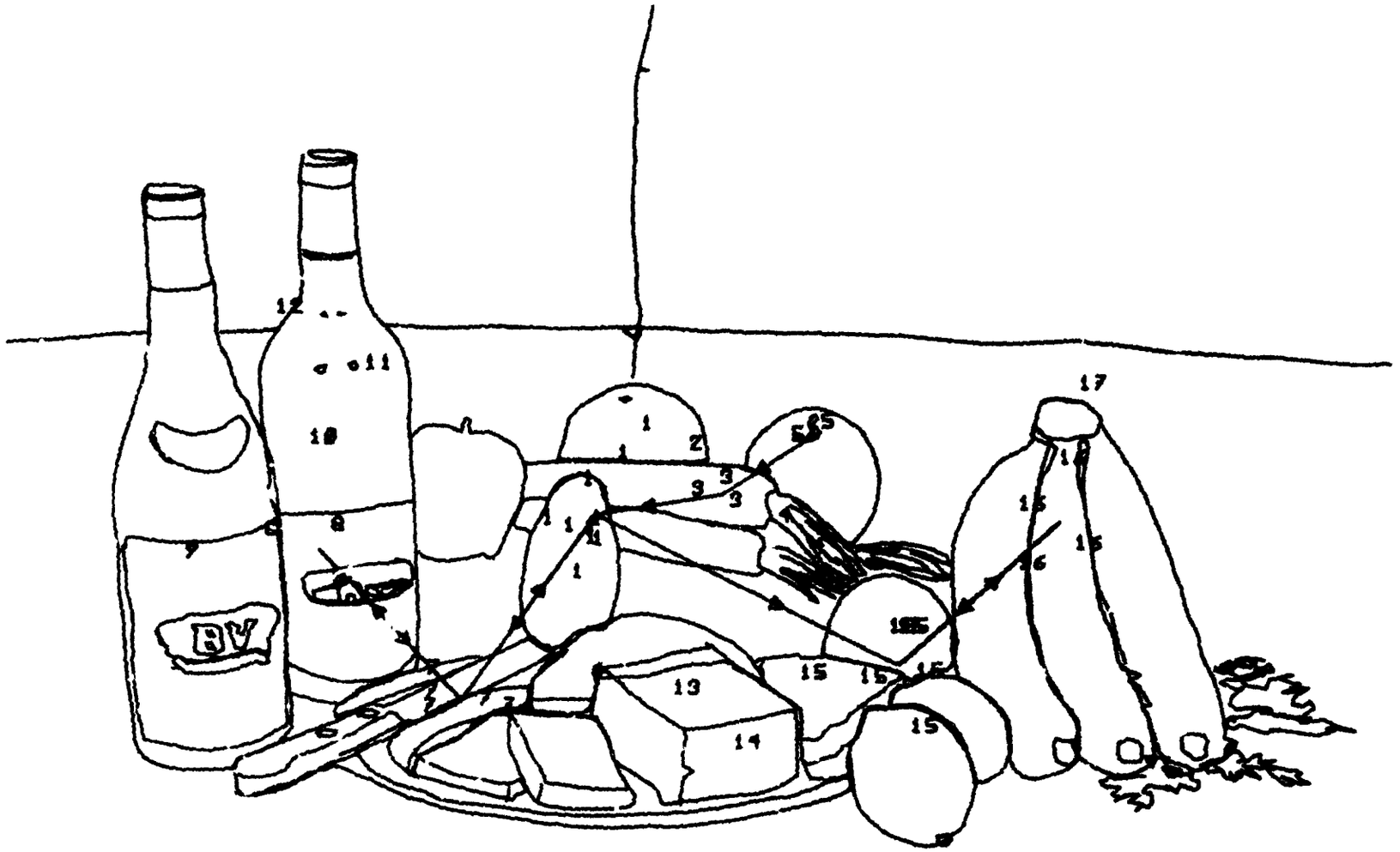


Figure 43 Most probable transitions between cluster centers

against another, criteria must be established which can be used to evaluate subtle differences in the following characteristics:

(1) Total number of clusters - The MSTC algorithm partitions all the fixation points into some number of clusters, very rarely will the number of clusters in two different scans be the same. Rules must be established for eliminating or merging clusters which complicate the analysis. For example, clusters containing a single point can usually be removed.

(2) Similarity between clusters - The geometrical center of two clusters will usually be different, and yet it may seem obvious that both clusters are associated with or centered on some feature of the picture.

(3) The most probable saccades between clusters will often be different in two scans, even if the cluster centers are nearly alike. The similarity of two scans is judged by their transition probabilities.

The above criteria are dependent upon the type of experiment being run and no fixed set of rules will be suggested here. Based on the above criteria and using statistical methods, we are able to show from our preliminary results that the scan patterns of the same visual material by the same subject who scored very high on Marks' Visual-Memory Task are consistent.

## V. TECHNIQUES FOR THE PRESENTATION OF VISUAL CUES

The measurement and prediction of eye movements and related EEG potentials are necessary prerequisites for the control of visually displayed material which can enhance an observer's perception or memory of a scene or visual environment. This section describes some means to couple the measurement of eye movements with the control of a computer-driven graphical display.

The task undertaken was to provide a facility for dynamically controlling the foveal or peripheral field of view of an observer. Such a facility would provide a flexible method for studying interaction between eye position and changes in the visual field. Some of the objectives of this research are:

(a) to develop techniques for dynamically controlling the visual field in humans without any restrictive mechanical attachment to the eye;

(b) to obtain a subjective feeling for perception without use of the normal visual field; and

(c) to quantitatively measure changes in the observer's performance (and scanpath characteristics) as a function of field size and type.

The system works as follows: At the start of each refresh of the display (30 times per second), the position of the eye is measured and the corresponding point on the display is computed. Parameters within the program determine what portion of the visual field will be displayed--fovea only, periphery only, and the size of the field in either case. Then, each point in the display list is checked, and if it is within the

required field, it is displayed. Figures 44 and 45 depict the stimulus for the two modes of display. The box (which was used instead of a circle to simplify computations) remains centered on the fovea, no matter where on the screen the observer looks.

The visual scenes used in these experiments were outline drawings of simple, still scenes. No text or highly detailed pictures were involved. A new scene could be entered into the computer through use of a graf/pen digitizer. Once entered, the points in the picture were stored by X,Y position, and a display list was created for later use by the real-time interactive program.

After adjusting the eye tracker and calibrating the instrument, the observer would be presented with a field of view which could be either a fovea-only presentation or a periphery-only presentation. The size of the field (width of box boundary) was also adjustable, from less than one degree to the maximum width of the display. Use of this program has produced, so far, these results:

Impaired perception for fovea-only vision - If only a two or three degree wide foveal field is displayed (when the display itself spans twenty or more degrees), the observer finds it difficult, if not impossible, to perceive the display. What the observer sees are short line segments, and sometimes junctions between line segments. The only way to perceive an object is to consciously follow the contours and mentally reconstruct the path followed. Simple objects take several minutes to detect. Few observers get a complete idea of the entire scene. Far more use of peripheral visual information is made than was anticipated. Large

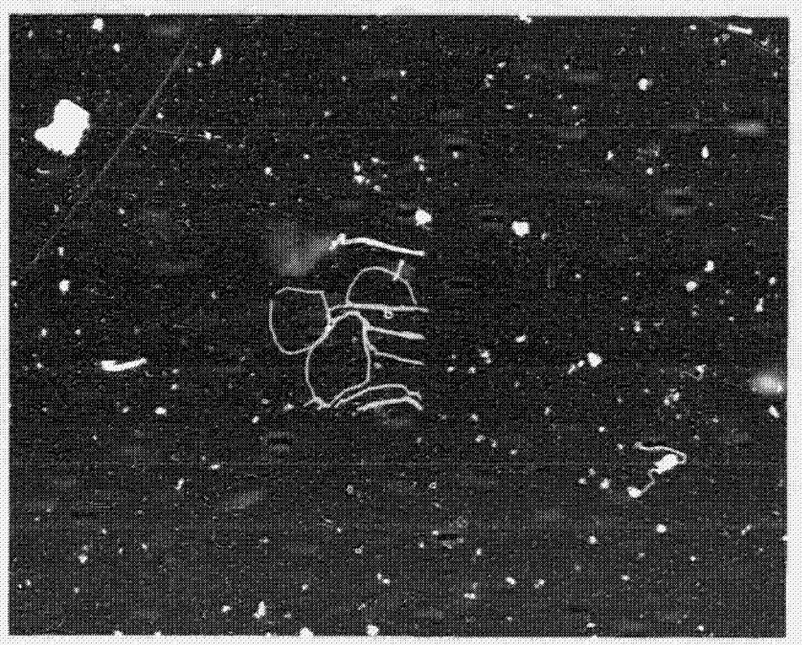

Figure 44 Fovea-only visual field display

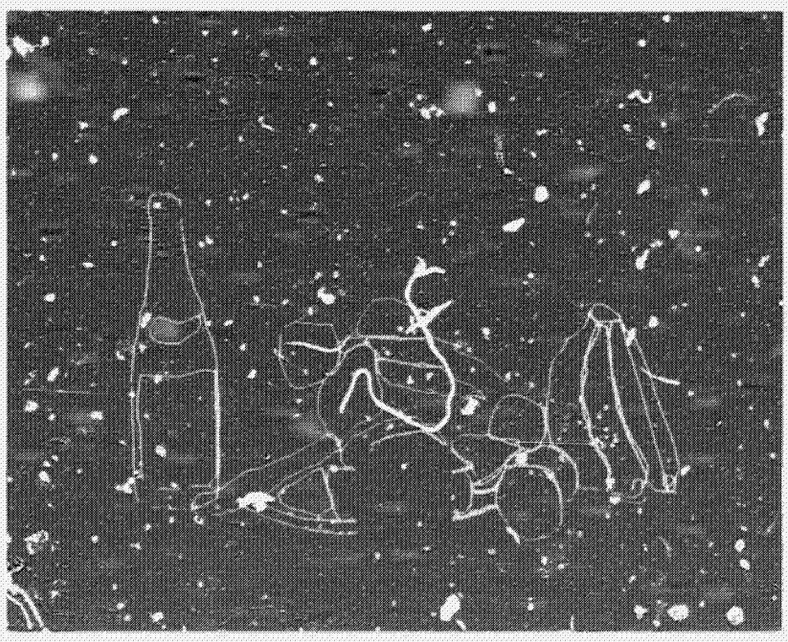

Figure 45 Peripheral visual field display

saccades must be forced, and the observer becomes very conscious of having to manipulate his own eye movements.

Perception with peripheral vision - If the foveal region is blanked, little perceptual loss occurs until the window size approaches roughly 10°, that is, the scene is still perceived even when the window is quite large. Our stimuli did not include text or other material where high visual acuity was essential. This result is somewhat surprising in view of the general assumption of the importance of foveal-high acuity field. The peripheral field apparently makes an important contribution to the overall perception of a scene, even the visual acuity may be quite low in the outer regions.

Importance of closed contours - If the fovea-only visual field is being displayed, little improvement in perception of objects within the field occurs until the window size is large enough to include the complete, closed contour of an object. The absolute size of the foveal region seems to be less important than the fact that complete objects are visible, at least for the line drawings we used. This result supports another observation we have made, which is that fixations tend to be centered on the main surfaces of a simple object, and are not as often found on the edges or corners of the object.

Appearance of a phantom window - After about ten seconds of viewing, and especially for the fovea-only condition, a phantom window with pronounced grey-black edges appears. The subject sees a grey background with a black window cut in the center, through which the white lines may be viewed. The window, of course, is fixated on his eye like an afterimage.

Two causes for the window are evident. Only the foveal region receives stimulation, and the rods and cones adapt to a higher ambient light level than in the periphery, which adapts to "visual grey". Also, the sharp truncation of many contours along a straight line reinforces the perception of an edge. Similar effects have been noted before by Yarbus.

These preliminary experiments with an eye-movement controlled visual display have proved quite interesting and useful. The next step is to incorporate the predictive algorithms discussed in other previous sections of this report to present the visual cues at the desired locations of the visual field at the desired moments.

## VI. CONCLUSIONS

Our aim has been to develop and use biocybernetic techniques for the enhancement of visual memory. To this end, we have designed a closely-coupled man-machine system for implementation. We have developed and completed the models for saccadic eye movements and EEG signals in this man-machine system. The models are used for monitoring and prediction of eye positions and brain states. With the continuously up-dated information concerning the eye position and brain state for adjusting the stimulus parameters and the monitoring and prediction schemes, we can guide the eyes to fixate at the specified locations of the visual field at the specified instants of time through a technique we developed. If these specified locations and instants are the optimally required for superior visual memory, then the vividness and persistence of the desired after-image will be enhanced. We have approached the problem of determination of these optimal locations and time instants by monitoring eye movements and EEG signals through the models which we have developed.

Through the EEG model, we have obtained a better assessment of EEG's role as the timing mechanism for visual information acquisition and processing. We have also shown that the scan pattern is more consistent for individuals with good visual memory (as scored by Marks' Visual-Memory Task) than those with poor visual memory. This comparison is made possible by our method of characterization of scan patterns. With these results, it is possible to determine the optimal locations in the visual field and the optimal time instants for presenting visual stimuli. We conclude

that the approach for visual memory enhancement as proposed is a feasible one. At the termination of this project, we have implemented all of the parts shown in the closely-coupled man-machine system but the feedback path.

Significant accomplishments made during this research have been published or presented in international or national scientific conferences and two Ph.D. dissertations are near completion.

APPENDIX A

## APPENDIX A

## ELECTRONIC INTERFACE SYSTEM

We shall describe here the interface system for eye-movement data acquisition only. We are presently using a double Purkinje image eye tracker developed at Stanford Research Institute (SRI) for measuring eye movements. It relies on measuring the motion of the reflections from the front surface of the cornea and from the back surface of the lens of the eye (the first and fourth Purkinje images). The instrument is discussed in an article: "Accurate two-dimensional eye tracker using first and fourth Purkinje images", by T. N. Cornsweet and H. D. Crane in the Journal of the Optical Society of America, vol. 63, no. 8, pp. 921-928, August, 1973. Figures A.1 and A.2 show the set up of this eye tracker.

The first and fourth Purkinje images are generated by positioning a narrow beam of infrared light on the subject's pupil. The image of the eye and its attendant Purkinje image reflect off the infrared mirror in front of the subject, through two large collimating lenses and on to a movable mirror. A four-quadrant photodetector senses the position of the first Purkinje image. Signals from these four quadrants are used to drive two high-speed servo motors to detect the movable mirror in altitude and azimuth. The function of this servo system is to position the image of corneal reflection when the eye moves so that the reflection is always in the same position; thus, a stable reference of the eye is provided. As the eye moves, the image reflected by the movable mirror will remain stationary. A second optical system in tandem consisting of another movable mirror and quadrant photodetector tracks the fourth

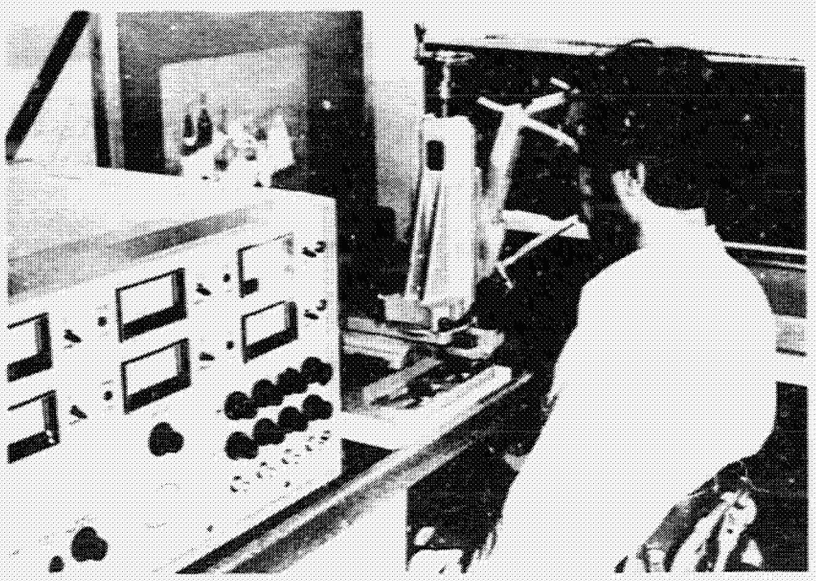

Figure A.1 View of subject in the head positioner with eye-tracker electronics

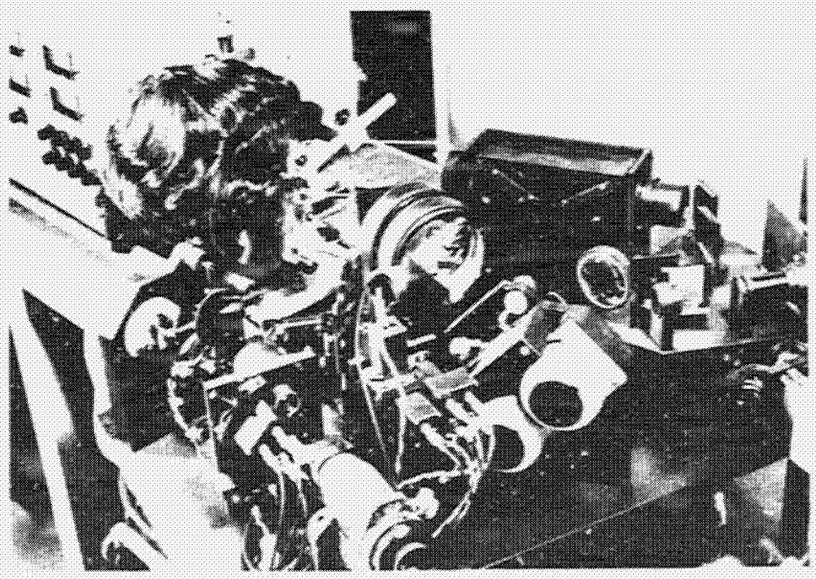

Figure A.2 View of eye-tracker optics and subject

Purkinje image and measures its movement relative to the first image. The two-dimensional motion of this image derived from the position of this mirror system is used as the output signal of the subject's eye movements. The system is designed to measure eye movements with an accuracy of up to two minutes of arc. The overall system has a flat frequency response of up to 100 Hz.

To assure the proper use of the eye tracker requires elaborate procedures for alignment of subjects and calibration of the eye tracker. The calibration is done through a computer program (MAP) we developed. This calibration program serves to:

(1) provide a way of relating the output voltages of the instrument to the stimulus positions;

(2) give an estimate of the size of the visual field over which the instrument is able to track the eye movements; and

(3) indicate whether the eye tracker is correctly adjusted.

It has been a major problem to relate the measured eye positions to the actual locations on the scene. This difficulty arises mainly from the distortion introduced in measuring eye movements. To alleviate this difficulty, we have developed and implemented a scheme which maps automatically the eye fixations onto the scene without distortion. This is achieved by expressing both the fixations and the line drawing of the inspected scene in terms of visual degrees relative to a calibration slide. Since both are on the same coordinate system, they can be easily superimposed without any fear of distortion.

Our scheme consists of the following computer programs: MAP, FIXFIL, OVLAY, and PFIX. MAP produces a calibration file relating

eye tracker voltage with the visual angle subtended by the eye. FIXFIL analyzes the data collected by the DIGIT program. It reduces the data into fixations and, with the aid of the calibration file produced by MAP, it translates the location of these fixations into units of visual angle. The origin of this visual coordinate system is assumed to be the center point of the calibration slide. OVLAY is a variation of the DRAW program which uses the graf/pen to digitize pictures. OVLAY is used to digitize an outline of the inspected scene on a slide. Some additional data are added to the file to enable it to be eventually translated into units of visual angle with the exact coordinate system used by FIXFIL. PFIX plots the fixations and superimpose the outline of the scene. This can easily be done since the fixation locations and the outline are expressed in the same visual angle coordinate system.

To illustrate the effectiveness of this scheme, we show an example in Figures A.3 and A.4. The observer was asked to fixate at those circled points of a scene as shown in Figure A.3. The eye-movement data taken were then processed by the mapping scheme. The result was plotted as shown in Figure A.4. It is seen that the measured eye fixations correspond very closely to those circled points in Figure A.2 in the right sequence.

It should be emphasized that the process described is fully automatic and will compensate for different subjects and any of the permissible variations in the experimental set up such as size of stimulus, distance between the screen and the observer, etc. With this system, we are capable of processing massive amounts of eye-movement data with relative ease.

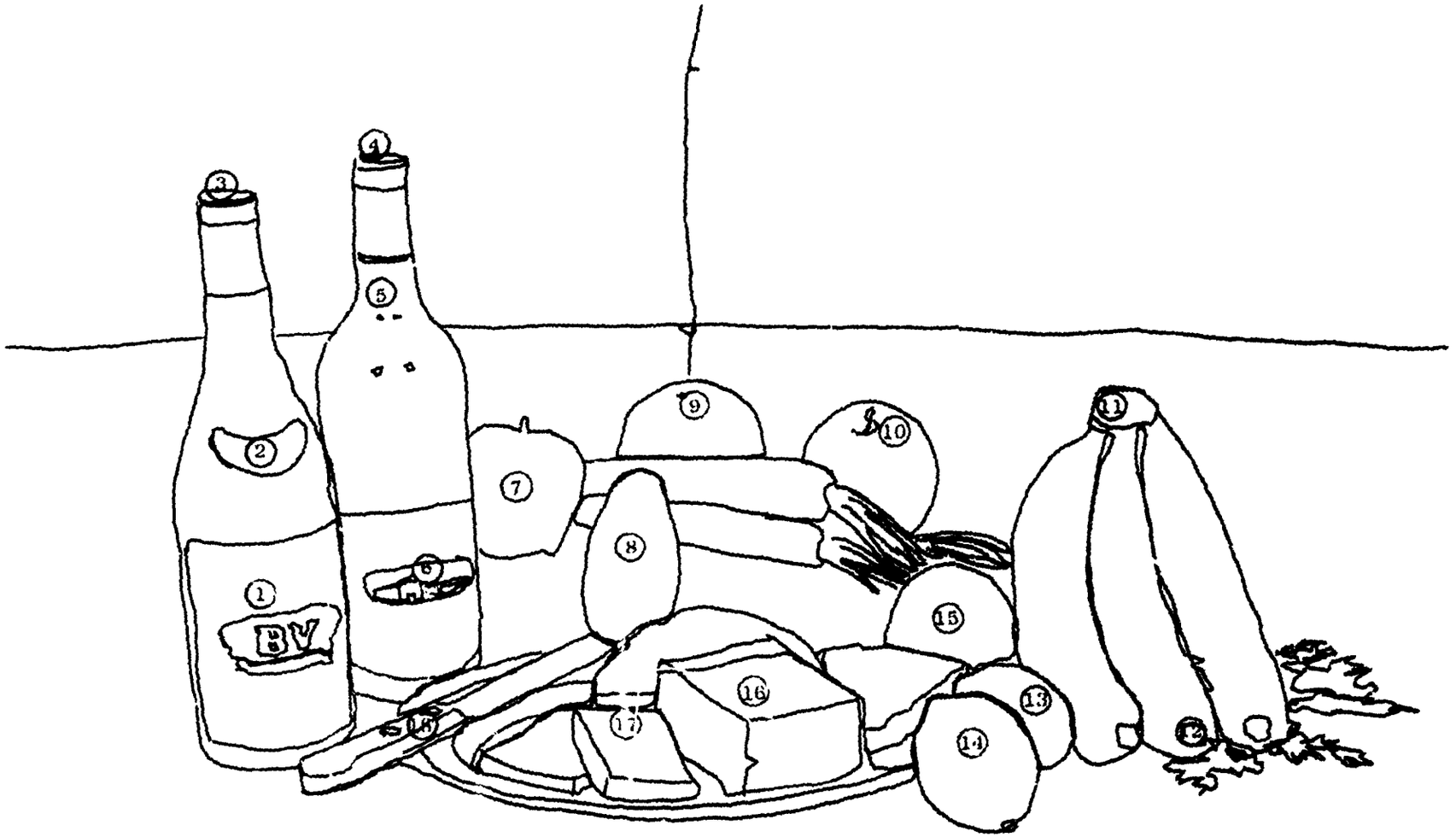


Figure A.3 Requested fixation points

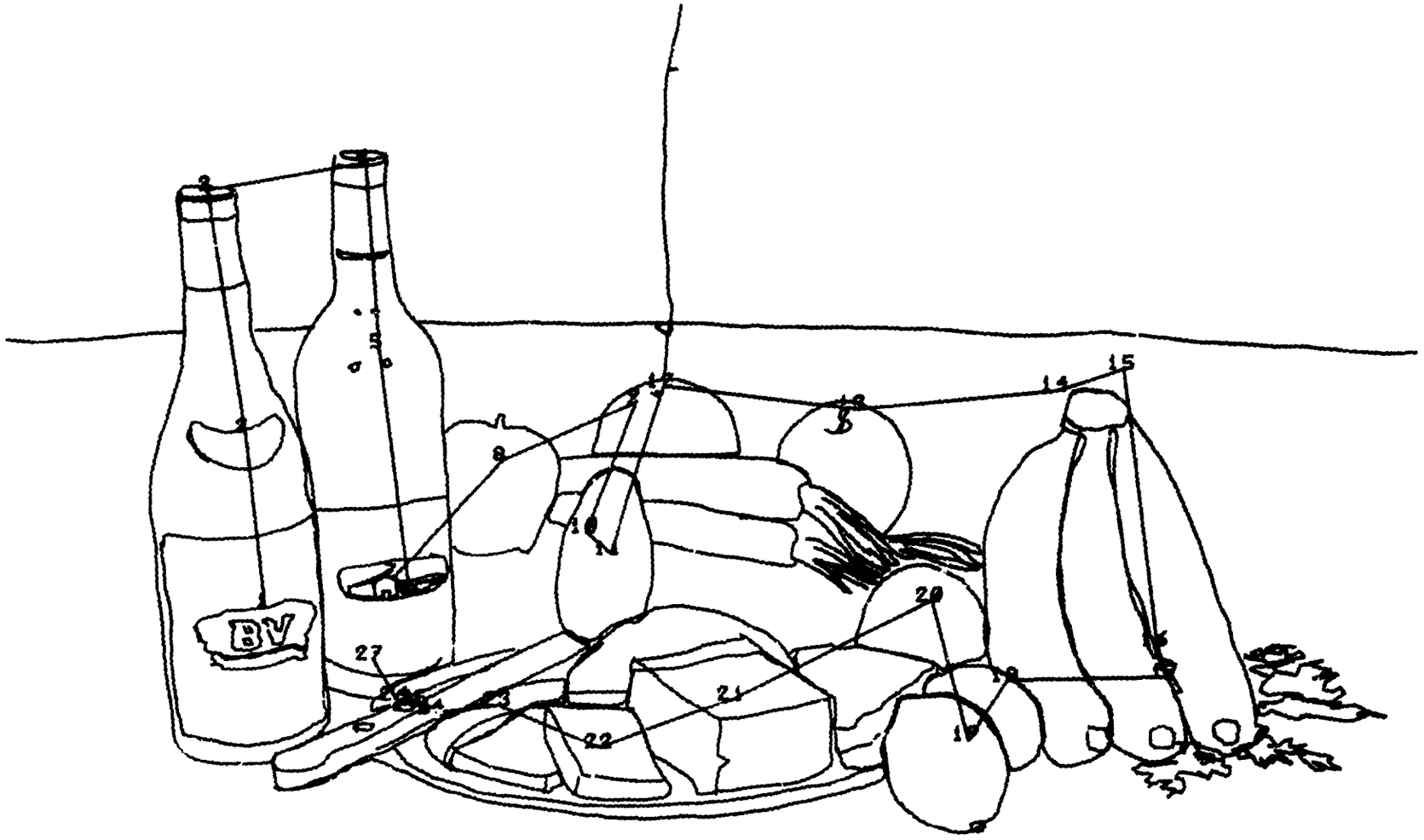


Figure A.4 Responses to requested fixation points

# APPENDIX B

## APPENDIX B

### (1) LIST OF PERSONS WHO HAVE CONTRIBUTED TO THIS PROJECT

Since the inception of this project in 1972, the following persons have participated in this research project. Their present addresses are indicated.

Dr. J. E. Anliker, Research Scientist, NASA/Ames Research Center, Moffett Field, California

Mr. T. E. Attwood, Scientific Programmer, CMX, Sunnyvale, California

Ms. K. Dilley, Project Secretary, Stanford University, Stanford, California

Dr. M. Ein-Gal, Research Associate, Information Systems Laboratory, Stanford University, Stanford, California

Mr. R. Floyd, Graduate Student Research Assistant, Neuroscience Program, Stanford University, Stanford, California

Mr. A. Huang, Scientific Programmer, Stanford University, Stanford, California

Mr. K. H. Jacker, Computer Science Consultant, Environmental Protection Agency, Chapel Hill, North Carolina

Dr. H. S. Magnuski, Engineering Manager, Gamma Technology, Palo Alto, California

*Mr. J. R. Nickolls, Graduate Student Research Assistant, Electrical Engineering Department, Stanford University, Stanford, California

*Mr. A. Shah, Graduate Student Research Assistant, Electrical Engineering Department, Stanford University, Stanford, California

Mr. M. Stauffer, Engineer, Time-Data, Inc., Palo Alto, California

Mr. L. D. Stricklan, Scientific Programmer, Stanford University, Stanford, California

Mr. A. Yang, Student Technician, Stanford University, Stanford, California

*Ph.D. dissertations on topics relevant to the project are near completion.

APPENDIX B

## (2) LIST OF RELEVANT PAPERS PUBLISHED DURING THE PROJECT


[1] "Application of Frequency Discrimination Technique to the Analysis of Electroencephalographic Signals", D. C. Lai and R. L. Lux, Proc. National Electronics Conference, vol. 27, pp. 80-85, October, 1972.

[2] "A Model for the Photically Stimulated Electroencephlographic Signals", R. V. Floyd, J. E. Anliker, and D. C. Lai, Proc. 1973 San Diego Biomedical Symposium, February, 1973.

[3] "The Graphics Software DEC Forgot to Include", K. H. Jacker, Proc. of the DECUS Spring Symposium, May 2, 1973.

[4] "Estimating Signal and Noise in Coherent Time Averages of EEG Data", J. E. Anliker, D. C. Lai, T. Rimmer, and H. Finger, Proc. 1973 Annual Conference on Engineering in Medicine and Biology, October, 1973.

[5] "Real-time EEG Analysis and Monitoring Using In-phase and Quadrature Components", M. Ein-Gal and D. C. Lai, Proc. 26th ACEMB, p. 401, October, 1973.

[6] "Error-free EEG Signal Representation", M. Ein-Gal and D. C. Lai, Proc. IEEE International Conference on Systems, Man, and Cybernetics, pp. 242-243, November, 1973.

[7] "Phase Contingent Expansion of the Visual Evoked Response (VER)", R. V. Floyd and J. E. Anliker, Proc. 1974 San Diego Biomedical Symposium, February, 1974.

[8] "Computer Determination of Eye Fixations and Saccades", A. Shah and D. C. Lai, Proc. 27th ACEMB, p. 103, October, 1974.

[9] "A Nonlinear Model of EEG Entrainment by Periodic Photic Stimulation", J. R. Nickolls, D. C. Lai, and J. E. Anliker, Proc. 7th Annual Meeting of the Neuroelectric Society, pp. 13-14, November, 1974.

[10] "Remark on Algorithm 179[Z]", H. S. Magnuski, Communications of the ACM, vol. 18, no. 2, p. 119, February, 1975.

[11] "Prediction of EEG Alpha Waveform by Using an Autoregressive Model", A. Shah, D. C. Lai, and J. E. Anliker. Proc. 1975 San Diego Biomedical Symposium, February, 1975.

[12] "Computer Control of the Foveal and Peripheral Visual Field", H. S. Magnuski and D. C. Lai, Proc. 28th ACEMB, September, 1975.

[13] "Modeling the EEG Entrainment Process", J. R. Nickolls, D. C. Lai, and J. E. Anliker, Proc. 28th ACEMB, September, 1975.

[14] "Monitoring and Prediction of Saccadic Eye Movement". A. Shah and D. C. Lai, Proc. 1975 IEEE International Conference on Systems, Man, and Cybernetics, September, 1975.

[15] "A System for Monitoring and Prediction of Eye Movements During Perception of a Two-dimensional Stationary Scene", Ph.D. Thesis to be submitted, A. Shah.

[16] "A Nonlinear Model for Human EEG During Photic Stimulation", Ph.D. Thesis to be submitted, J. R. Nickolls.

## APPENDIX B

### (3) LECTURES AND TALKS

The following list gives chronologically the lectures and talks relevant to the work performed under this research project.

1. D. C. Lai, "Measurement of the Entrainment of EEG Alpha Rhythm in the Human Brain by Frequency Discrimination Technique", at the 1972 IEEE International Symposium on Information Theory, February, 1972.

2. D. C. Lai, "The Effect of Photic Stimulation in Human EEG Signals", SEL-ISL Affiliates Meeting, Stanford University, February. 1973.

3. D. C. Lai, "The Phase-uncertainty Model for the Photically Stimulated EEG Signals", EE Seminar, Stanford University, April, 1973.

4. H. S. Magnuski, "Summary of Recent Work on the Relationship Between Eye Movement and Visual Imagery", EE Graduate Seminar, Stanford University, May, 1974.

5. Arun Shah, "An Autoregressive Scheme for Prediction of the EEG Alpha Rhythm", SEL-ISL Affiliates Meeting, Stanford University, February, 1975.

6. J. R. Nickolls, "A Nonlinear Model of Human EEG Entrainment by Periodic Photic Stimulation", SEL-ISL Industrial Affiliates Meeting, Stanford University, February, 1975.

7. H. S. Magnuski, "Scanpaths and Theory of Vision", EE Graduate Seminar, Stanford University, May, 1975.

8. J. R. Nickolls, "Nonlinear Models of the EEG Signal During Visual Stimulation", Ph.D. Seminar, Stanford University, July, 1975.

9. Arun Shah, "Analysis and Modeling of Eye Movements During Perception of Scenes", Ph.D. Seminar, Stanford University, August, 1975